ENSC-(n° d'ordre)

THESE DE DOCTORAT
DE L'ECOLE NORMALE SUPERIEURE DE CACHAN

Présentée par

Mademoiselle SHI Feifei

pour obtenir le grade de

DOCTEUR DE L'ECOLE NORMALE SUPERIEURE DE CACHAN

Domaine:

MÉCANIQUE-GÉNIE MÉCANIQUE-GÉNIE CIVIL

Sujet de la thèse:

Comportement des tôles métalliques à gradient de propriété sous chargement dynamique

Thèse présentée et soutenue à Xi'an le 19 août, 2015 devant le jury composé de:

ZhiQiang FENG	Université d'Evry	Rapporteur
GuoXing LU	Swinburne University	Rapporteur
ShengPing SHEN	Xi'an JiaoTong University	Examinateur
YuLong LI	Northwestern Polytech. University	Directeur de thèse
Han ZHAO	Université Pierre et Marie Curie	Directeur de thèse

Laboratoire de Mécanique et Technologie
ENS CACHAN/CNRS/UMR
61, avenue du Président Wilson, 94235 CACHAN CEDEX (France)

Impact behavior of functionally graded multi-layered sheet metals

Dissertation submitted to

Ecole Normale Supérieure de Cachan

and

Northwestern Polytechnical University

In Partial Fulfillment of the Requirements

For the Degree of Doctor of Philosophy

by

Feifei SHI

Doctoral committee

ZhiQiang FENG	Université d'Evry	Reporter
GuoXing LU	Swinburne University	Reporter
ShengPing SHEN	Xi'an JiaoTong University	Examiner
YuLong LI	Northwestern Polytech. University	Superviser
Han ZHAO	Université Pierre et Marie Curie	Superviser

Laboratoire de Mécanique et Technologie
ENS Cachan/CNRS/UMR
61, avenue du Président Wilson, 94235 CACHAN CEDEX (France)

Acknowledgements

First and foremost, I would like to avail myself of the opportunity to express my heartfelt gratitude to my two advisors, Professor Han Zhao in LMT-Cachan and Professor Yulong Li in NPU, for all that they have done to help me. Without their careful and offering constant encouragement, valuable suggestions and enlightening instructions, I cannot end my thesis successfully. I will forever appreciate their patience in teaching me from ignorance to who I am at the present, the wonderful instructions in science research as well as the caring advice for career and life.

I would also like to acknowledge my indebtedness to my colleagues in LMT and NPU. I would like to thank Dominique Saletti, Jiagui Liu, He Huang, Omar Kraiem and Amine Bouterf who fight for the thesis together with me in the office, for their help and also the great time to be with them during my stay in France.

I am also grateful to all the friends in both France and China who have given me generous support and helpful advice in the past years. They have accompanied me for such a long time and encouraged me at any time. I give the special thanks to my treasured friend Qian Dong who encouraged me to get over all the tough times.

I also must thank the financial support from China Scholarship Council to provide me the opportunity to study abroad. Thanks to LMT-Cachan for the kind reception and the convenience they provided to perform the research work. Thanks to 111 project of China for funding the cooperations between NPU and LMT.

I owe a lot to my beloved family as well for their consistent support and encouragement in this long journey. I could not have achieved this without their love and encouragements.

Finally, I would also like to thank my doctoral committee for their assistance and suggestions.

Abstract:

This Ph.D dissertation aimed at the comprehensive understanding and the constitutive modeling of the mechanical behaviours of the surface mechanical attrition treatment (SMAT) treated AISI304 stainless steel sheet under a large range of loading rates. SMAT treated AISI304 stainless steel sheets are multi-layered functionally graded materials (FGM). The main research results and conclusions are summarized as followed:

(1) The overall rate sensitivity SMAT treated AISI304 stainless steel sheet is characterized by the double shearing test under quasi-static and dynamic loading where a large strain can be achieved without geometry instability. Impact double shear test are performed with a large diameter Hopkinson bar system and an adapted equal-impedance clamping device. Significant rate sensitivity is found. It is also observed that such a rate enhancement does not induce an important reduction of the ductility.

(2) In order to extract accurate material information from the double shear tests, their testing conditions are thoroughly analyzed using numerical simulation. Numerical models including clamping devices have been built to investigate the influence of this clamping device at the early stage of loading. A limited effect was found for various imperfect testing conditions such as the clamping device stiffness, non-homogeneous stress and strain fields, non-equilibrium state, etc. On the contrary, numerical and analytical study shows that the simple small strain assumption usually used in double shear tests are not accurate enough. Eulerian cumulated strain definition should be used to get consistent numerical results. From this finding, the experimental rate sensitivity obtained for the SMAT treated AISI304 stainless steel sheet are recalculated.

(3) A multi-layers elastic plastic damageable constitutive model is proposed to model SMAT treated AISI304 stainless steel sheet. The parameters are identified using tensile testing results. The elastic plastic behavior is curve fitted with a simple Ludwig hardening model. However, the damage parameters should be identified using an inverse method on the basis of numerical simulation of these tensile tests. In order to validate this multi-layer elastic plastic damageable constitutive model, indentation/piercing tests on SMAT treated AISI304 stainless steel sheet are performed. Numerical simulation of this indentation/piercing tests is also realized. It

is found that the identified multi-layer elastic plastic damageable constitutive model allows for a quite accurate prediction of the experimental piercing tests.

(4) In order to evaluate the impact anti-piercing capacity of the SMAT treated AISI304 stainless steel sheet, the impact perforation tests using Hopkinson bar are carried out. Numerical simulation of these impact perforation tests are realized with a similar FEM model as the quasi-static case. As the rate sensitivity of SMAT treated AISI304 stainless steel sheet is experimentally characterized with double shear test, a rate sensitive multi-layer elastic plastic damageable constitutive model is introduced. The numerical results agree well with the experimental ones, which indicates the effectiveness of the numerical model as well as the rate sensitive multi-layer elastic plastic damageable constitutive model.

Key words: Functionally graded multi-layered sheet metals; SMAT treated AISI304 stainless steel; Rate sensitivity, Double shear tests; Hopkinson bars; Elastic plastic damageable model.

Résumé:

Cette étude vise à bien comprendre puis à modéliser le comportement mécanique dans une large plage de vitesse de déformation des tôles d'acier austénitique AISI304 ayant subis un traitement d'attrition mécanique de la surface (SMAT). Ces tôles ainsi traités sont des matériaux multicouches avec un gradient de propriétés. Les principaux résultats obtenus sont résumés comme suit:

(1) La sensibilité globale à la vitesse déformation des tôles d'acier austénitique AISI304 traités avec SMAT est caractérisée par des essais de double cisaillement sous chargements quasi-statiques et dynamiques, qui permet d'atteindre une grande déformation sans instabilité geométrique. Des essais de double cisaillement sous impact sont réalisés à l'aide des barres de Hopkinson de grande diamètre et un système d'attache qui a une même impédance acoustique que la barre. Une sensibilité significative a été révélée et on observe ce renforcement n'a pas induit une réduction importante de la ductilité.

(2) Dans le but d'un meilleur dépouillement de ces essais de double cisaillement, leur conditions d'essai est analysé dans le détaillé. Le modèle numerique avec le système d'attache a été construit pour étudier l'influence du système d'attache au debut de chargement. On trouve un effet limité pour les diverses conditions imparfaites des essais comme la souplesse de système d'attache, des champs mécaniques non-homogènes, l'état de non-équilibre, etc. Par contre, les études numerique et analytique ont démontré que l'hypothèse simple de petites perturbations habituellement utilisé pour le dépouillement de ces essais n'est pas suffisemment précise. La déformation Eulérien cumulée doit être utilisée pour obtenir un résultat numerique correct. A partir de ce résultat, la sensibilité à la vitesse déformation des tôles d'acier austénitique AISI304 traités avec SMAT obtenue expérimentalement a été retouchée.

(3) Un modèle multicouche elasto-plastique en dommageable a été proposé pour décrire le comportement des tôles d'acier austénitique AISI304 traités avec SMAT. Les paramètres sont identifiées à partir des essai de traction. La partie elasto-plastique est calée par une loi d'écrouissage de type Ludwig. Par contre, les paramètres d'endommagement sont obtenues avec une méthode d'identification inverse sur la base de simulation numerique de ces essais de traction. Pour valider ce modèle multi-couche elasto-plastique dommageable, un essai d'identation/perforation est realisé sur des tôles d'acier austénitique AISI304 traités avec SMAT. Des simulations

numeriques correspondantes montres que ce modèle multi-couche elasto-plastique en dommageable une prédiction plutôt précise de ces essais de d'identation/perforation.

(4) Pour évaluer la performance anti-perforation des tôles d'acier austénitique AISI304 traités avec SMAT, des essais de perforation sous impact a été realisés avec des barres de Hopkinson. Numeriques simulations de ces essais de perforation sous impact sont realisées avec un modèle numerique comparable avec le cas quasi-statique. Étant donne que la sensibilité globale à la vitesse déformation des tôles d'acier austénitique AISI304 traités avec SMAT est caractérisée par des essais de double cisaillement, la sensibilité à la vitesse a été introduite dans le modèle multi-couche elasto-plastique en dommageable. Le résultat numerique correspond bien à la mesure expérimentale, ce qui indique non seulemnt l'efficacité du modèle numerique mais aussi celle du modèle multicouche elasto-plastique en dommageable.

Mots clés: Tôles métalliques multicouches à gradient de propriétés; Tôles d'acier austénitique AISI304 traités avec SMAT; Sensibilité à la vitesse; Essais de double cisaillement; Barres de Hopkinson; Modèle elasto-plastique dommageable.

TABLE OF CONTENTS

CHAPTER 1 INTRODUCTION 1

1.1 BACKGROUND OF FGM 1
1.2 CURRENT FGM RESEARCHES 3
1.2.1 Manufacturing path of functionally graded materials 3
1.2.2 Mechanical performance studies on graded multi-layered materials 6
1.3 GRADED SHEET METALS PRODUCED BY SMAT 12
1.3.1 Introduction of Surface mechanical attrition treatment (SMAT) 12
1.3.2 SMAT treated graded AISI304 stainless steel sheet 14
1.4 AIMS AND OUTLINE OF DISSERTATION 16

CHAPTER 2 RATE SENSITIVITY OF SMAT TREATED AISI304 AUSTENITIC STAINLESS STEEL SHEET 19

2.1 REVIEW OF SPLIT HOPKINSON PRESSURE BAR TECHNIQUE 19
2.1.1 Set-ups of Split Hopkinson Pressure Bar 19
2.1.2 Some specific problems in SHPB technique 21
2.2 EXPERIMENTAL TECHNIQUES FOR CHARACTERIZING THE SMAT TREATED AISI304 AUSTENITIC STAINLESS STEEL SHEET USING SHPB 22
2.2.1 Choice of testing technique 22
2.2.2 Review of impact plane shear test 23
2.2.3 Double shear test on the SMAT treated AISI304 austenitic stainless steel sheet under quasi-static and dynamic loading 27
2.3 NOMINAL RESULTS OF RATE SENSITIVITY SMAT TREATED AISI304 AUSTENITIC STAINLESS STEEL SHEET 34
2.4 SUMMARY 37

CHAPTER 3 COMPREHENSIVE ANALYSIS OF IMPACT DOUBLE SHEAR TESTS 39

3.1 VALIDITY OF STRESS-STRAIN CURVE OBTAINED FROM DOUBLE SHEAR TEST 39
3.2 NUMERICAL EVALUATION OF SHEAR ZONE HOMOGENEITY 40
3.3 NUMERICAL ANALYSIS OF THE INFLUENCE OF THE CLAMPING DEVICE 44
3.3.1 Quasi-static test simulation 45
3.3.2 Impact test simulation 48
3.4 LARGE STRAIN DEFINITION USED IN FEM CODES AND STRAIN CORRECTIVE COEFFICIENT 54
3.5 APPLICATION TO SMAT TREATED AISI304 AUSTENITIC STAINLESS STEEL SHEET 57
3.6 SUMMARY 58

CHAPTER 4 PARAMETER IDENTIFICATION OF A MULTI-LAYERS ELASTIC-PLASTIC DAMAGEABLE MODEL FOR SMAT TREATED AISI304 AUSTENITIC STAINLESS STEEL SHEET 59

4.1 MULTI-LAYERS GEOMETRY AND THE ELASTIC PLASTIC PARAMETERS OF EACH LAYER. 59
4.2 DETERMINING THE DAMAGE EVOLUTION AND FRACTURE STRAIN OF EACH LAYER 61
4.2.1 Inverse identification by numerical simulation 61

4.2.2 Selected damage model....63
4.2.3 Simulated results and identified parameters....65
4.3 VALIDATION OF THE IDENTIFIED ELASTIC-PLASTIC DAMAGEABLE MODEL....68
4.3.1 Quasi-static piercing test....68
4.3.2 Numerical models of the piercing test....70
4.3.3 Numerical results and comparisons....71
4.4 SUMMARY....72

CHAPTER 5 ANTI-PERFORATION PERFORMANCE OF SMAT TREATED AISI AUSTENITIC STAINLESS STEEL SHEET UNDER IMPACT LOADING AND FGM DESIGN....75

5.1 IMPACT PIERCING TESTS OF SMAT TREATED AISI AUSTENITIC STAINLESS STEEL SHEET....75
5.2 NUMERICAL SIMULATION OF PIERCING TESTS USING THE A MULTI-LAYERED ELASTIC PLASTIC RATE SENSITIVE CONSTITUTIVE MODEL....79
5.2.1 Numerical model for piercing test....79
5.2.2 Rate sensitivity of the multi-layered elastic plastic constitutive model....79
5.2.3 Numerical results....81
5.2.4 Comparisons experiment-simulation....82
5.3 PROSPECTIVE NUMERICAL STUDY ON FGM DESIGN....83
5.4 SUMMARY....84

CHAPTER 6 CONCLUSIONS AND PERSPECTIVES....87

REFERENCES....89
APPENDIX....101
Publications and International Communications....101

Chapter 1 Introduction

1.1 Background of FGM

Functionally gradient materials (FGM) in some extent can be understood as composite materials with a property gradient in order to create a material with an optimized global property. For example, the biological materials in nature are functionally graded materials. In order to adapt to the living environment, the biological materials such as bamboo, bone, tortoise shell, trees and animals[1-6] (see Figure 1.1) have a density gradient which allows achieving both high strength and high toughness with a low global density.



Figure 1.1 Body armors of animals and plants

The concept of functionally gradient materials (FGM) was initially introduced in 1984 by material scientists in the Sendai area in Japan as a means of preparing thermal barrier materials in space-planes to withstand thermo-mechanical loading[7]. They used heat-resistant ceramics on high-temperature side and tough metals with high thermal conductivity on the low-temperature side with a gradual compositional variation from ceramic to metal. FGM is thus defined as composite materials because of its microscopically inhomogeneous character. However, there are differences between FGM and conventional composite materials. The differences in microstructure and properties between them are shown schematically in Figure1.2.

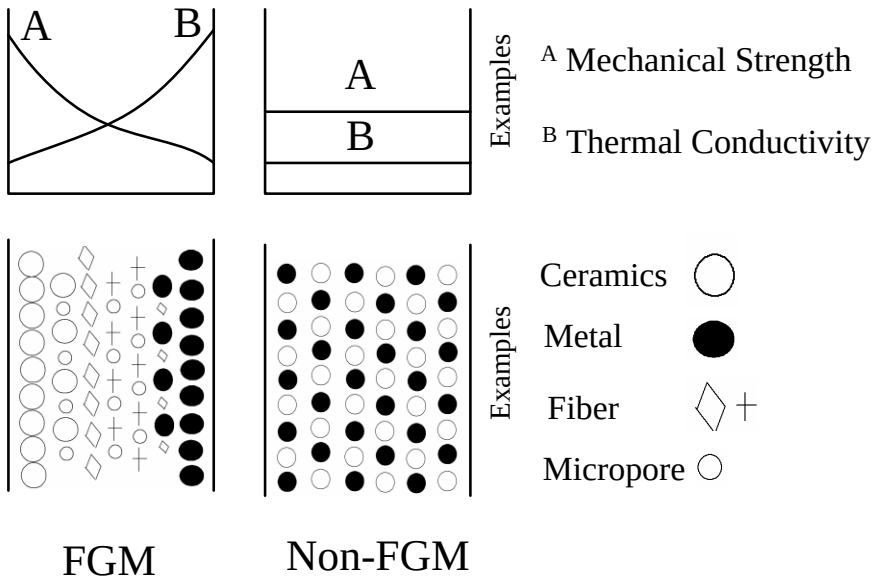


Figure 1.2 Comparisons of FGM and non-FGM[7]

According to the requirements of applications, the composition and the organization can continuously change in design and manufacturing process of FGM, which leads to the gradient in materials without obvious interfaces. Meanwhile, compared with the conventional materials, the graded materials are actually optimized. Therefore, superior properties of graded materials can be obtained.

Nature is always a master in design of such materials[8-9]. The performance of monolithic components in general is not the best, but they can be bonded together to form biological FGM with very good mechanical properties. A recent research[10-11] analyzed the scales of an ancient fish. By using the complex hierarchical structures, the fish scale characterized by a decreasing stiffness and an increasing energy absorption capacity from outer to inner layers, served as body armors to resist impact damage. Such hierarchical materials as the fish scale spread impact force by the hard surface layer and absorb the energy by soft interior layers. Therefore they will provide better penetration-resistance and high weight-efficiency than the monolithic materials (see Figure 1.3).

In order to adapt the particular surviving environment, biological organisms system can even optimize their mechanical properties to adjust the surrounding situations[12] and finally form different hierarchies in different levels from molecular to nano, micro and macro scales[13]. Gradient structures of natural biological materials are the form of hierarchical and ordered features, which shows good mechanical properties on high strength, meanwhile improving toughness.

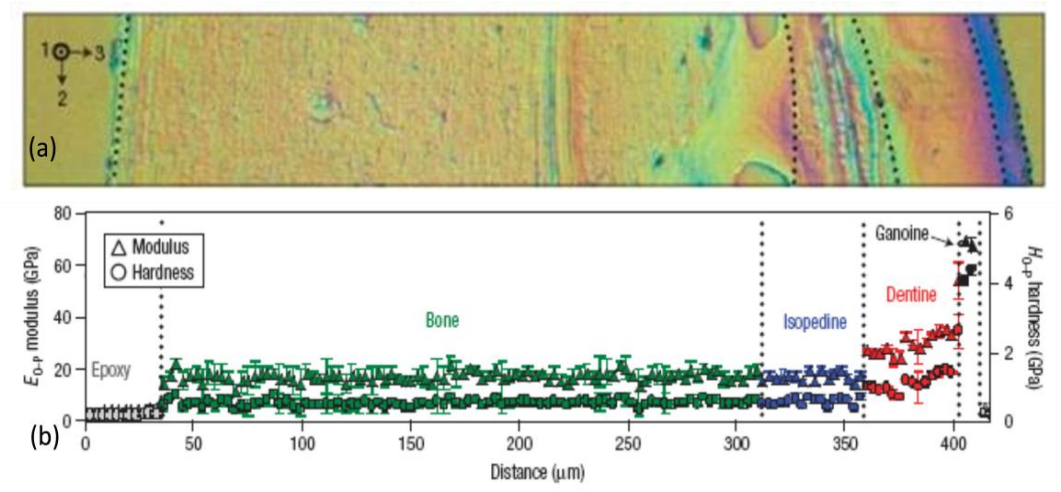


Figure 1.3 Topography of different material layers(a) and
Distance-Hardness & Distance-Modulus curves[10]

The human being can be inspired by these biological hierarchical structures to design graded materials to resist impact by using outer hard materials to disperse the impact force while the inner soft material can absorb the energy to protect human body[14]. For example, the FGM made of metal matrix composites enhanced by ceramics could be used in tanks, armored vehicles, helicopters and attack aircrafts as protection armor. Such FGM designed armor offers the advantages of decreasing its weight and at the same time enhancing its impact resistance. We can also take example in the crashworthiness design in automotive industry. Multi-layered structures, gradient can be introduced to enhance energy absorbing capacities.

In summary, FGM concept has been recently introduced by material scientists and it spreads out in many related domains with wide prospective engineering applications. In particular, it offers a new trend in impact performance and crashworthiness designs.

1.2 Current FGM Researches

1.2.1 Manufacturing path of functionally graded materials

Generally, functionally graded materials are divided into two types: the continuous functionally graded materials with a continuous gradient changing from one side to another side and the multi-layered functionally graded materials produced by bonding different materials.

1.2.1.1 Fabrication for continuous Functionally graded materials

Most of traditional manufacturing methods such as CVD/PVD, powder metallurgy, plasma sprays and self-propagating combustion synthesis (SHS) can be used to fabricate FGM. These processes are mostly involved in making FGM thermal barrier.

The surface treatment techniques can also create property gradient through the treatment thickness. Indeed, the failure mechanism of metallic materials such as fatigue cracks and erosion often starts from the surface, a surface treatment is then necessary to improve the serving life of material. Taking surface nanocrystallization technique as an example[15-17], mechanical performance and chemical performance after surface nanocrystallization are enhanced because a nanocrystallizing layer has been induced and the grain size has been gradually increased from the surface to core. This microstructure gradient induces hardness gradient through the depth[16-18]. Surface nanocrystallization technique can therefore produce a graded material.

1.2.1.2 Fabrication for Multi-layered Functionally graded materials

Common manufacturing methods for multi-layered functionally graded material include repeat rolling, cold roll bonding, accumulative roll bonding (ARB)[19-21]. Actually, these methods are solid state welding techniques, where the metal sheets can bond together at atomic level because of the large deformation of metallic materials, which is obtained as a permanent secure connection.

Gajananp and co-workers[22] developed an analysis on the roll bonding of multi-layered bimetals in order to give laminate composites and applied to Ti-Al system. The model gave qualitative information on the conditions suitable for roll bonding. With the increase of passes, two elements spread well into each other and the bonding ability becomes more and more solid. Carreno and co-workers[23] processed a seven layer steel based (mild steel and ultrahigh carbon steel, UHCS) laminated composite by roll bonding. It is found that this laminated composite has a better capacity of energy absorbing because the nucleation of new cracks from one material layer to the next layer is more difficult. Figure 1.4 shows SEM micrograph of the graded multi-layered steel sheet. It is clearly displayed that the grains of two kinds of steels have been refined to some extent, and there is a bond of Carbide at the interface, which provides the best connection for the two kinds of steels.

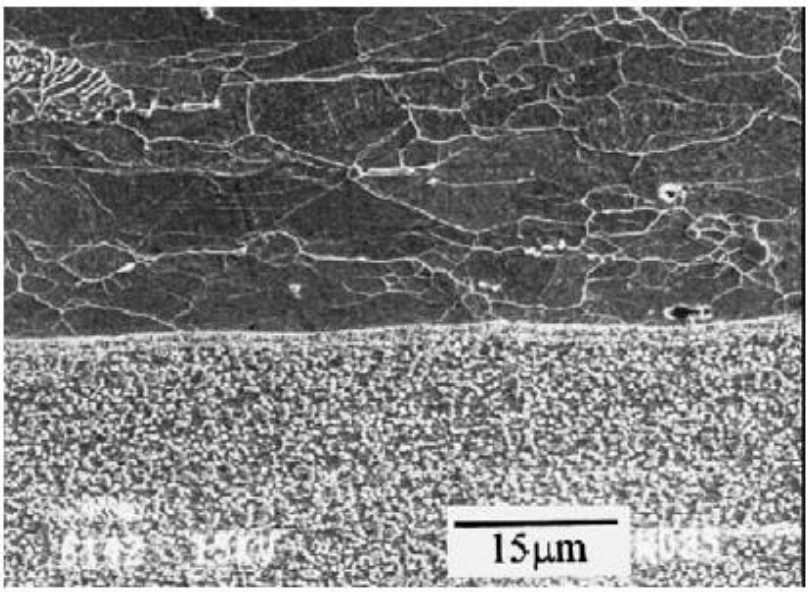


Figure 1.4 Micro-structure of the multi-layered graded sheet steel[24]

Back to 1980, Moore and co-workers[25] already developed composite fabrication techniques for the reinforcement of a precipitation-hardening aluminium alloy (Duralumin) with stainless steel and maraging steel (also for the reinforcement of titanium alloys with high strength steel) using hot-cold rolling. Wu and co-workers[24] performed many genuine solid-state-bonding experiments for a great number of metals, including superplastic ultra-high-carbon steel, Fe – Ni – Si alloy, manganese steel, brass, stainless steel, iron-silicon alloy as well as two superplastic aluminum alloys. Tamotsu and co-workers[26] developed a new method for producing laminated Mg-Ni binary hydrogen storage materials by a repetition of alternative stacking and cold rolling, combined with final heat treatment.

Accumulative roll bonding (ARB) method has been practised by Eizadjou and co-workers[27] on Al/Cu graded multi-layered material. ARB process of primary Al/Cu multi-layer sandwich involves two main steps: the first is the surface treatment which includes degreasing of bonding surfaces of primary multi-layer (outer aluminum layers) by acetone, air drying and then scratch brushing the degreased surfaces by a circular steel brush. The second step is the concurrent rolling of the stacks of primary multi-layer sandwich at a rolling speed of 5 rpm repeated 5 times at room temperature. These steps resulted in layered Al/Cu composites using severe plastic deformation. The time between surface treatment and rolling was maintained less than 60 s in order to avoid re-formation of oxide layers on the surface.

It is also possible to use other bonding techniques. Kundu and co-workers[28] carried out the solid-state diffusion bonding between commercially pure titanium and 304 stainless steel using 300 μm copper interlayer. Coalescence of elements play an important role to avoid problems mentioned above. Zeng and co-workers[29-30] glued aluminum plates and aluminum foam into functionally graded structure. Wadley and co-workers[31] made sandwich graded structures with filling alumina into aluminum frames. Yu and co-workers[32] produced graded plates consisting of layered structures with two stack sequences prepared by vacuum hot pressure diffusion processing.

1.2.2 Mechanical properties of graded materials under impact loading

The advantage of graded materials basically lies in the possibility to adapt the property gradient to the loading environment so that the stress levels in the whole structure are optimized. It is evident that the property gradient will have no advantage in a homogeneous loading environment. Thus, graded materials are mostly used in the situation where the loading is not uniform. Typically, a non-uniform loading environment is found under dynamic/impact loading such as stress wave propagation, crack propagation, armor perforation, etc. Therefore, the current research of FGM on its mechanical properties is focused on these loading conditions.

1.2.2.1 Stress wave propagating in functionally graded materials

Because of different wave impedance of different FGM components, the wave propagation in the FGM materials is governed by the reflection and transmission at the interface. Tasdemirci and co-workers[33] performed compression tests under dynamic loading using Hopkinson bar and numerical simulations on multi-layered graded material ceramic/metal matrix composites. The wave signals measured in the pressure bars and stress distributions through the thickness are shown in Figure 1.5(a) and Figure 1.5(b).

It indicates that wave impedance mismatching leads to a discontinuous stress distribution in the interface between the different layers and influences the energy absorption capability. Furthermore, the subsequent experimental and numerical studies on metal-ceramic FGM led by Tasdemirci and his co-workers[34-35] show that a

low modulus material in between the metal layer and ceramic layer as an interface could reduce stress wave transmission.

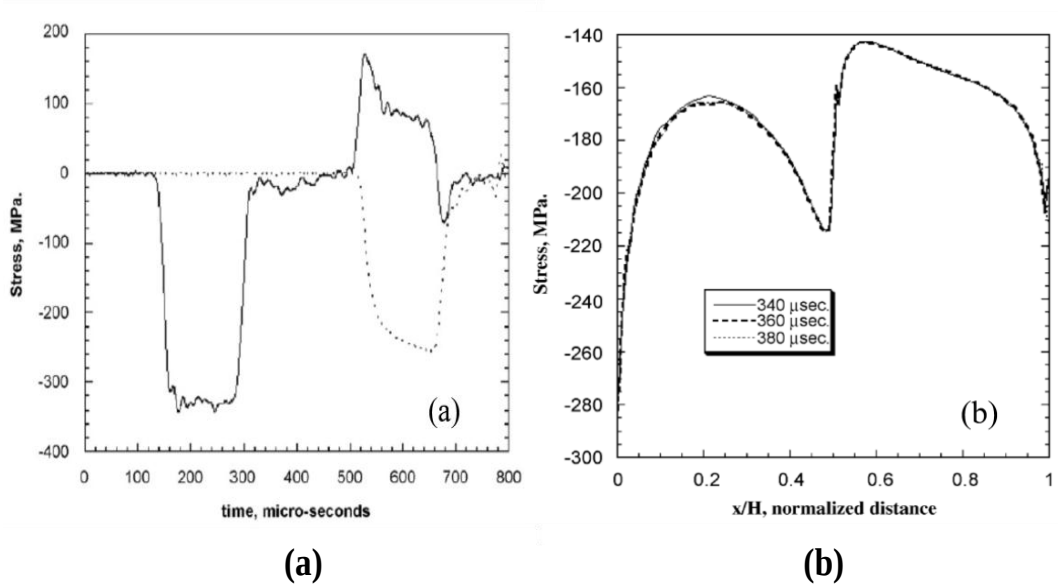


Figure 1.5 Stress-Time curves of the multi-layered graded sheet (a) and axial stress distribution through the thickness for three different time values (b)[33]

Chakraborty and Gopalakrishnan[36] explained by finite element method analysis that the wave propagation in graded materials depends on composition distributions through the thickness. Berezovski and co-workers[37] numerically investigated two-dimensional stress wave propagating in layered FGM and continuous FGM. The numerical results show that the stress wave propagation is closely related with the gradient generated by enhancement phase proportion along the thickness. Han and Liu[38-39] studied numerically the wave propagation in a FGM where the elastic constant and the density vary in the form of quadratic function. Bruck[40] developed even a design method for FGM by studying wave propagating rule in FGM.

Li and Ramesh[41] investigated the dynamic response of functionally graded plates by numerical method. The results show also that wave propagation feature is influenced by composition distributions. It is noticed that such numerical method has a limited layer size and it leads to a discretized analysis as shown in Figure 1.6.

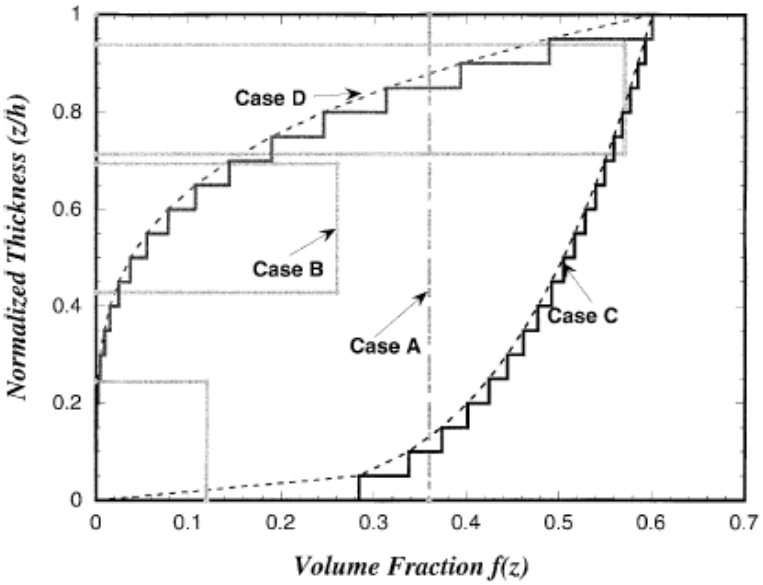


Figure 1.6 The specific gradations investigated by Li[41]

1.2.2.2 Dynamic fracture of functionally graded materials

Li and his co-workers[42] performed compression tests on FGM of Ti6Al4V-Al3Ti under quasi-static loading (0.001/s) and dynamic loading (800-2000/s) in order to study the crack propagation and the damage evolution. The results show that crack density measured for a given macroscopic damage level is higher after dynamic loading than under static case. Masahashi and his co-workers[43] performed shear tests on the rolled Fe-Al alloy and CrMo steel. It is found that the crack starts from the interface and spreads out to base material (CrMo) with increasing strain levels. Eizadjou and co-workers[27] realized tensile tests of Al/Cu multi-layered FGM (obtained through ARB method at room temperature). It is found that the material strength is enhanced and the fracture strain decreased with an increasing rolling passes.

Markaki and co-workers[44] analyzed the energy absorption capacities of various multi-layered metal/ceramic FGM using tensile tests, three-point bending tests and penetration tests. Carreno and co-workers[23] performed indentation tests and notch impact tests and found that the gradient improves impact performance of FGM. They argued that the main reason lies in that the crack can rotate under impact loading and this makes the crack renewing in the next material layer more difficult. Wu and co-workers[24] carried out tensile tests on three layers graded plates obtained by rolling and found that the graded plate has a larger fracture strain. The cross-sectional post-

mortem observation indicates that the voids start near the cracks under a certain strain instead of more dangerous delamination (see Figure 1.7).

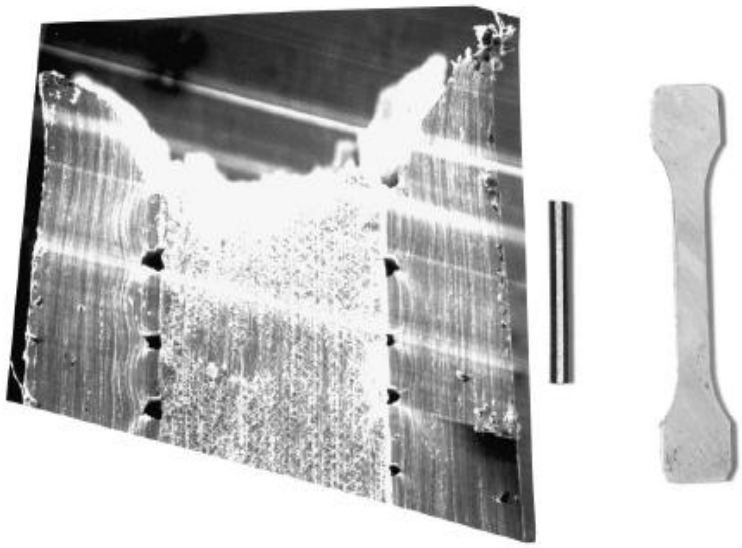


Figure 1.7 A specimen section of three-layer graded laminate sheet: 304ss/UHCS/304ss[24]

1.2.2.3 Armor protecting study on functionally graded materials

The armor protection capability is mainly evaluated by the absorbed energy, target damage and residual velocity of the projectile etc. in the ballistic tests. Figure 1.8 shows a schematic drawing of the penetration of armors.

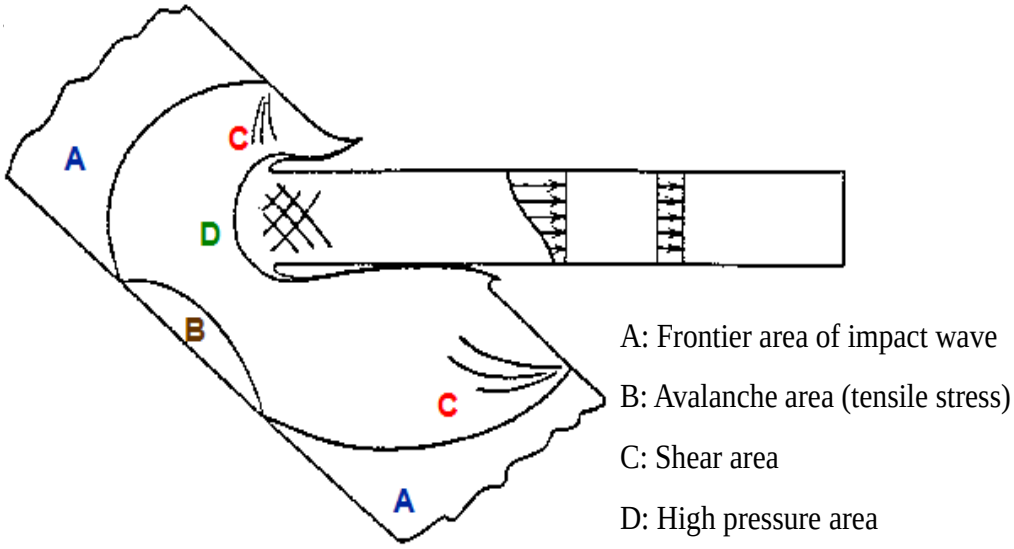


Figure 1.8 Schematic drawing of armor penetration

The contact surface of armor-target suffers from compression stress, while the back surface of the target suffers from tensile stress when penetrating on protecting armor.

Therefore, a good protecting armor requires a back surface with higher tensile strength, a larger fracture strain in a whole, a higher vertical shear resistance and a strong capability of energy absorption[45] .

Yu and co-workers[32,41] performed experiments and numerical research of functionally graded plate made from metal matrix composites in order to investigate the anti-penetration behavior. The location of occurrence maximum stress, the distributions of cumulative strain and the influence of gradient on maximum stress are obtained.

Hetherington and co-workers[46] performed a series of projectile impact tests on various graded plates. The results show that multi-layered graded plate has higher energy absorbing capability than that of equivalent thickness monolithic plate. Wadley and co-workers[31] made high speed impact tests on sandwich structure with 6061-T6 frame filled with Al_2O_3. The penetration resistance has been evaluated by ballistic limit velocity and residual velocity. Drop hammer impact tests on helmets (Hui and co-workers[47]) shows also that multi-layered graded metal/composite materials has an excellent anti-penetration performance.

Fiber/metal graded materials integrate the advantages of metal and composite materials. Fox example, the metal with isotropic properties can resist high impact forces due to high strength and toughness, while the fiber reinforced composite material has good anti-fatigue capability. He and co-workers[48] performed ballistic tests on six groups graded plates with GFRP layered plate at velocity of 70 m/s to investigate their energy absorption performance. The energy absorption capability of graded plates has been enhanced with the increasing portion of GFRP plate. It is also found the multi-layered graded plates with thickness ratio of GFRP of 5% are suitable for protection armors and multi-layered graded plates with thickness ratio of GFRP of 30% are suitable for human body protection.

Puente and co-workers[49] experimentally and numerically performed high speed impact tests on ceramic/polymer/metal gradient armored plates. The influence of polymer thickness on the penetration resistance and the optimal thickness of polymer layer are studied. It shows that the overall properties can be improved by metal/ceramic graded material with a soft material as joining interfaces. Yadav[50]

executed high speed penetration tests on ceramic/polymer/ceramic graded material with aluminum plate as a support. The anti-penetration capability of the target plates evaluated by residual depth of the projectile in the support plates. The results confirm that the anti-penetration capability in multi-layered graded plates is enhanced because the polymer layer reduced the velocity of stress wave propagation and arrested cracks. A number of published works (Radin et al[51], Marom et al[52] ,Corran et al[53] Gupta et al[54], Huang et al[55-56] ,Flores-Johnson et al[57]) shows more or less similar results on various FGM plates at various impact velocities.

Another more exotic study on the graded cellular materials is also reported in the literature. Cellular materials as foams and lattice materials are basically used for the energy absorption under impact loading. As an example single layer sandwich (Figure 1.9a, Liu[58]) or multi-layer sandwich (Figure 1.9b, Wadley et al[59], Wang et al[60]) can be used as protective shielding structure.

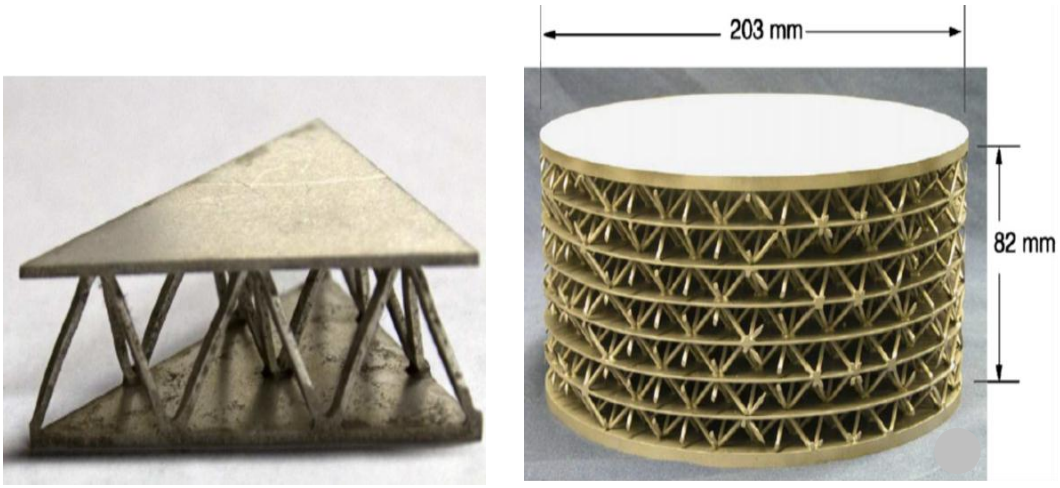


Figure 1.9 Specimens of different lattice structures (a)[58]and(b)[59]

Graded cellular materials can be produced and used as core materials. For example, Zeng and co-workers[29] performed penetration test on graded sandwich structure (see Figure 1.10) under impact velocity of 21m/s and 41m/s to investigate the influence of density/strength gradient on impact behavior of FGM core sandwich. The core layer with density gradient of the specimen lined with arrow is shown in Figure 1.10(a) and the density distribution is shown in Figure 1.10(b).

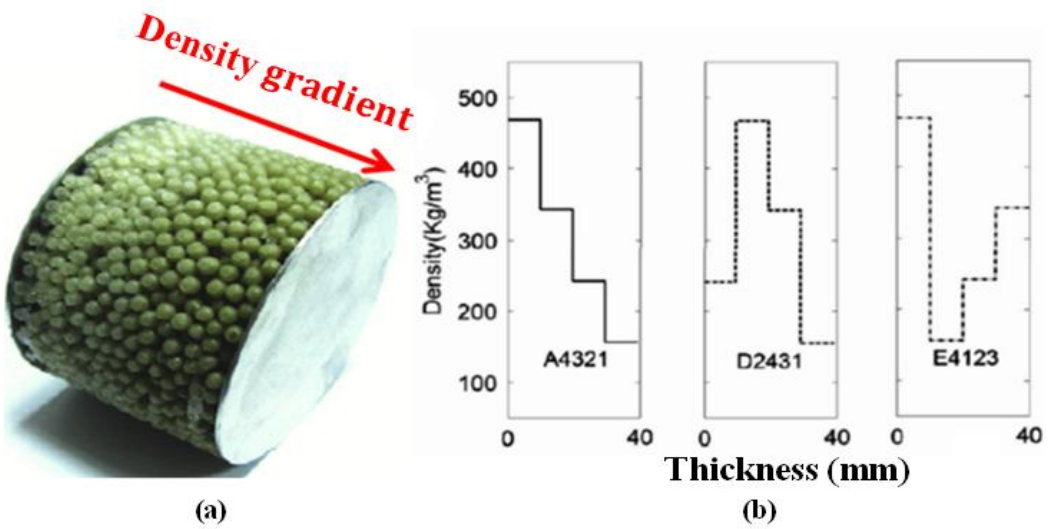


Figure 1.10 Graded specimen(a) and Density profile for the graded specimens(b)[29]

It is found that density gradient has a great influence on the piercing force and the energy absorption.

1.2.3 Summary

The abovementioned research background of FGM shows that the FGM is still a very active research domain. It is interesting not only for material scientist in their manufacturing methods but also for mechanical engineer or scientist in their property understanding.

In mechanical engineering, these investigations are mainly concentrated on the mechanical strength, thermal conductivity, fracture characteristics, and energy absorption capability. The previous studies suggest that the introduction of a property gradient can improve the overall mechanical property, especially under impact loading. Therefore, understanding the mechanical properties of functionally graded materials under impact loading has very important significance in engineering applications.

1.3 Graded sheet metals produced by SMAT

1.3.1 Introduction of Surface mechanical attrition treatment (SMAT)

Surface mechanical attrition treatment (SMAT) is a new approach to effectively upgrade the mechanical properties of treated surface layer of metallic materials[61-62]. It consists of generating grain refinement of treated surface layer by the random large plastic strain due to the random impact of steel balls.

Figure 1.11(a) shows a schematic illustration of the SMAT set-up. Stainless steel balls (shots) of proper diameter were placed at the bottom of a cylinder-shaped vacuum chamber that was vibrated by a generator, with which the shots were resonated. The samples are fixed at the top of the chamber. Because of the high vibration frequency of the system, the sample surface to be treated was peened by a large number of shots in a short period of time. Each peening of the ball to the surface will result in plastic deformation in the surface layer of the treated sample (as shown in Figure 1.11(b)).

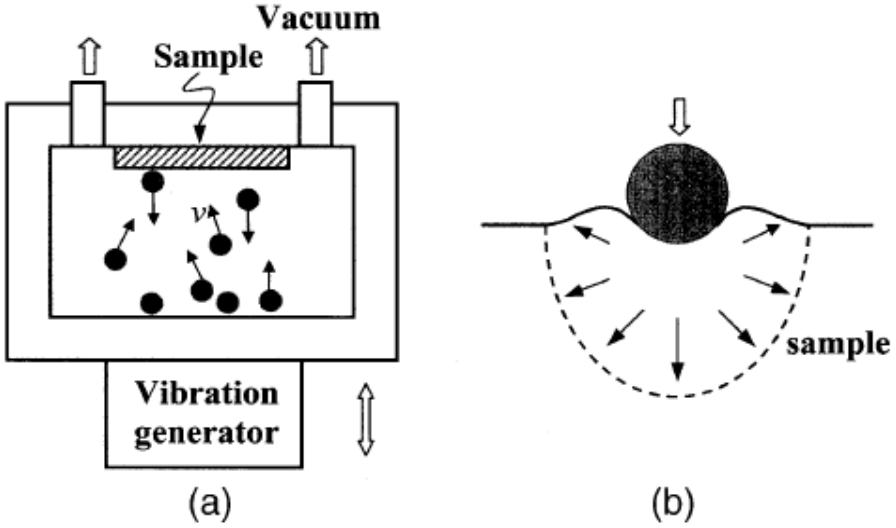


Figure 1.11 Schematic illustrations of the SMAT set-up(a)and the localized plastic deformation in the surface layer by the impacting of the shot(b)[63]

As a consequence, repeated multidirectional peening at high strain rates onto the sample surface leads to severe plastic deformation in the surface layer. It is observed that the yield stress of SMAT treated sheet metals can be outstandingly increased without significant reduction in the ductility after SMAT. This phenomenon is explained by the grain-size refinement (up to nano scale) in the surface layers. SMAT has been utilized for a number of materials. For example, a SMAT treated commercial pure titanium has a nanostructured surface layer up to 50 μm thick[64]. It is also observed that there is no obvious interface between the nanostructured surface layers and the base layer. Thus, the SMAT is considered as a new attempt to produce the

multi-layered graded sheet metals without any discontinuity between the graded layers.

It is also possible to combine SMAT with other bonding methods. For example, Chen and co-workers[65] produced a new multi-layered graded material with higher yield stress and fracture strain than monolithic material using accumulative roll bonding method to joint SMAT treated layers.

1.3.2 SMAT treated graded AISI304 stainless steel sheet

AISI304 austenitic stainless steel sheet is a widely used engineering material. It is reported[66] that the SMAT treated AISI austenitic stainless steel sheet has a much higher yield stress and a higher fracture strain as well. There is a real potential for a wide industrial use of such somehow enhanced materials. It is then necessary to further understand its mechanical properties and finally a pertinent material model.

The main microstructural feature of SMAT treated austenitic stainless steel sheet is the gradient of grain-size induced along the thickness direction, which leads to multi-layers with graded mechanical properties. Such a microstructural feature is easily checked by micro indentation test through the thickness of sheet. A micro-indentation test provides a hardness measurement for materials from the past three decades. It could be roughly related with the yield stress of the material at the indented location. So far, it is even a common method for determining materials properties used in small-scale analysis, such as hardness and Young's modulus of materials[67-68], the residual stress[69-72] and plastic properties of materials[73-86].

Figure 1.12(a) shows a typical procedure of hardness measurement of our 1mm thick AISI304 austenitic stainless steel sheet treated with SMAT at the both sides. The treated plate was cut through the thickness and put into an epoxy support. After polishing of the surface, a number of indentation tests were made with a regular distance (each 0.2 mm) along the thickness direction and the hardness profile through the thickness are obtained.

Figure 1.12 (b) shows the hardness profiles of SMAT treated AISI304 austenitic stainless steel sheet compared with the hardness profile of original (as received) AISI304 austenitic stainless steel sheet. The black dotted line and the red dotted line represent the hardness of material treated by SMAT and the material as received respectively. This hardness measurement reveals that the SMAT induces a gradient of

hardness and thus a gradient of yield stress. It shows also an important enhancement of yield stress after SMAT.

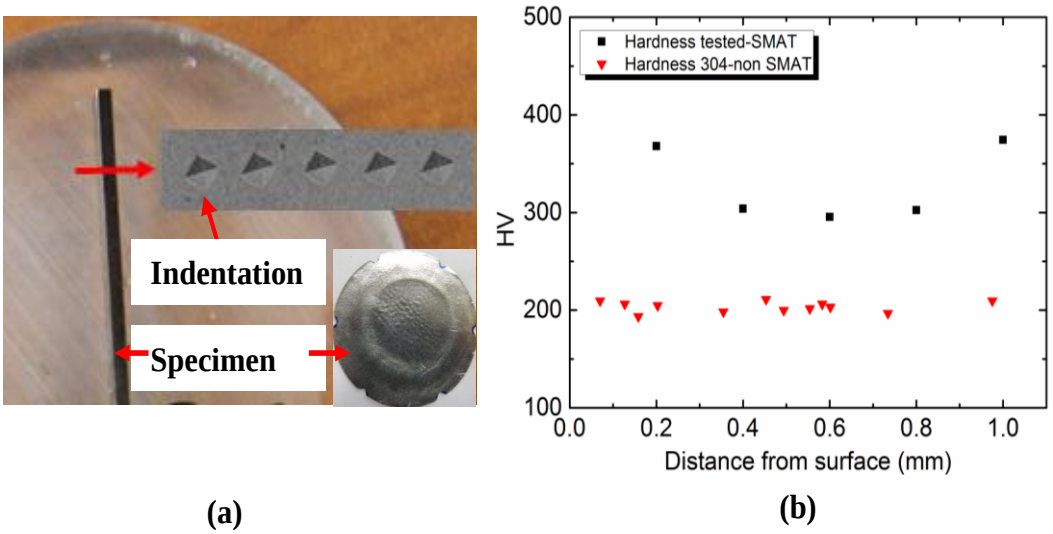


Figure 1.12 Indentation specimen (a) and Victor hardness (b)

The overall true stress-strain curves[87] were also obtained by the common tensile test using MTSRT-50 tensile testing machine. The geometry of dog-bone shaped tensile specimen is described by Figure 1.13.

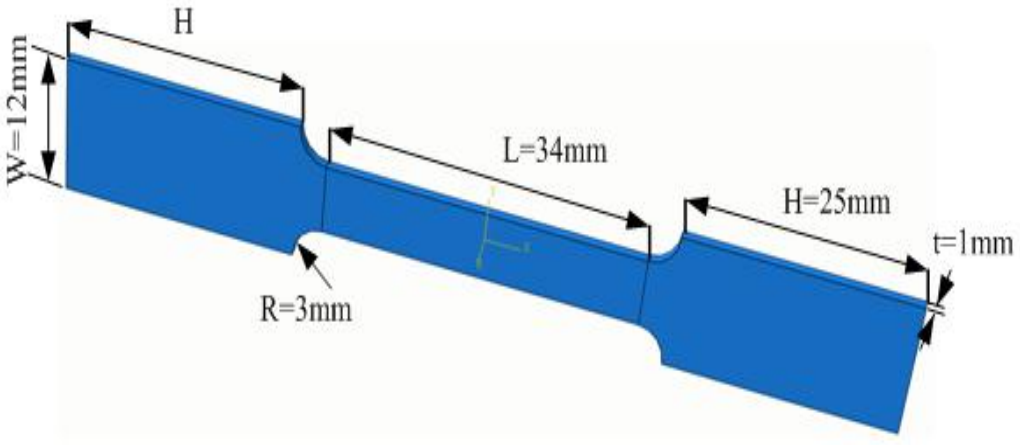


Figure 1.13 The geometry of dog bone tensile specimen

More intrusive tests can be realized to further determine the mechanical properties of different layers. One can remove the upper and lower outer surfaces and carry out the same tensile test on the remaining part of the specimen.

The true stress strain curves of various tensile tests are shown in Figure 1.14. The four following types of specimen are used:

(1) 1mm thick AISI304 austenitic stainless steel as received;

(2) 1mm thick AISI304 austenitic stainless steel with SMAT at both sides;

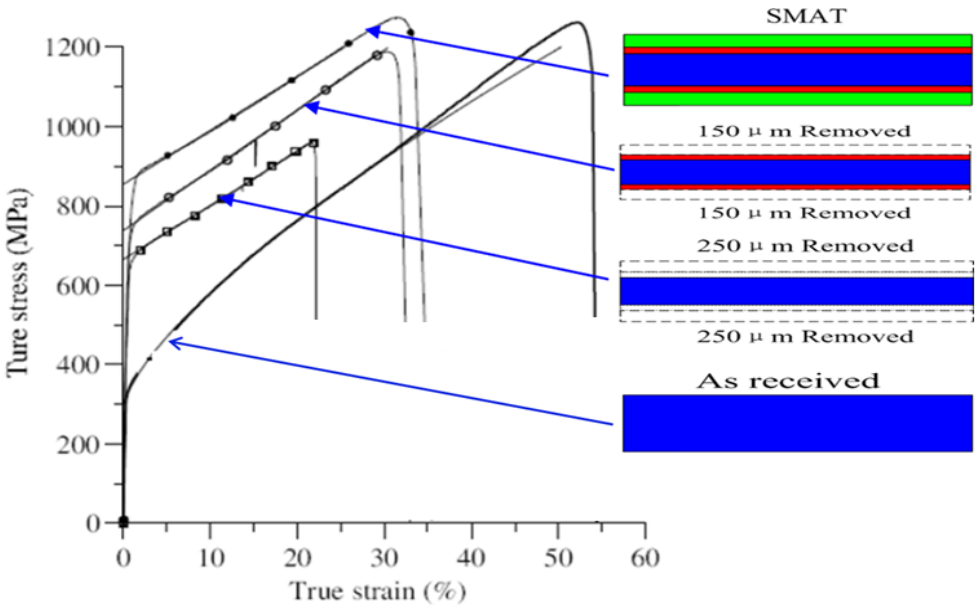


Figure 1.14 True stress-strain curves of the treated and as-received AISI304 stainless steel of 1mm thickness and different testing states of specimens

(3) 0.7mm thick AISI304 austenitic stainless steel with SMAT at both sides with the 0.15mm upper and lower surfaces removed.

(4) 0.5mm thick AISI304 austenitic stainless steel with SMAT at both sides and removed the upper and lower surface of 0.25mm each.

Such tensile results[87] are in good agreement with the hardness profile shown in Figure 1.12b. It confirmed that SMAT treated AISI304 austenitic stainless steel has an enhanced yield stress and a gradient of yield stress through the thickness.

1.4 Aims and outlines of dissertation

The research work described in this dissertation aims at investigating the mechanical properties under impact loading of SMAT treated AISI304 austenitic stainless steel sheet. On one hand, AISI304 stainless steel is a widely used industrial material and a cheap SMAT treatment induces an important mechanical strength enhancement with a limited fracture toughness loss. All these advantages lead potentially to an important industrial application. On the other hand, AISI304 stainless steel is naturally a multi-layer functionally graded material with perfect bonding by its manufacturing path and the property gradient has a significant effect

on the structural response under impact loading. Furthermore, this property gradient can be controlled by the intensity and duration of the SMAT treatment. SMAT treated AISI304 austenitic stainless steel sheet is therefore an excellent candidate for energy absorbing system as well as armor design.

For this purpose, a comprehensive study of the mechanical behavior of SMAT treated AISI304 austenitic stainless steel sheet under impact loading is desired. In this Ph.D research work, first of all, the overall rate sensitivity of mechanical behavior is evaluated by the double shear tests with a large diameter Split Hopkinson Pressure Bar (SHPB). Numerical models are used afterwards to identify material parameters (yield, hardening and damage) of each layer by the inverse method from the quasi-static tensile tests already presented in the previous section of this introduction. Assuming that the rate sensitivity is homogeneous in different layers, a multi-layer rate sensitive constitutive model is built.

In order to validate this multi-layer rate sensitive constitutive model, structural penetration tests under quasi-static and impact loading using a Hopkinson bar are performed. The testing results are in good agreement with the simulated results using our multi-layer rate sensitive constitutive model and this validates the multi-layers material model. Further optimization of the gradient profile for a better anti-penetration response is finally proposed.

The content includes of six chapters:

The first chapter is a general introduction. The FGM related topics such as the interest, history background, manufacturing path, and their properties are summarized. Afterwards, the surface mechanical attrition treatment (SMAT) and the induced graded materials are described. Finally, we focused on SMAT treated AISI304 austenitic stainless steel sheet which is the subject of this Ph. D work.

The chapter 2 describes the double shear testing of SMAT treated AISI304 austenitic stainless steel sheet using SHPB technique. The history and the principle of the SHPB and the plane-shear tests are introduced at first. Quasi-static and impact double shear tests are carried out on the SMAT treated AISI304 austenitic stainless steel specimen. Force vs displacement curves at different loading rate are obtained. A nominal average strain-stress related at various strain rates can be extracted.

Unfortunately, the stress-stress curve of tested material cannot be easily derived from the directly measured force and displacement time histories in this double shear test. Indeed at the early stage, equilibrium state is not yet reached. At final stage, the

strain is too big to use small strain assumption. Therefore, we introduce in the third chapter the numerical simulation for double shear using ABAQUS. It allows analyzing the influences of the length of shear zone and the clamping fixtures on the strain uniformity in the shear zone, which is important for the behavior at the early loading stage. For the final stage of loading, the strain defined in finite element software is analyzed and it is ultimately found that we should use the Eulerian cumulative equivalent strain and the equivalent Cauchy stress respectively.

The chapter 4 reported an inverse method to identify the material parameters to describe the yield stress, strain hardening as well as damage until final fracture. It is on the basis of numerical simulation of quasi-static tensile tests of specimen with and without removal of outer surfaces. Finally, a multi-layers models for the SMAT treated AISI304 austenitic stainless steel sheet is proposed. Validation is made with a piercing test on the SMAT treated AISI304 austenitic stainless steel.

Chapter 5 presented at first the penetration tests of a target made of the SMAT treated AISI304 austenitic stainless steel sheet under dynamic loading using Hopkinson pressure bar. Assuming that the rate sensitivity of different layers is homogeneous, a multi-layers rate sensitive elastic-plastic damageable model is built with parameters identified in chapter 4. The numerical simulation of the penetration test using ABAQUS/Explicit can be performed. The good agreement between numerical and experimental results validates this multi-layers rate sensitive elastic-plastic damageable model and the numerical penetration models. It allows to explore numerically the optimal material gradient design for the anti-penetration performance.

The final chapter is the conclusion.

Chapter 2 Rate sensitivity of SMAT treated AISI304 austenitic stainless steel sheet

2.1 Review of Split Hopkinson pressure bar technique

2.1.1 Set-ups of Split Hopkinson Pressure Bar

Hopkinson Pressure bar technique was invented in 1914[88] and modified as Split Hopkinson pressure bar in 1949[89]. It has become nowadays the most widely used testing method. It is mainly used to characterize the mechanical properties of materials in the strain rate range between 10^2/s-10^4/s. A typical SHPB set-up is shown in Figure 2.1. It is composed of long input and output bars with a short specimen placed between them. A projectile launched by a gas gun strikes the free end of the input bar and develops a compressive longitudinal incident wave $\varepsilon_I(t)$. Once this wave reaches the bar/specimen interface, part of it $\varepsilon_R(t)$, is reflected, whereas the other part goes through the specimen and develops the transmitted wave $\varepsilon_T(t)$ in the output bar. Two gauges are cemented at the midpoints of input and output bars to record those three basic waves which can be used to investigate the constitutive behavior of the specimen.

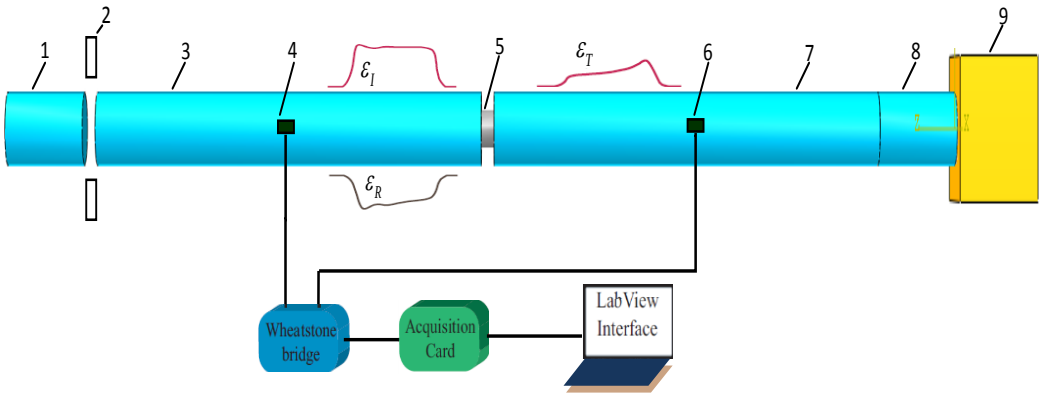


Figure 2.1 The schematic drawing of Hopkinson bars

1. Impactor; **2.** Laser velocimeter; **3.** Incident bar; **4.** Strain gauge; **5.** Specimen; **6.** Strain gauge; **7.** Transmitted bar; **8.**Energy absorption bar; **9.** Bumper

The Split Hopkinson Pressure Bars are based on the one-dimensional wave propagation theory. Therefore, one can calculate the stress as well as the particle velocity from the strain history. It is also possible to time shift the measured signal at the position of strain gage to the pressure bar end in contact with the specimen. From specimen viewpoint (Figure 2.2), those three waves are simultaneously at the bar specimen interfaces.

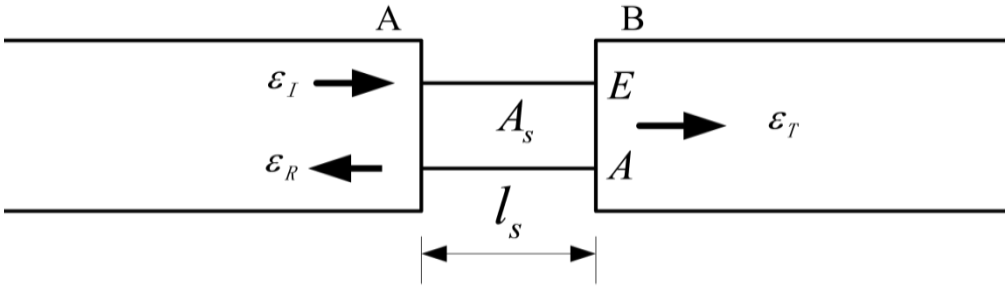


Figure 2.2 The schematic drawing of waves at bar specimen interfaces

With the superimposition principle, force and velocity on the specimen-bar interface can be calculated from the incident signals, reflected signals and the transmitted signals by the following formulas (2.1)

$$F_{input}(t) = AE(\varepsilon_I(t) + \varepsilon_R(t)) \qquad V_{input}(t) = C_0(\varepsilon_I(t) - \varepsilon_R(t))$$
$$F_{output}(t) = AE\varepsilon_T(t) \qquad V_{output}(t) = C_0\varepsilon_T(t) \tag{2.1}$$

where A and E are respectively the cross section area and Young's Modulus of Hopkinson bars, C_0 is the elastic wave speed in bars.

For a short metallic specimen, one can assume besides:

1) The stress and strain fields in the specimen are homogenous;

2) The inertia effects of specimen under dynamic loading can be ignored;

3) The friction between the specimen and the ends of input and output bars is negligible.

A nominal average strain rate, strain and stress of the tested specimen can be calculated from the basic waves:

$$\dot{\varepsilon}_s(t) = \frac{d\varepsilon}{dt} = \frac{2C_0}{l_s}\varepsilon_R(t) \tag{2.2}$$

$$\varepsilon_s(t) = \frac{2C_0}{l_s}\int_0^t \varepsilon_R(t)\,dt \tag{2.3}$$

$$\sigma_s(t) = E\left(\frac{A}{A_s}\right)\varepsilon_T(t) \tag{2.4}$$

where $\varepsilon_I(t)$ and $\varepsilon_T(t)$ are respectively the reflected and transmitted strain pulses measured by strain gauges, A_s is the area of specimen cross section, l_s is the specimen length.

2.1.2 Some specific problems in SHPB technique

2.1.2.1 Large diameter pressure bar/Viscoelastic pressure bar

Traditional SHPB uses small diameter pressure bar (about 10mm) to meet the one dimensional wave propagation assumption. However, when the rock, ceramic and concrete should be tested for military or civil engineering applications, large size of specimens is needed to ensure the validation of the experimental results. Therefore, large diameter SHPB has been developed for characterizing the dynamic properties of these materials. For example, Gary and Bailly[90] performed experiments on concrete using Hopkinson bar with diameter of 80mm. Fandrich and co-workers[91] investigated the fracture mechanism of solid grains using Hopkinson bar with diameter of 100mm.

Another practical difficulty is low resistance of cellular material such as honeycomb, foam-like materials because the signal/noise ratio in the metallic pressure bar is too small. The pressure bar of low acoustic impedance should be used. For example, Zhao[92-93] established nylon SHPB with diameter of 60mm to test mechanical performance of bulk cellular materials.

2.1.2.2 Wave dispersions in the time shift of measured impulse

The Hopkinson bar measurement is based on one-dimensional elastic wave theory. According to this theory, the strain signals are not only known at the measuring points but everywhere in the bar because an elastic wave can be shifted to any distance without distortion. However, the one-dimensional wave theory is not always true especially for the large diameter bars, and the geometrical effects should be taken into account. In fact, there are wave dispersion effects during the propagation of waves in elastic or viscoelastic bars. For the classical Hopkinson bars, the ratio of bar diameter over bar length is small enough and this wave dispersion effect is negligible. While for large diameter Hopkinson bars, the wave dispersion effects should be taken into account. In general, a correction of dispersion on the basis of the

theory of three dimensional stress wave propagating in infinite cylindrical rod by Pochhammer and Chree[94-95] can be applied.

Moreover, when the viscoelastic pressure bars are used, the traditional correction methods on wave dispersion are not suitable anymore and a correction on the basis of 3D viscoelastic wave propagation should be chosen.

2.1.2.3 Inertia effect and friction effect

In a SHPB test, the energy received by the specimen from the pressure bar is not only converted to the strain energy, but also lateral kinetic energy and horizontal kinetic energy. Therefore, the strength of the specimen is overestimated if those inertia effects are not taken into account. Another problem is the unavoidable friction in the compression tests.

However, it is also possible to eliminate the additional stress caused by inertia effect and minimize the friction to determine more realistic experimental results. For example, Davis and Hunter[96] proposed a formula to correct the effect of inertia.

$$\sigma = \sigma_0^m - \rho_s\left(\frac{1}{8}v_m^2 D_m^2 - \frac{1}{6}l_m^2\right)\frac{\partial^2 \varepsilon}{\partial t^2} \tag{2.5}$$

Klepezko and Malinowski[97] proposed a formula to take account of friction effect.

$$\sigma = \sigma_0^m - \left(1 - \frac{v_s d_s}{3l_s}\right) \tag{2.6}$$

where， σ_0^m is the measured stress in the specimen, ρ_s is the density of the specimen, v_s is the poisson's ratio of the specimen, d_s is the diameter of the specimen, and l_s is the length of the specimen.

2.2 Experimental techniques for characterizing the SMAT treated AISI304 austenitic stainless steel sheet using SHPB

2.2.1 Choice of testing technique

In order to characterize the rate sensitivity of the mechanical behavior of the SMAT treated AISI304 austenitic stainless steel sheet, SHPB as a universal testing technique for impact loading should be used. The conventional SHPB compression test cannot be applied for this thin sheet metal because of buckling concerns. The impact tensile Hopkinson bar test requires specific device as well as a special attachment design to avoid early failure at the attaching location or the huge peak force at the early stage of the test due to contacting imperfections.

The remaining possibility is the plane shear test which is usually considered as a complementary tool to the standard tensile tests for sheet metals, especially when the plastic criterion is desired. Actually, the shear test has even following advantages: it permits to realize large strain loading without geometric instability (till 80%). Besides, as the plane shear area is very small, at the same impact speed, the strain rate is much higher. For all this reason, shear test is chosen to characterize the rate sensitivity of the SMAT treated AISI304 austenitic stainless steel sheet.

2.2.2 Review of impact plane shear test

The pioneer work of Iosipescu[98] introduced the in-plane single shear fixture for sheet metals under quasi-static loading. Figure 2.3(a) shows the basic principle of such a concept. Such a fixture was afterwards applied to polymer testing[99] and composites testing[100]. The well-known Arcan fixture[101] to generate in plane combined tension-shear was quite close to this basic concept. However, the shortcoming of such testing figuration with a single shear zone is the requirement of a rigid clamping system.

Yoshida and Myauchi[102] proposed symmetric double shear configuration under quasi-static tests (Figure 2.3(b)). It improves the stability of the clamping system due to the symmetric geometry.

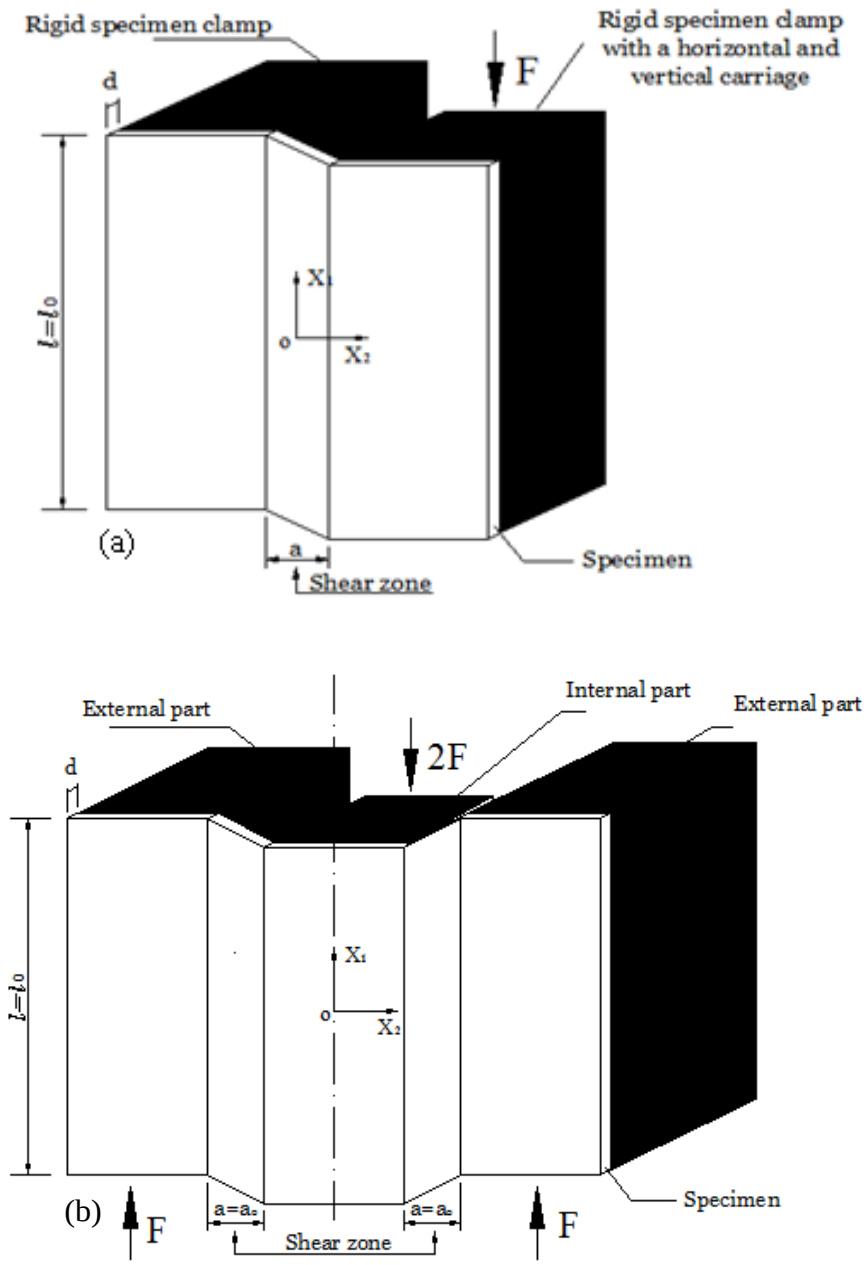


Figure 2.3 Configuration of shearing specimen in tests(a)single shearing zone and (b)double shearing zone[103]

Careful attention should be paid to the geometry of in-plane shear specimen. The length of the shear zone and the width of the specimen should satisfy certain requirements (seeing in figure 2.4). For example, the ratio of width and thickness of the specimen needed to be small enough, namely l/a<10 to avoid buckling of the shearing zone. Meanwhile, the ratio of width and length of the specimen should be small enough (l/L_0<1/10) as well to ensure a large homogeneous shear zone.

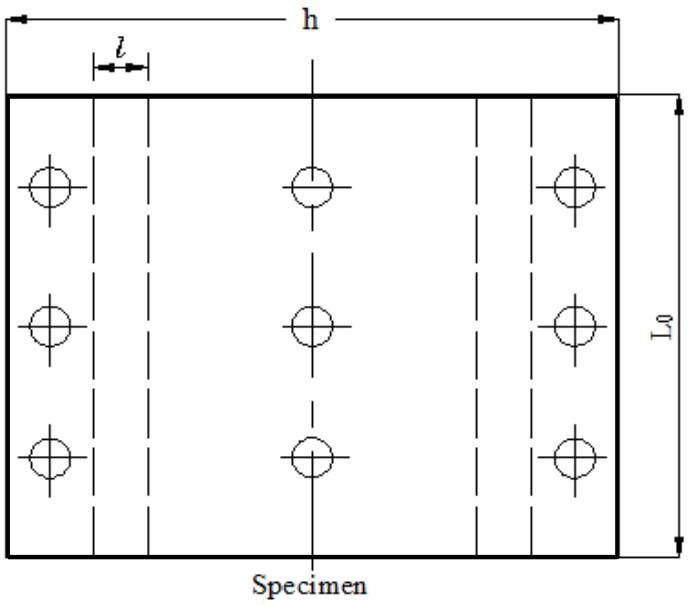


Figure 2.4 The double shearing specimen[103]

where, *l* is the width of shearing area, h is the total width of the specimen, L_0 is the total length of the specimen.

Under dynamic loading, shearing tests were initially performed by Campbell and Ferguson(1970)[103]. They put a double-notched specimen directly in contact with an input Hopkinson bar and an output Hopkinson tube. Figure 2.5 provides a schematic drawing of this configuration (see Guo et al. [104]).

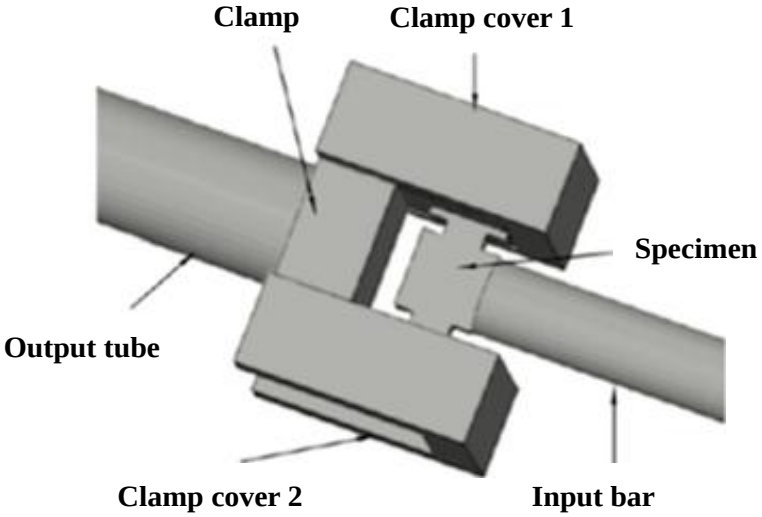


Figure 2.5 Clamping fixture for small shearing specimen[104]

However, a small double-notched specimen (gage length of 0.8mm) was used because of the small size of Hopkinson bars. It leads to an important error due to the non-homogeneous shear strain and also to the severe plastic deformation of the

specimen supports. Modifications of the specimen geometry in order to reduce testing error was also reported[105] but with a limited improvement because the gage length is fixed.

In order to overcome this difficulty and to adopt a bigger specimen as used in most quasi-static cases, an additional co-axis clamping device is designed and placed in between a large diameter Hopkinson bar system. This technique was initially reported by Klepaczko and co-workers[106] and Gary and Nowacki[107] with respectively 30mm and 40mm diameter aluminum bar.

This new technique offered rather good result provided that there is no impedance jump between clamping device and the Hopkinson bars and the wave dispersion effect is well taken into account in the data processing. Even larger system (60mm diameter Hopkinson bar+clamping device) was also reported and it is proven that the plane wave assumption is still valid in this case[108]. Figure 2.6a shows the overall setup of this testing configuration and Figure 2.6b depicts the photo of 60mm large diameter SHPB together with the clamping devices.

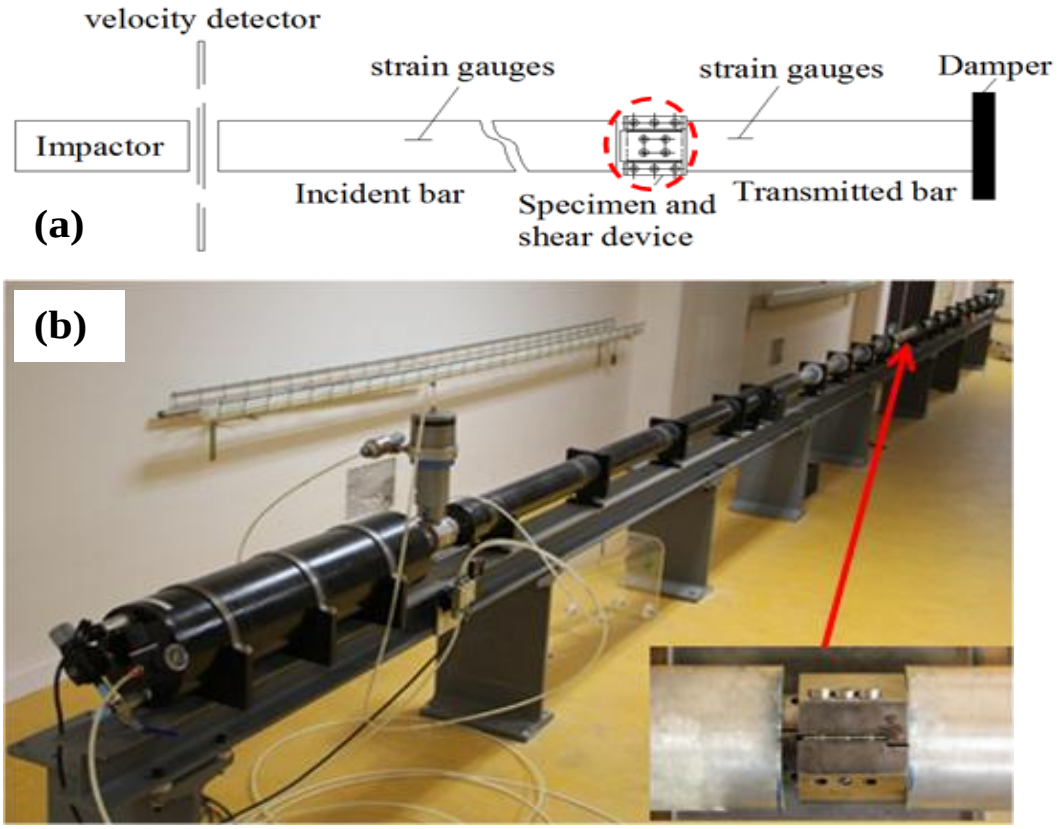


Figure 2.6 The schematic drawing of double shearing tests(a) and Large diameters Hopkinson bar set-up(b)

The double shear clamping device is composed of two coaxial pieces made of high strength steel. The principle is schematically shown in figure 2.7.

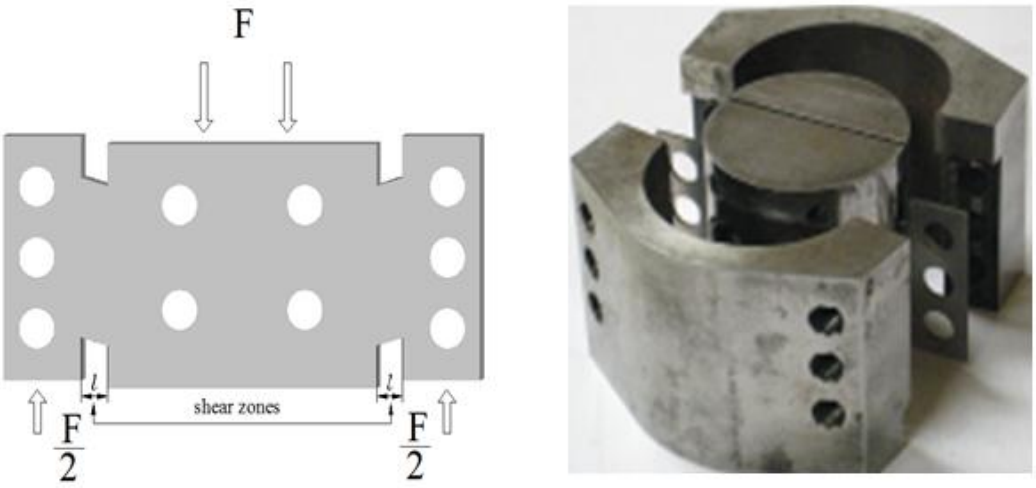


Figure 2.7 Double shear specimen and clamping device

The inner rectangular part of the specimens clamped by the inner coaxial part with griping teeth aligned on the border of the shear area. The two external rectangular parts of the specimen are clamped by the external coaxial pieces with griping teeth aligned at the boundary. When the two coaxial pieces move relatively, the two rectangular zones (width *l*) between inner and external coaxial pieces are sheared.

Quasi-static tests can be simply performed by putting the clamped specimen into a classical hydraulic testing machine. Dynamic tests can be realized by placing the clamped specimenin between the two Hopkinson pressure bars. It is of course necessary to ensure that the inner and external clamping pieces have the same acoustical impedance that equals to the pressure bar's impedance to avoid spurious oscillations. In particular, the studied device is designed for aluminum bars with a diameter of 60 mm. Thus, the overall specimen size (Figure 2.7, left) is of 60mm long and 30mm high. The clamping pieces have a length of 40mm.Technical details can be found in (Merle, 2006)[109].

However, with this new possibility of shear specimen geometry, it is still necessary to respect the limitation of the thickness/width ratio as well as width/length ratio of the shear area to prevent the buckling and instabilities[110].

2.2.3 Double shear test on the SMAT treated AISI304

austenitic stainless steel sheet under quasi-static and dynamic loading

2.2.3.1 Specimen and fixture clamping

The double shear specimen was cut from 1 mm thick raw AISI304 stainless steel sheet. Its chemical compositions are the following: Cr (18.3%), Ni (8%), Mn (0.9%) and Si (0.6%). Figure 2.8a illustrates the dimension of the specimen with an overall length of 62 mm and a width of 30 mm. The shear zones marked with a width of 3 mm has a reduced length of 20 mm in order to obtain a better clamping condition.

Shear zones can be SMAT treated on the both sides. A photo of the SMAT treated specimen as well as the details in the shear zones are presented in figure 2.8b.

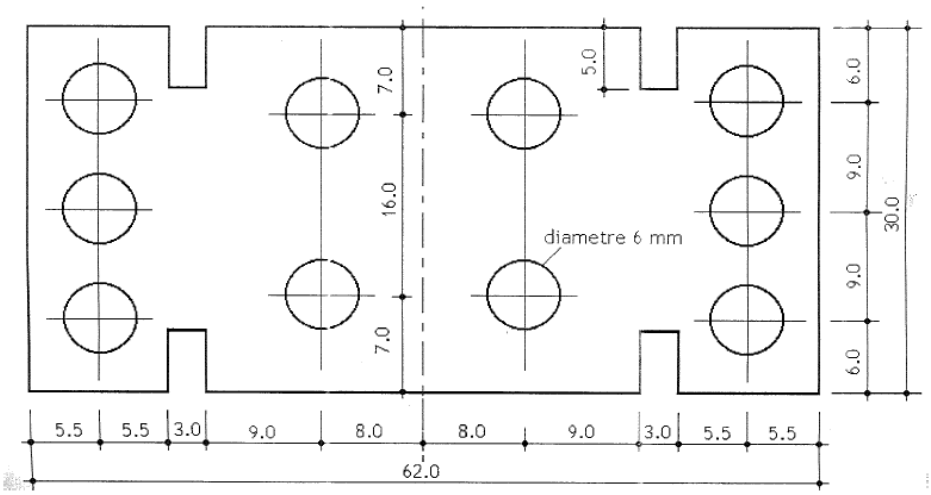


Figure 2.8a

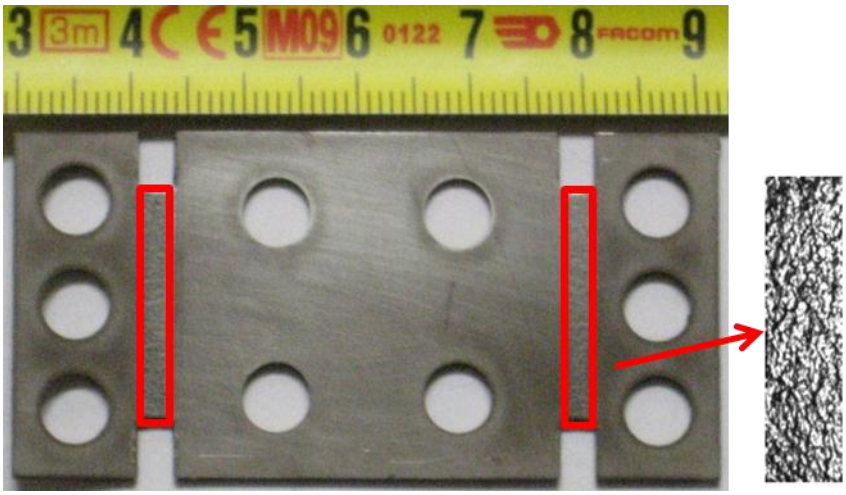


Figure 2.8b Photo of specimen and the detail of SMATed shear zone

Figure 2.9 shows the clamping devices composed of inner pieces, outer pieces,

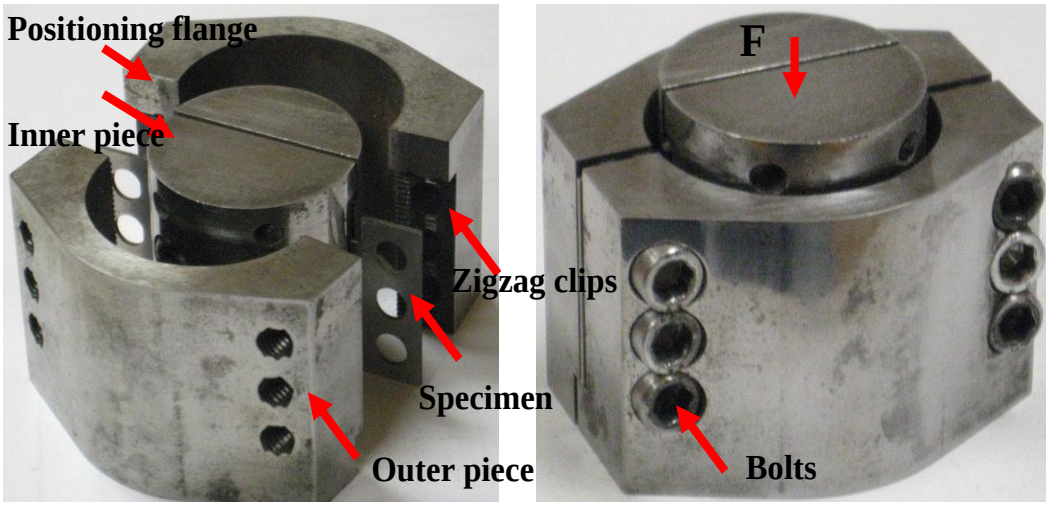


Figure 2.9 Double shearing specimen and fixture clamping device

positioning flange, zigzag clips for avoiding glide between the clamps and the specimen. Bolts of M8 are used to fix the specimen in the clamps.

An additional device is used in the assembling procedure in order to guide all the clamping pieces and to ensure the parallel end faces between the inner and external clamping pieces(Figure 2.10). A moment of 20Nm is applied on the bolts, which is found as a good compromise to avoid the damage caused by zigzag clips on the specimen.

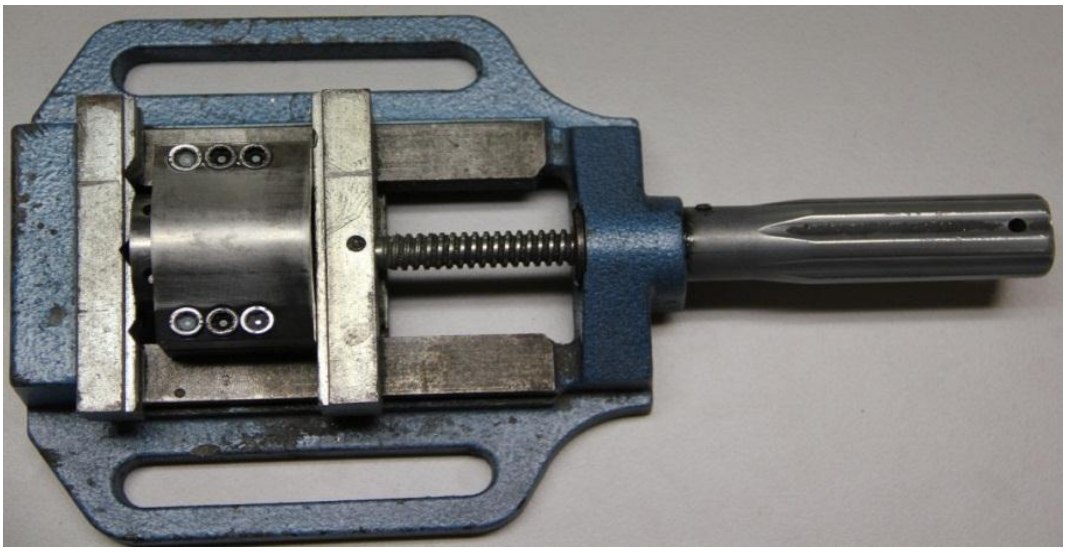


Figure 2.10 Located devices for the shearing test

2.2.3.2 Quasi static and impact loading details

The assembly of the clamping device and the SMAT treated AISI304 austenitic stainless steel specimen can be put in the universal Tension/Compression INSTRON3369 machine to perform quasi static double shear test. The force and displacement is directly measured by testing machine. Anyway, to ensure the accurate experimental results, the machine rigidity is measured before testing. In the data processing, the deformation of the crossbeam is then removed.

It can be also placed in between the 60mm Aluminum Hopkinson bar including an incident bar of 4500 mm long and a transmitted bar of 2000 mm (as shown in Figure 2.6) to perform dynamic tests. The tension impulses of three basic waves are recorded by the signal acquisition chain.

2.2.3.3 Data processing details for impact double shearing tests

As aforementioned, the use of large diameter Hopkinson bar will lead to wave dispersion. Careful data processing is needed to obtain accurate results. For example, the correction of this dispersion effect on the basis of a generalized Pochhammer's wave propagation theory is consequently performed in data processing. Besides, the calibration of the measuring chain is quite important in order to obtain credible experimental results because many factors such as the coefficient of gauges, gain of the amplifier might vary with time.

With all the necessary precaution on the signal processing, the measured tension corresponding to the three basic waves (incident, reflected and transmitted) can be converted to strain and time shift correctly to the bar specimen interfaces. It is noted that the clamping device is considered as a short extension of the pressure bars because their acoustic impedance is the same as the pressure bar.

Figure 2.11 depicts these three waves. There is no sharp peak related with a bad contact, nor high-frequency oscillations related with the successive reflections within the clamping device. These waves demonstrated influences of the complex clamping device could be more or less neglected.

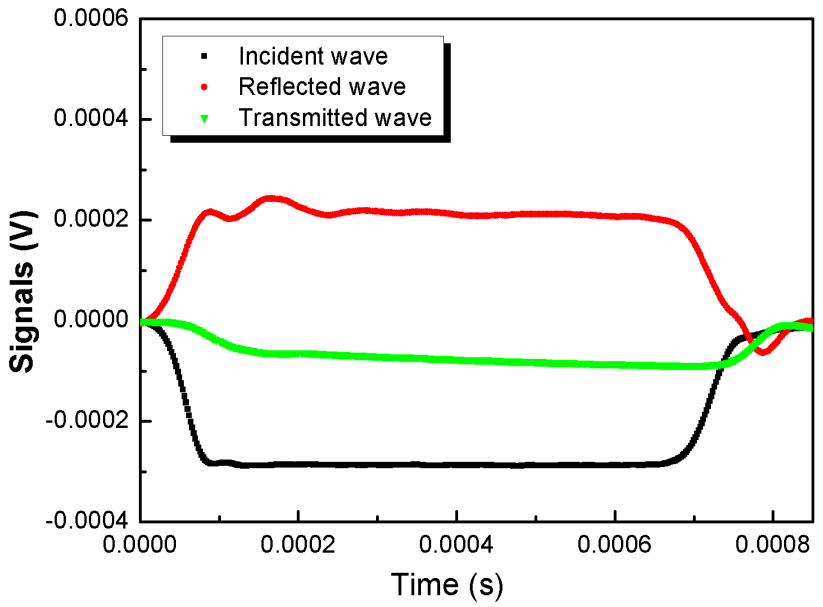


Figure 2.11 Curves of stress wave in the specimen

The force and the velocity on the specimen-bar interface can be calculated from the three waves by formulas (2.7).

$$F_{input}(t) = AE(\varepsilon_I(t) + \varepsilon_R(t)) \qquad V_{input}(t) = C_0(\varepsilon_I(t) - \varepsilon_R(t))$$
$$F_{output}(t) = AE\varepsilon_T(t) \qquad V_{output}(t) = C_0\varepsilon_T(t) \tag{2.7}$$

Figure 2.12 shows the two forces time history. It can be seen that an equilibrium state is rather rapidly reached.

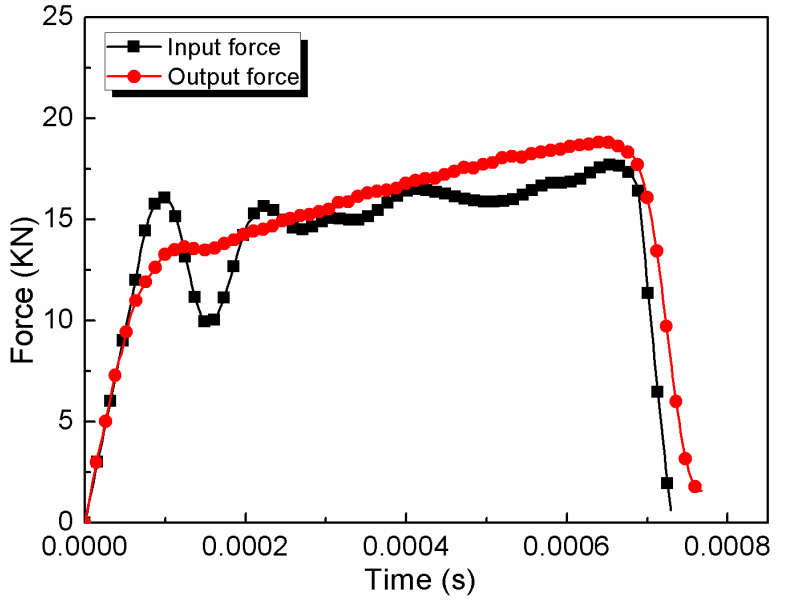


Figure 2.12 Comparison of input force and the output force

The displacement can be calculated by the time integral of the difference of input and output velocities(Equation 2.8),

$$\Delta(\mathrm{T}) = \int_0^T (V_{Output}(t) - V_{input}(t)dt) \tag{2.8}$$

A relationship between force and displacement time history can be obtained as in a quasi-static test (Figure 2.13).

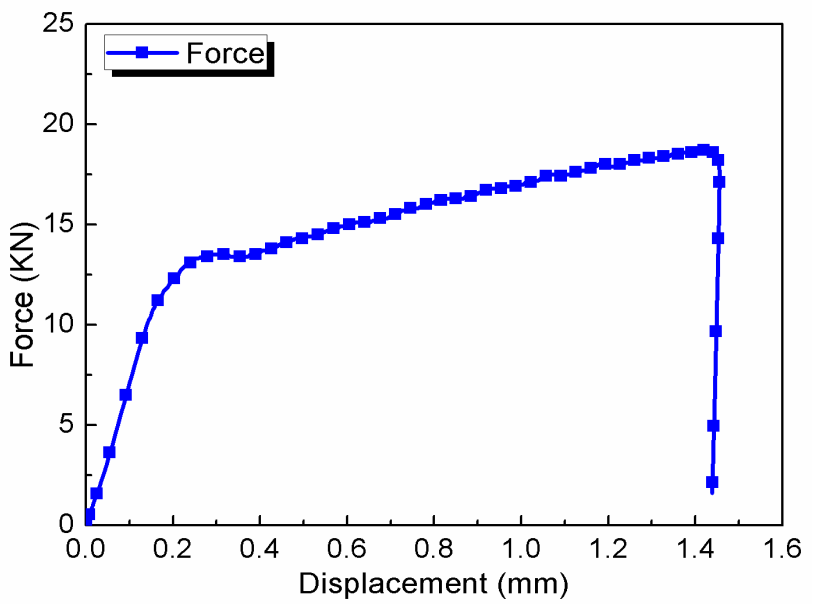


Figure 2.13 Curve of displacement and force

2.2.3.4 Average nominal stress-strain relation

From the basic measurements of such a test which are the force F and the relative displacement d of the shear zone (see also Figure 2.14), a nominal stress/strain relation can be extracted. It is noted that the impact shear test provides rather indirectly the measurement of force and displacement as shown in the previous sections while the quasi-static test provides them directly.

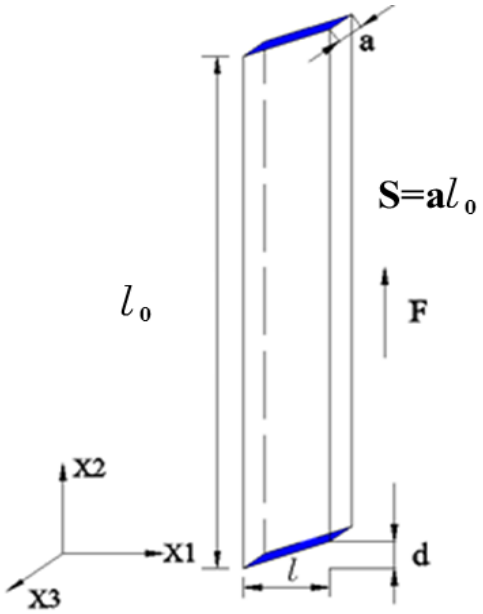


Figure 2.14 The schematic drawing of simple plane shear

Actually, one can assume for the simplicity a pure shear state where the strain state and stress state are expressed as following,

$$\varepsilon = \frac{1}{2}\begin{bmatrix} 0 & \gamma & 0 \\ \gamma & 0 & 0 \\ 0 & 0 & 0 \end{bmatrix} \quad \sigma = \begin{bmatrix} 0 & \tau & 0 \\ \tau & 0 & 0 \\ 0 & 0 & 0 \end{bmatrix} \tag{2.9}$$

where $\gamma = d/l$ is the shear strain. Classical equivalent strain can be calculated with the measured displacement d (Equation 2.10) and equivalent stress with the force F (Equation 2.11) if von Mises criterion is assumed.

$$\varepsilon_{eq} = \frac{d}{l\sqrt{3}} \tag{2.10}$$

$$\sigma_{eq} = \tau\sqrt{3},\ \tau = \frac{F}{S} \tag{2.11}$$

Figure 2.15 shows this stress strain curve.

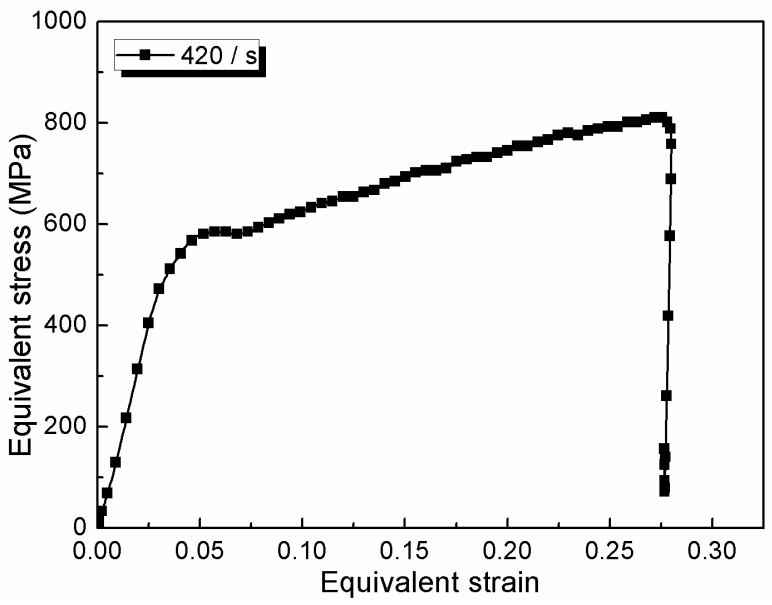


Figure 2.15 Equivalent stress and equivalent strain with strain rate of 420 / s

2.3 Nominal results of rate sensitivity SMAT treated AISI304 austenitic stainless steel sheet

Following strictly the aforementioned experimental procedure, tests are performed at 5 different loading velocities (0.001 mm/s, 2.92 m/s, 3.4 m/s, 4.82 m/s and 4.87 m/s). In order to evaluate the efficiency of the clamping device, the interrupted tests with loading-unloading cycle under small deformation have been executed under quasi-static loading. After unloading, the clamping device is amounted and photos of permanently deformed specimen are taken. Figure 2.16 depicts the nominal stress-strain curves of the interrupted tests compared with a continuous test. It appears that the repeatability of those shear tests are good and it indicates the clamping device are rather reliable.

Figure 2.17 (a-d) shows the photos of specimen after the 4 strain steps. It is found that there is almost no slip between the specimen and the clamping device when shear strain is still limited (Figure 2.17(a)-(c)). These photos reveal also (Figure 2.17(d)) the clamping efficiency is surely not acceptable when the shear strain exceed a certain limit.

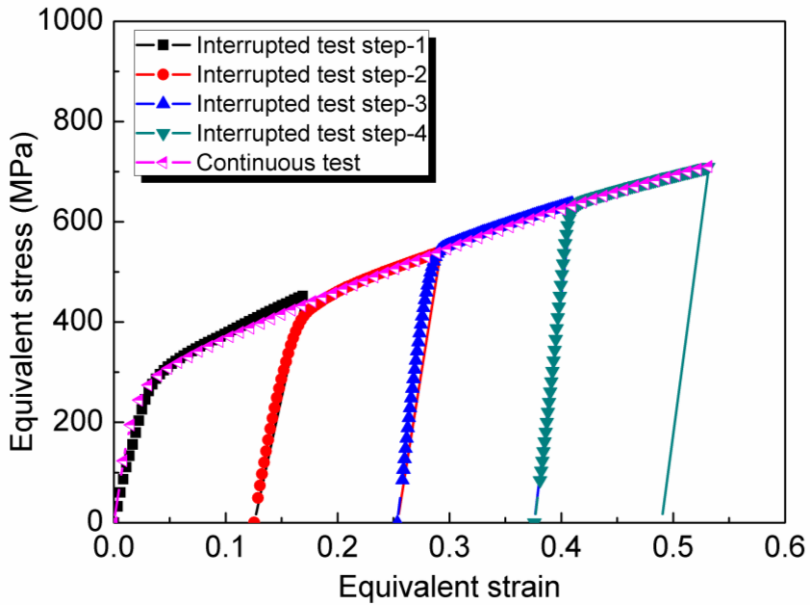


Figure 2.16 Experimental results comparison of interrupted test and continuous test under quasi-static loading

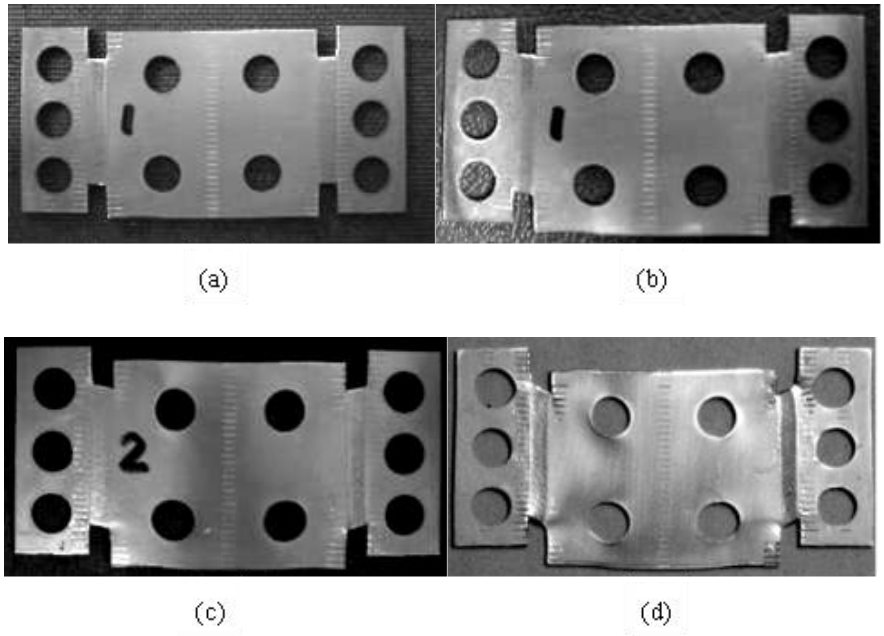


Figure 2.17 The deformation of specimen for interrupted test

The equivalent nominal shear stress and shear strain relation are also obtained from the SHPB tests, following the data processing procedure presented previously. The loading rates of 0.001 mm/s, 2.92 m/s, 3.4 m/s, 4.82 m/s and 4.87 m/s correspondent to equivalent strain rate of 0.0002/s, 420/s, 500/s, 740/s and 760/s.

Figure 2.18 presents all the equivalent nominal shear stress and shear strain relations from quasi-static tests to SHPB tests. An important rate sensitivity is found for this SMAT treated AISI304 austenitic stainless steel sheet.

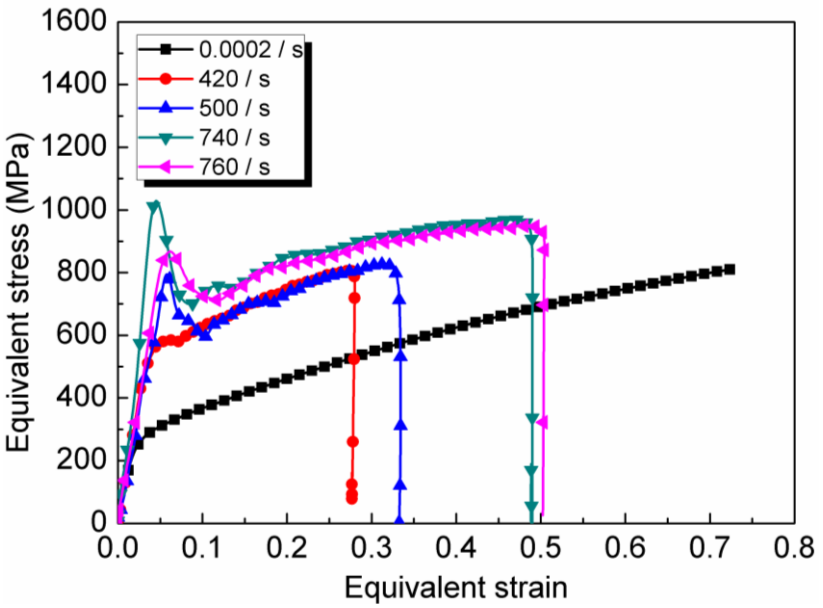


Figure 2.18 Comparison of the equivalent stress and equivalent strain under quasi-static and dynamic loading

Figure 2.19 depicts the rate sensitivity of the raw AISI304 austenitic stainless steel found in the literature [111].

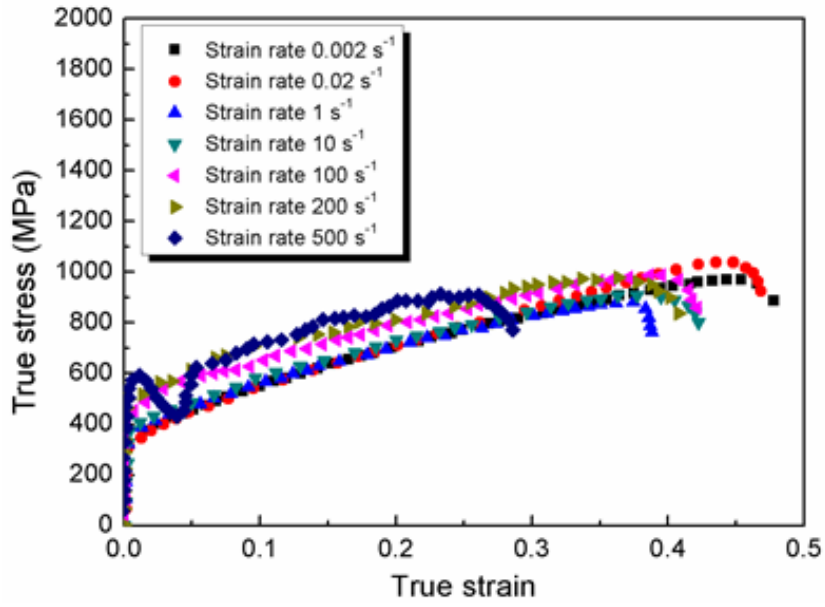


Figure 2.19 True stress-strain curves of AISI304 under different strain rates[111]

In order to compare the strain rate sensitivity of the two material states, Figure 2.20 gives a comparison of the rate sensitivities of the SMAT treated AISI304 austenitic stainless steel and the raw AISI304 austenitic stainless steel found in the literature. It is demonstrated that the SMAT treated AISI304 austenitic stainless steel is much more rate sensitive than that of raw material. It is noticed that SMAT treated AISI304 austenitic stainless steel sheet still has good ductility. The plastic strain under dynamic loading can be achieved over 50%.

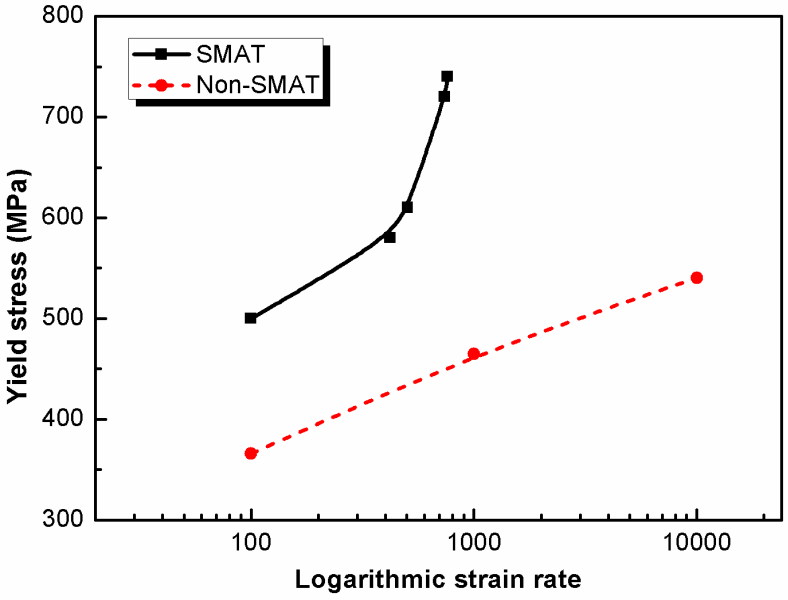


Figure 2.20 Comparison of logarithmic yield stress for different strain rates

2.4 Summary

In order to characterize the overall rate sensitivity of the SMAT treated AISI304 austenitic stainless steel sheet, the double shear tests are chosen using SHPB and a specially designed clamping devices. In this chapter, SHPB technique and the plane shear test are briefly reviewed.

Adopted testing procedures, especially for the impact SHPB test are described in detail. Double shearing tests on SMAT treated AISI304 austenitic stainless steel sheet are performed at quasi-static loading and dynamic loading rates (0.001 mm/s, 2.92 m/s, 3.4 m/s, 4.82 m/s and 4.87 m/s). Interrupted test under quasi-static loading were also made to check the clamping efficiency. Experimental results show that the overall rate sensitivity of the SMAT treated AISI304 austenitic stainless steel sheet is much higher than that of raw AISI304 austenitic stainless steel.

Chapter 3 Comprehensive analysis of impact double shear tests

3.1 Validity of stress-strain curve obtained from double shear test

In the chapter 2, the double shear testing results on the SMAT treated AISI304 austenitic stainless steel sheet led to equivalent stress-strain relation under following assumptions:

(1) For early stage of the loading (at very small strain level, say the yield stress), the equilibrium state is reached within the shear zone and an average stress strain curve do represent the constitutive relation of tested material.

(2) For the large strain level, the small strain assumption will not induce significant error.

Unfortunately, such assumptions are evidently not exact, and it is then crucial to evaluate them. For this purpose, Rusinek and klepaczko[110-112] performed a numerical analysis of the shear area to evaluate the homogeneous state level of the strain and stress field in the shear area and found that they were not as homogeneous as expected. The non-homogeneous strain field was also experimentally proven by the successive digital image correlation measurement in the studies of Merle and Zhao [108-109,113-114]. Besides, this simulation showed a significant gap between given constitutive law and the stress-strain relation obtained from simulated forces and displacements. Thus, coefficients (which is a function of the shear strain level) based on numerical simulations were proposed to fill in the gaps in stress as well as the strain. Such a concept of corrective coefficients is still used nowadays[110-113]. For instance, Guo[104] performed the dynamic shearing tests on small double shear specimens and determined corrective coefficients by experimental and numerical methods under dynamic loading. The modified formulas with coefficient factors will be shown in (3.1) and (3.2) as following:

$$\tau = \bar{\lambda}_{\tau} \frac{F}{S} \tag{3.1}$$

$$\gamma = \bar{\lambda}_{\gamma} \frac{d}{l} \tag{3.2}$$

where, $\bar{\lambda}_\tau$ and $\bar{\lambda}_\gamma$ are respectively the coefficient factors for shear stress and shear strain, F is the force loaded on the shear zone of the specimen, S is the area of specimen cross section for shear force, d and l are respectively the deformation of shear zone and length of shear zone.

Nevertheless, such a 'state-of-art' is not satisfactory for many reasons. Actually, the numerical reference is a simple shear area model. The stiffness of the clamping device is not taken into account, especially for the impact loading where the transient effect in the clamping device is not clear at all. Another possible discussion lies in the usual formulas relating forces and displacement to the shear stress and strain, especially under large strain.

In this chapter, we aims at numerical analysis of the experimental conditions of this plane shear test. First of all, the homogeneity of the shear zone is evaluated by simulation of the shear zone only. A complete numerical model (clamps+specimen) is proposed to evaluate the influence of the stiffness of the clamps in quasi-static and impact loading cases. An analysis of large strain deformation is also developed and it leads to the natural cancellation of correctives coefficient of strain.

3.2 Numerical evaluation of shear zone homogeneity

In order to evaluate the homogeneity of the shear zone, a simple numerical simulation of a rectangular shear specimen with 3 mm width and the length varying from 20 mm to 120 mm is performed. The numerical model is constructed in ABAQUS/standard code with the 8-node linear brick elements with reduced integration and hourglass control (C3D8R). The use of 3D brick element is motived by the small element size compared to the thickness of specimen. Another reason is to avoid simplified large strain treatments in some type of shell elements used in explicit version.

Figure 3.1 shows schematically the FEM model. The element size is 0.4mm$\times$ 0.375mm$\times$0.3333mm. The clamping boundary condition is applied to one edge of rectangular shear specimen, while a velocity of 0.001 mm/s was imposed on the nodes of the opposite edge.

The constitutive relation used in this simulation is extracted from double shear testing curve of SMAT treated steel[115] (Figure 3.2).

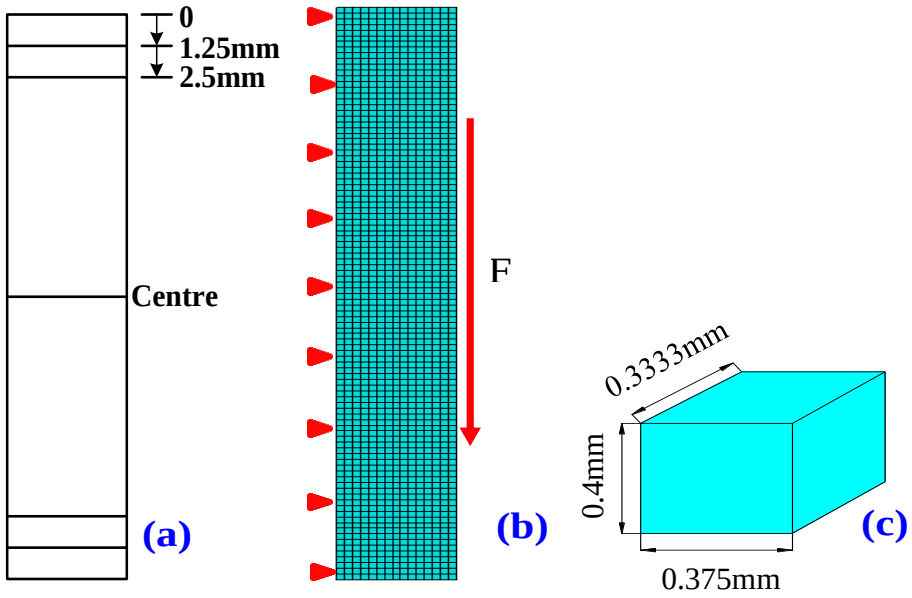


Figure 3.1 Schema, the meshes and the element sizes of the specimen for the numerical model

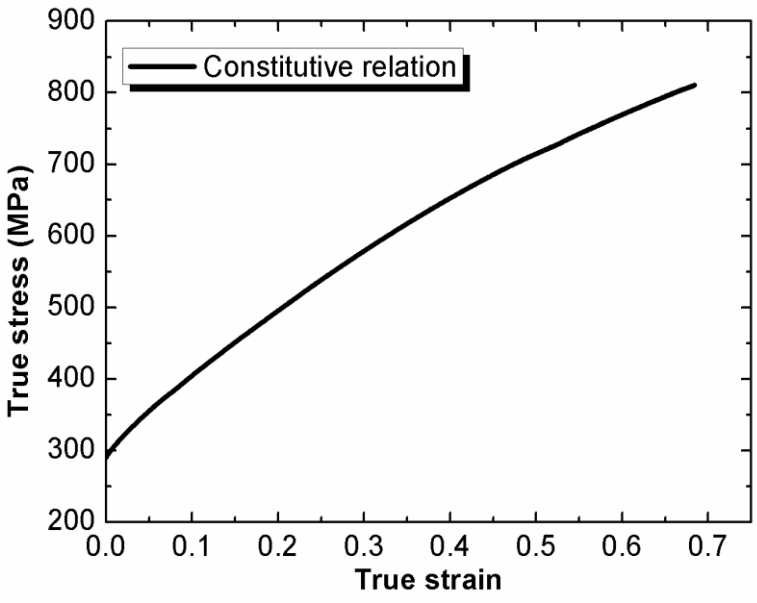


Figure 3.2 Prescribed constitutive relation

It is noted that the real testing condition is not a pure shear condition because lateral motion of the coaxial clamping devices is not possible. There are then more and more tension components when the strain increases. Figure 3.3 depicts the average value of all the elements of different components of stress and strain tensors. The tensile component is rather small but always exists.

It should be also noted that the state of strain and stress is never homogeneous because of the free boundary conditions. Figure 3.4 shows the average value of the equivalent stress and equivalent strain of all the elements in the lines at the top surface,

at a distance of 1.25mm and 2.5mm from the top free surface and at the center (see Figure 3.1(a)) in the case of a shear area length of 20mm. The state of stress and strain is clearly not homogeneous.

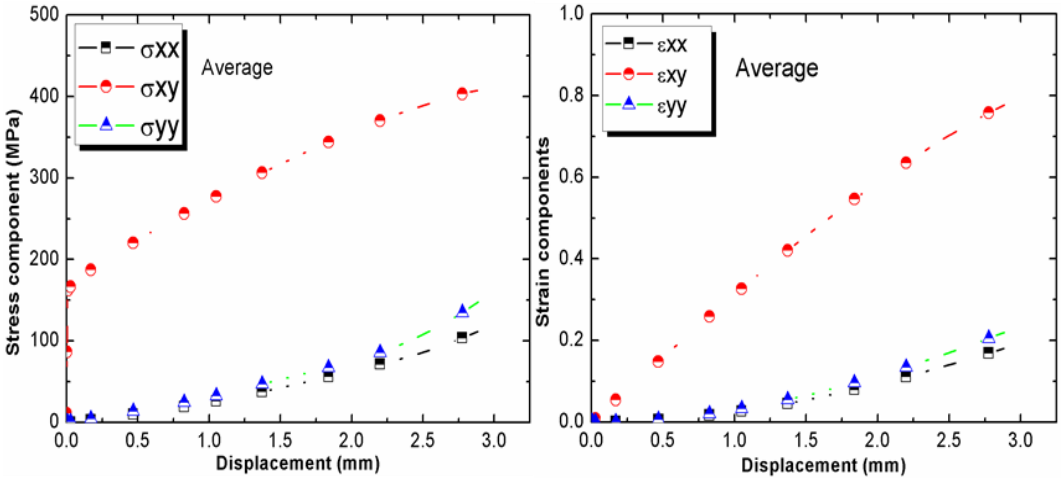


Figure 3.3 Average value of stress and strain components

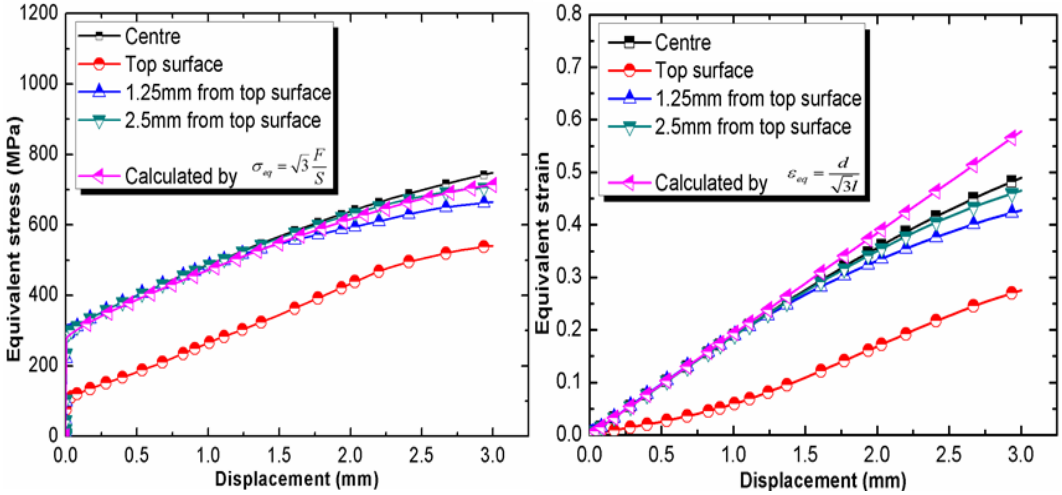


Figure 3.4 Equivalent stress and strain at different locations

Such gaps between real testing condition and idealized pure shear assumption cannot be avoided. Even though a long specimen length of 120mm (6 times) is used, the overall error will not be significantly reduced. Figure 3.5(a) provides an overall comparison between the numerically calculated force (scaled with length ratio) and the prescribed force obtained by applying the Equation(2.11) to the prescribed constitutive relation. The relative error can be defined and depicted in Figure 3.5(b), where the improvement is rather limited.

Consequently, 20mm or 30mm length are often adopted and the corrective coefficients are used to fill in the gaps. Figure 3.6 depicts respectively the numerical average equivalent stress compared with nominal stress calculated by Equation(2.11)

and the average numerical equivalent strain compared with nominal strain (Equation(2.10)).

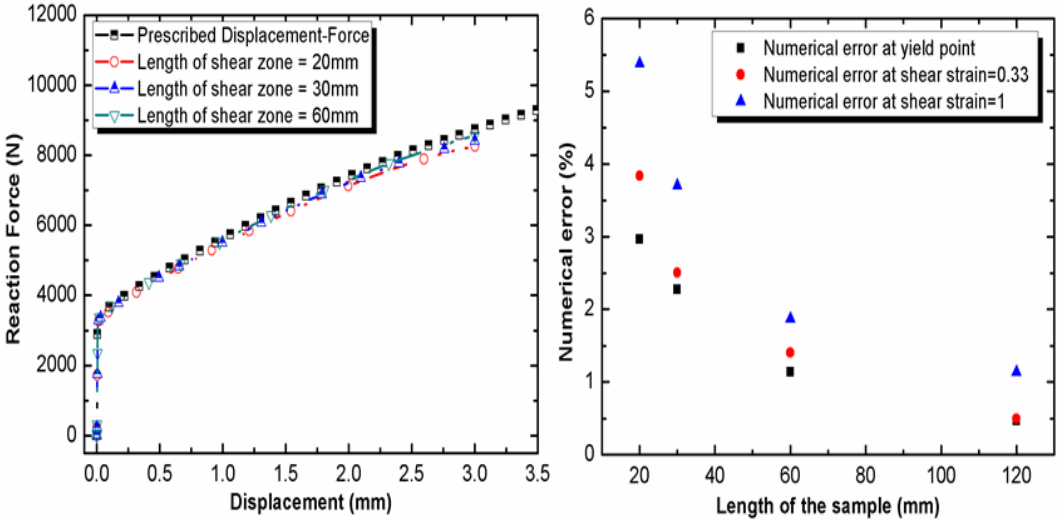


Figure 3.5 Forces and numerical errors for different lengths of shear zone

It seems that the commonly used corrective coefficient for stress is not needed if the average equivalent stress in the whole specimen is used instead of equivalent stress at the central part of the specimen (see also Figure 3.4 left). However, a multiplying coefficient applied to nominal strain seems to be necessary.

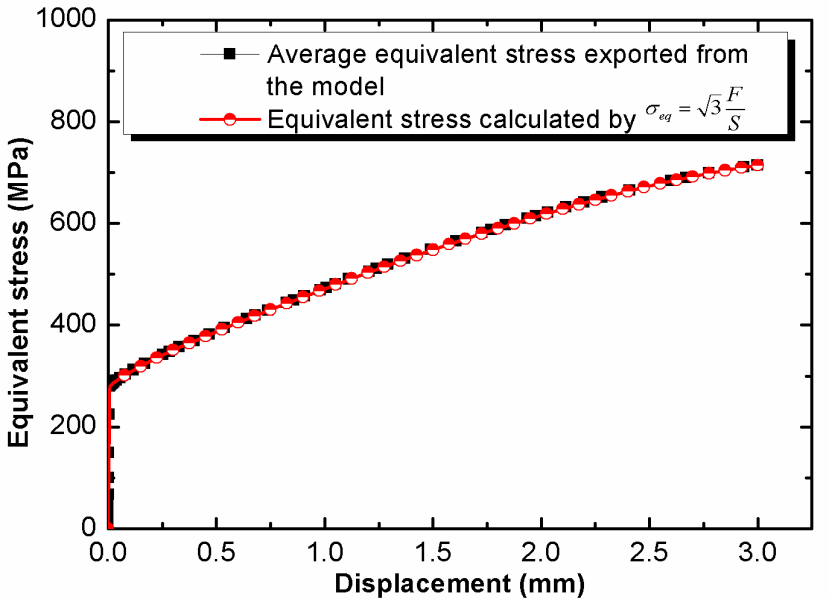


Figure 3.6 (a)

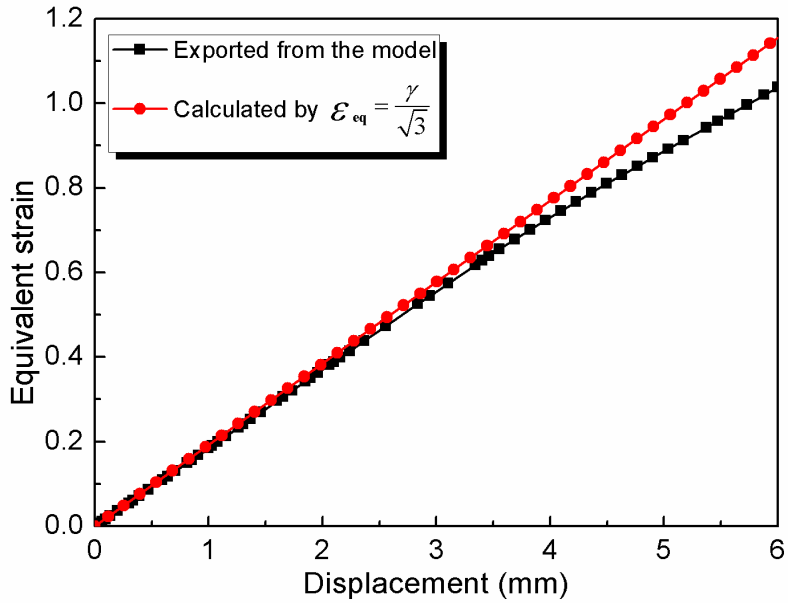


Figure 3.6 Comparison between numerical results(a) and nominal stress and strain(b)

3.3 Numerical analysis of the influence of the clamping device

From aforementioned analysis, the corrective coefficients include the eventual imprecision of the used numerical model. An evident source of numerical errors lies in the ignorance of the clamping device. A complete model including grips as well as the specimen is then built. In order to minimize the influence of the contact, the fixing bolts in all clamping pieces are not taken into account.

An overall view of the FEM model is shown in Figure 3.7.

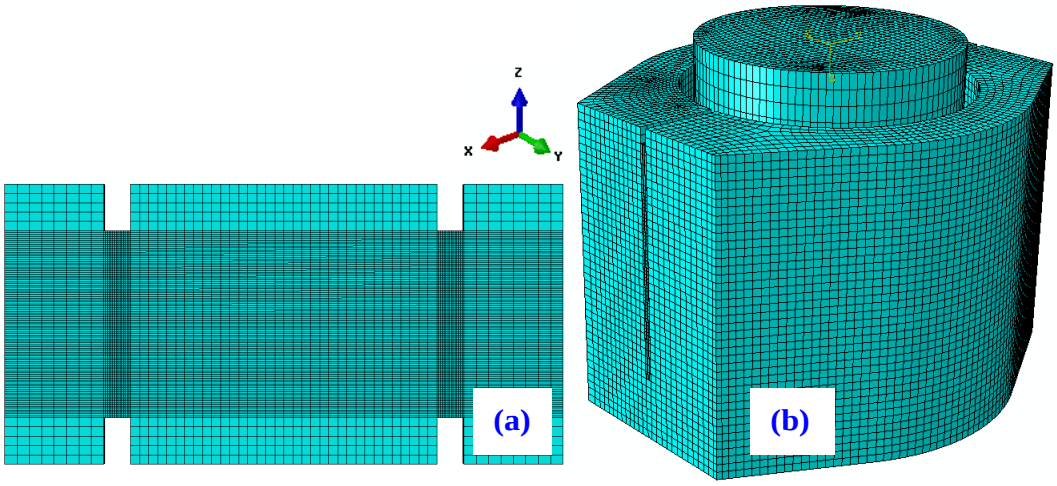


Figure 3.7 Complete numerical model

The convergence study on element size indicates that elements of 0.4 mm in the shear area are small enough to achieve the reliable results within an acceptable calculation time. The element size is same with the case of simple model.

The constitutive parameters for the two types of model are shown in table 3.1.

Table 3.1 Constitutive parameters for the model

Components	Young's Modulus E (GPa)	Density ρ (kg/m^3)	Poisson's ratio ν
Clamps	210	7800	0.3

3.3.1 Quasi-static test simulation

For the quasi-static simulation, the external clamps are fixed for all nodes situated at the bottom surface. A constant velocity of 0.001mm/s is prescribed on the top surface of the inner clamp. Surface-to-surface contact with penalty contact method is used for all the contact faces between the specimen and clamps. No slip is allowed between the two grips and the specimen.

Figure 3.8 and Figure 3.9 give the contour plots of the equivalent Von-Mises stress and the shear strain at two nominal strain levels corresponding to a displacement of 1mm and 3mm.

They can be compared with the results obtained with the simple model presented in the section 2 (superimposed in the central part of the specimen). One can see that the contour shapes and their values between those two models are nearly the same, which indicates a limited influence of the clamps. It is worthwhile to notice that the strain contour plot outside the rectangular shear zone is due to the deformation of clamping pieces because of the clamping reaction forces. It means that the clamping pieces undergo a deformation that results in a less rigid boundary condition.

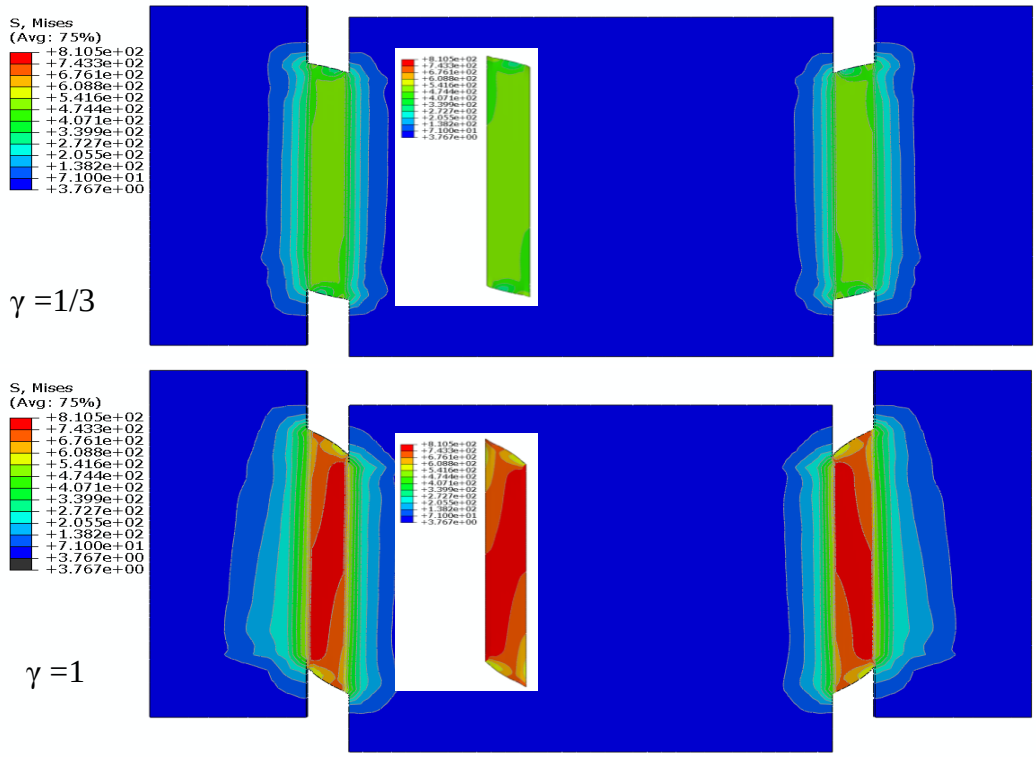


Figure 3.8 Von Mises stress comparison between the simple model and complete model

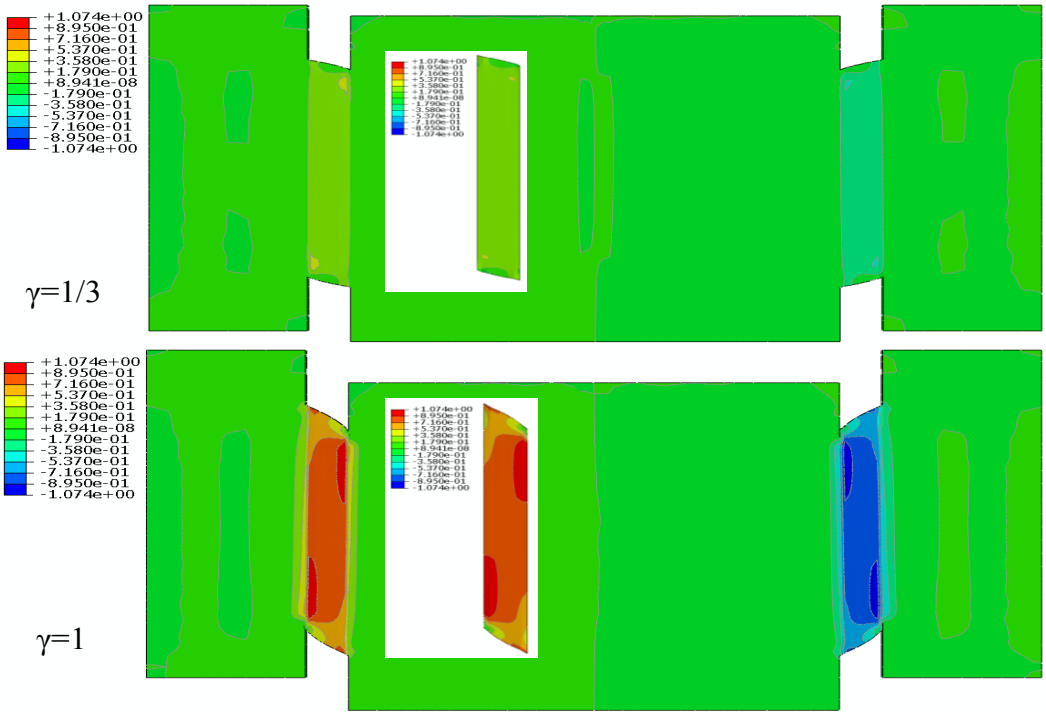


Figure 3.9 Shear strain comparison between the simple model and complete model

The detailed quantitative comparison between the simple rigid model and the complete model are also depicted in Figure 3.10.

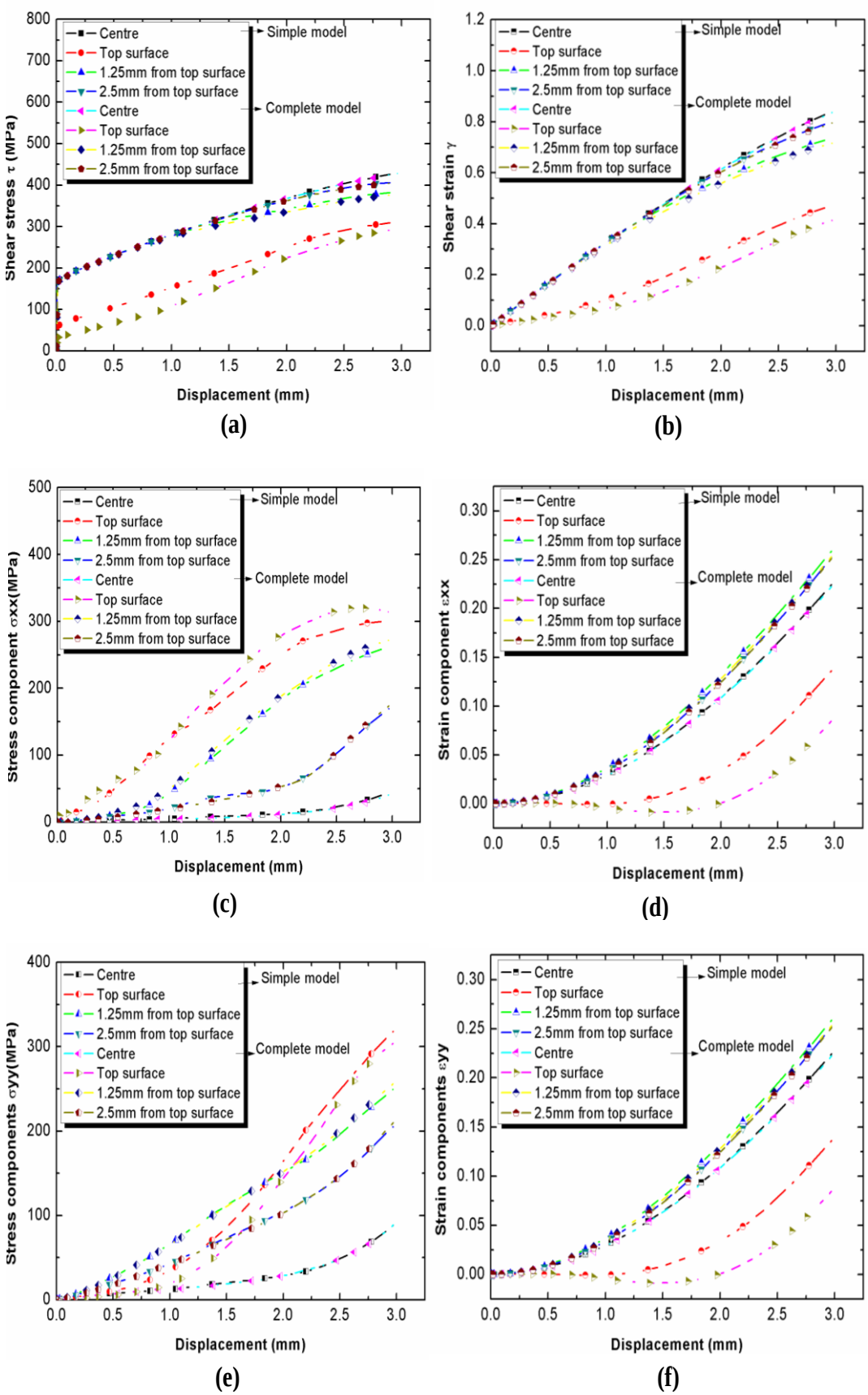


Figure 3.10 Comparison between the simple model and complete model of the stress components (a),(c),(e) and strain components (b),(d),(f) of different positions of the shear zone

At different places in the specimen, all the components seem only have negligible difference.

If we compare the numerical result with the prescribed force, the result of simple model agrees well with that of complete model. However, at rather small strain, the two models differ because of stiffness exaggeration of clamping pieces in the simple model. This leads naturally to different slopes of the elastic stage(see Figure 3.11).

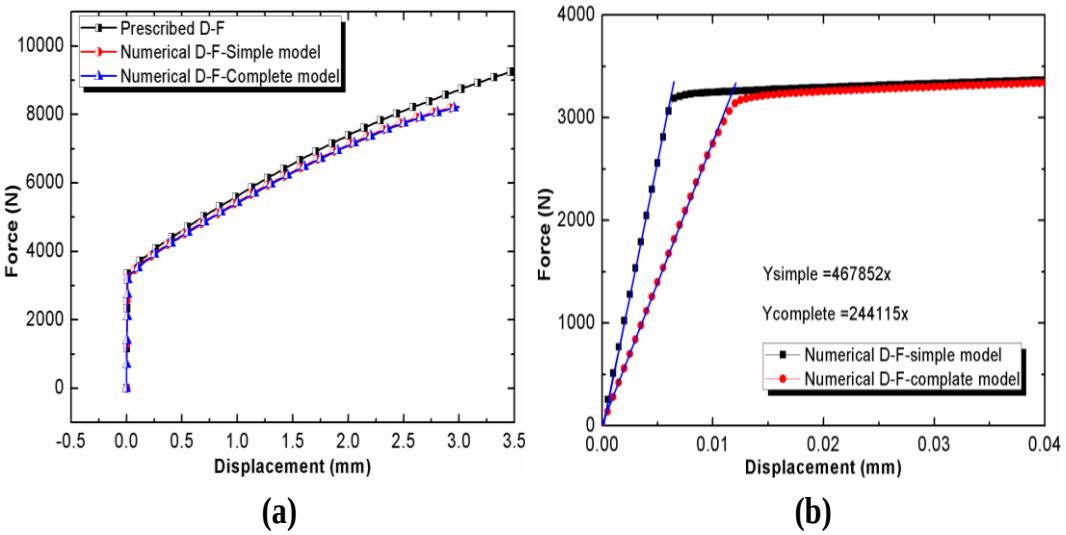


Figure 3.11 Overall comparisons between the simple model and complete model

3.3.2 Impact test simulation

Numerical analysis of the complete model under impact loading is performed with Abaqus/explicit. The material parameters (rate insensitive) and element size are the same as that of quasi-static case. Input and output velocities measured in a real SHPB test are prescribed at the two opposite ends of clamping device (see Figure 3.12). The input velocity is under 3 m/s, which is rather small for a classical SHPB. However, it leads to a shear strain rate around 1000 1/s because the gage length (width) in the shear configuration is only 3mm.

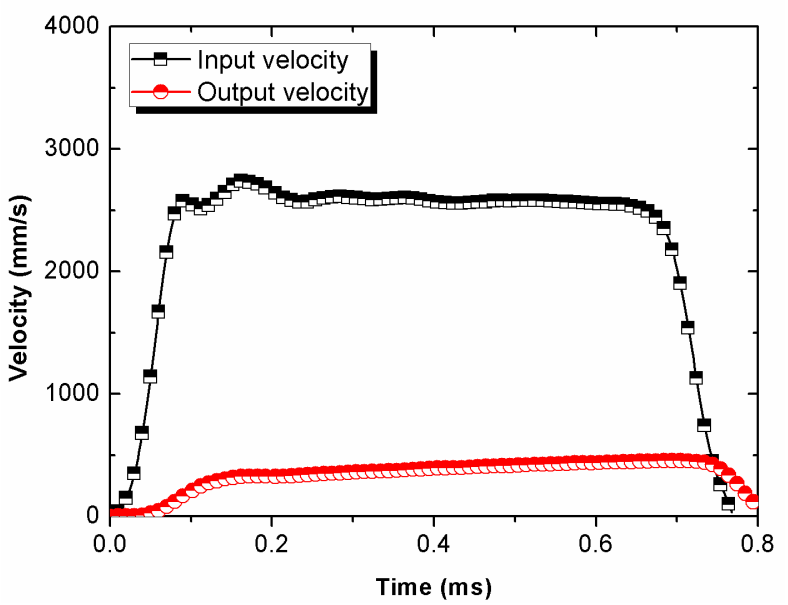
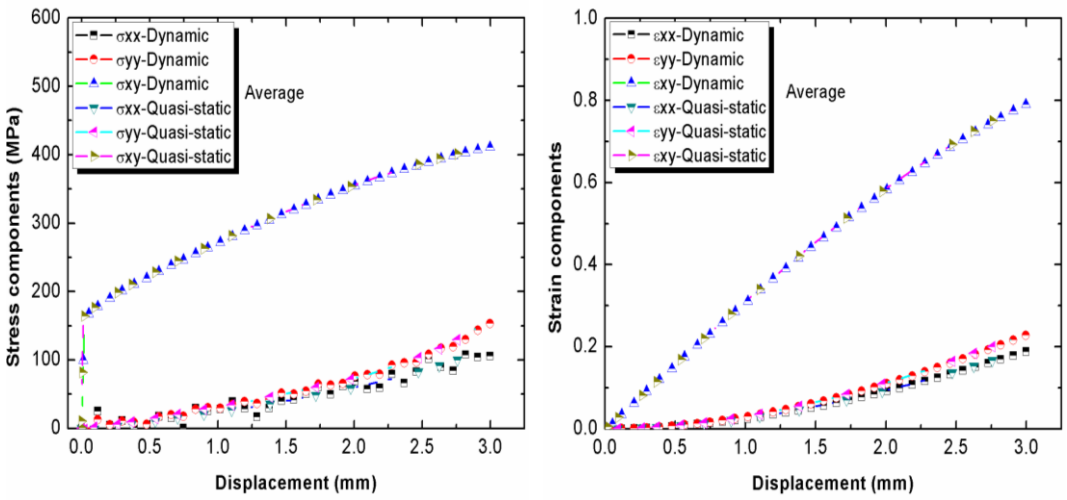


Figure 3.12 The prescribed velocities

The average value of stress components (Figure 3.13a) and strain components (Figure 3.13b) under impact is compared with these values under quasi-static loading. It indicates that the effect of clamps is very small in the shearing area. The detailed comparison at different positions of all the components in these two loading cases shows that the stress and strain distributions are nearly the same (Figure 3.14).



(a) **(b)**

Figure 3.13 Stress and strain components for quasi-static and dynamic models

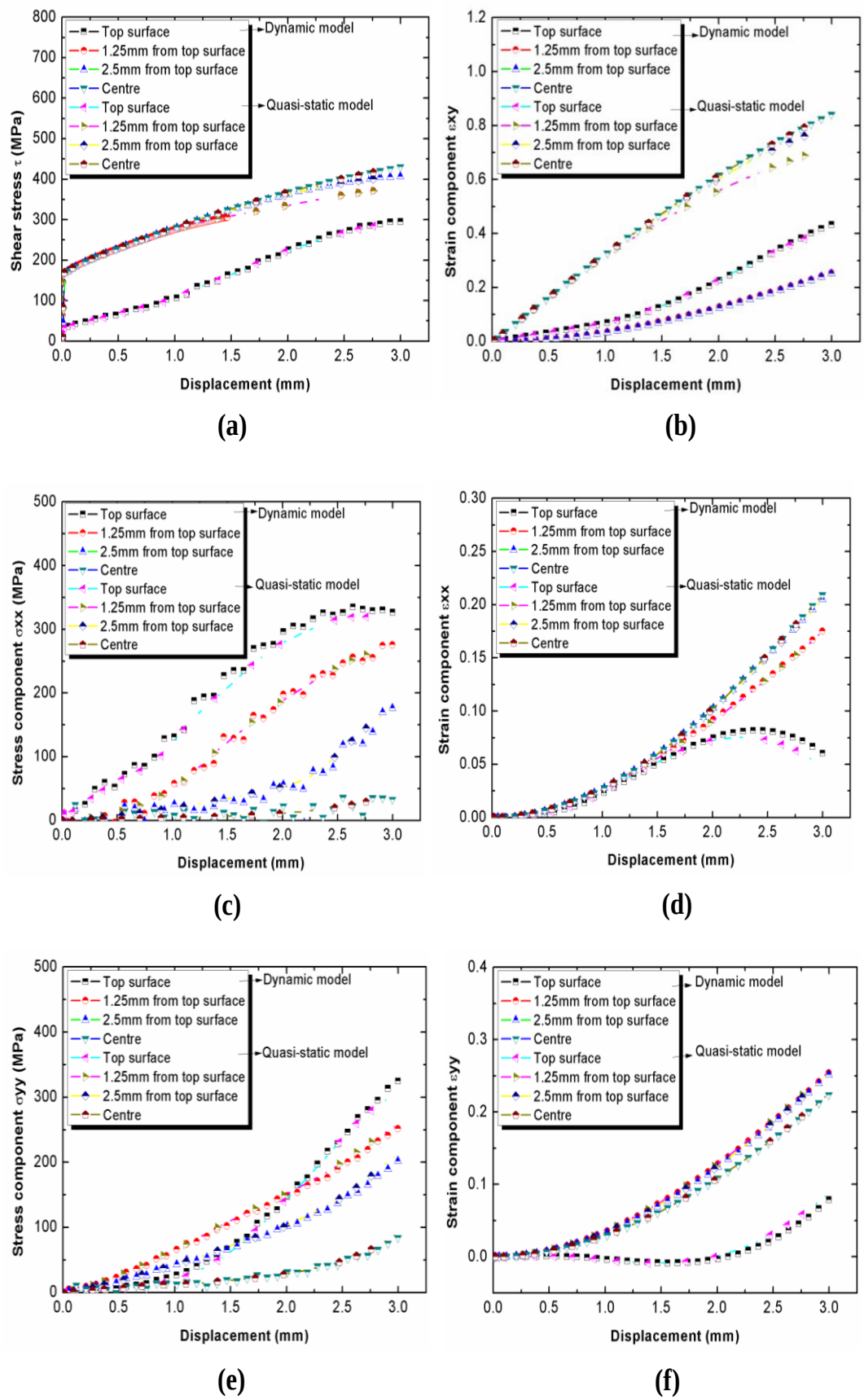
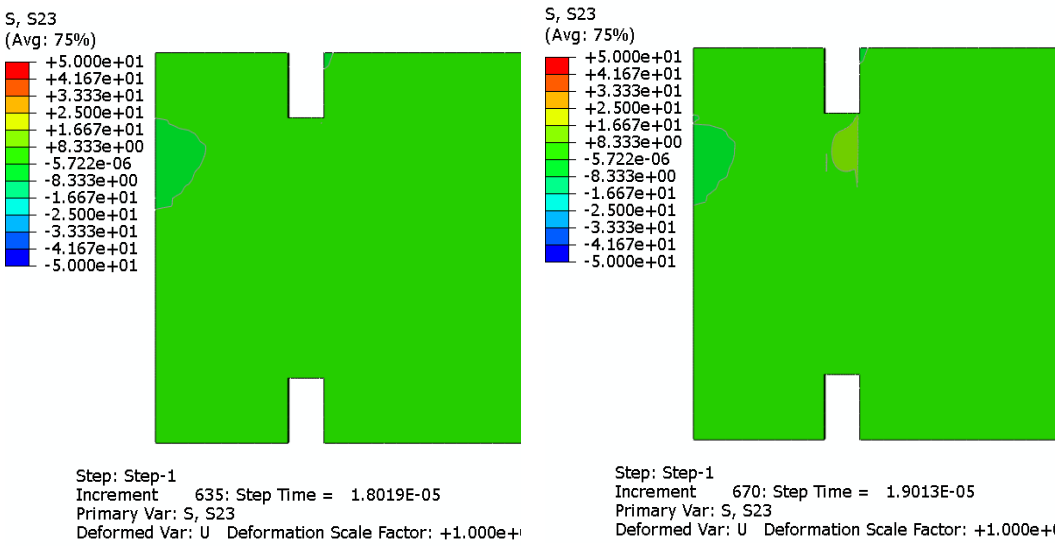


Figure 3.14 Comparison between the quasi-static model and dynamic model of the stress components (a),(c),(e) and strain components (b),(d),(f) of different positions of the shear zone

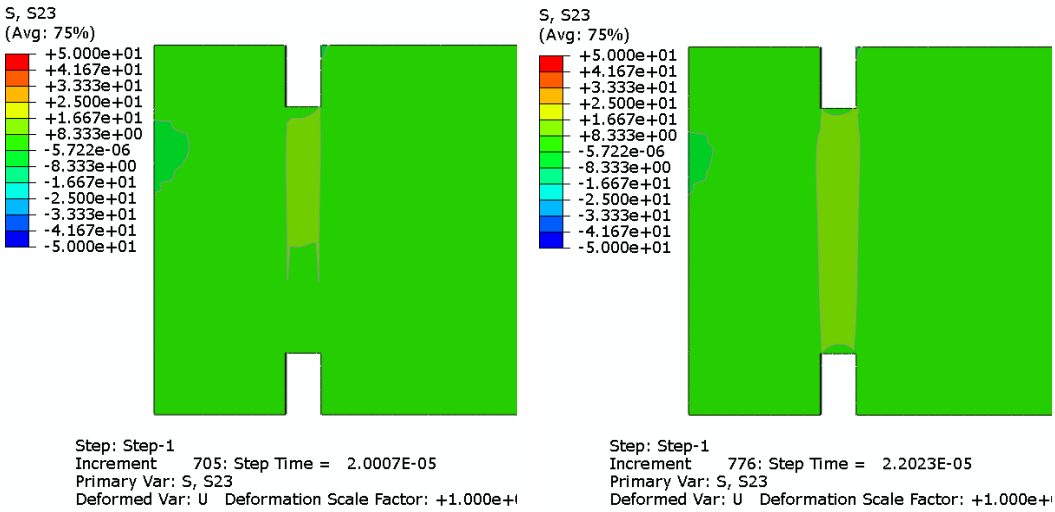
Above simulated results imply that the transient effect inside the shear area of the specimen is negligible and a somehow equilibrium state has achieved quite quickly. Figure 3.15 illustrates this process inside the specimen.

It can be seen in Figure 3.15 that at 18microseconds (a), the specimen is not yet loaded. At 19microseconds (b), the shear start from corner in contact with the inner grips propagating not only horizontally towards the external grips by the shear wave but also vertically along the inner grips because of the compressive wave within the massive inner grips. At 20microseconds (c), it is clear that the compressive wave in inner grips is dominant. At 22 microseconds (d), all the shear area is nearly homogeneous. Within 4 microseconds which is the time needed for the compressive wave to pass through the 20mm length of the shear area, the shear area is likely to be loaded homogeneously. Such processes repeat during the rising time of prescribed velocity (40microseconds, see Figure 3.12). This may explain why the stress and strain fields within shear area are hardly affected by the impact loading.

Unfortunately, such a quick equilibrium state does not mean that the transient effect in the clamping pieces is not important. Figure 3.16 illustrates the compressive wave propagating in the inner grips as an example. The wave needs more than 6 microseconds to go through the clamping pieces.

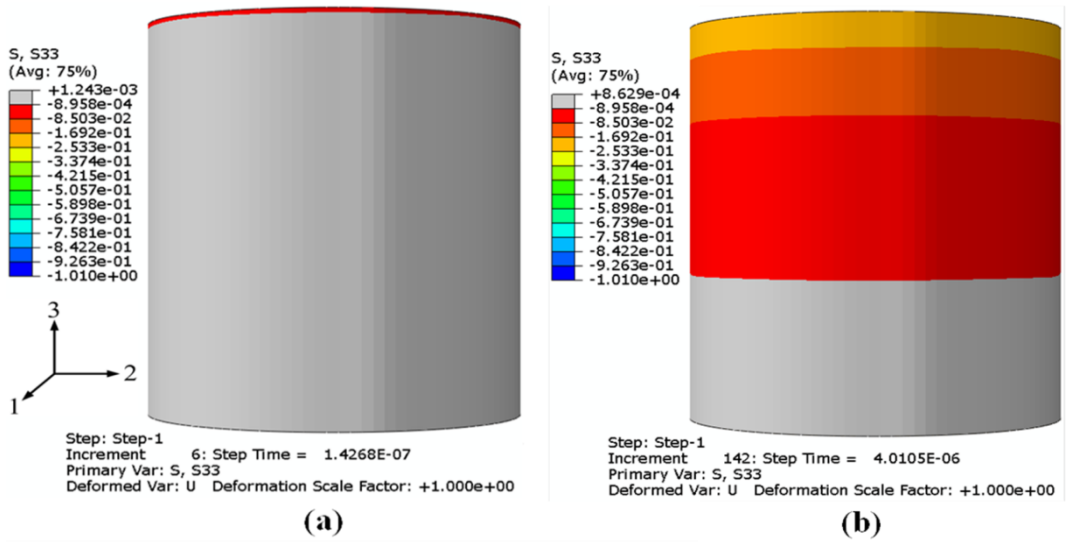


(a) **(b)**

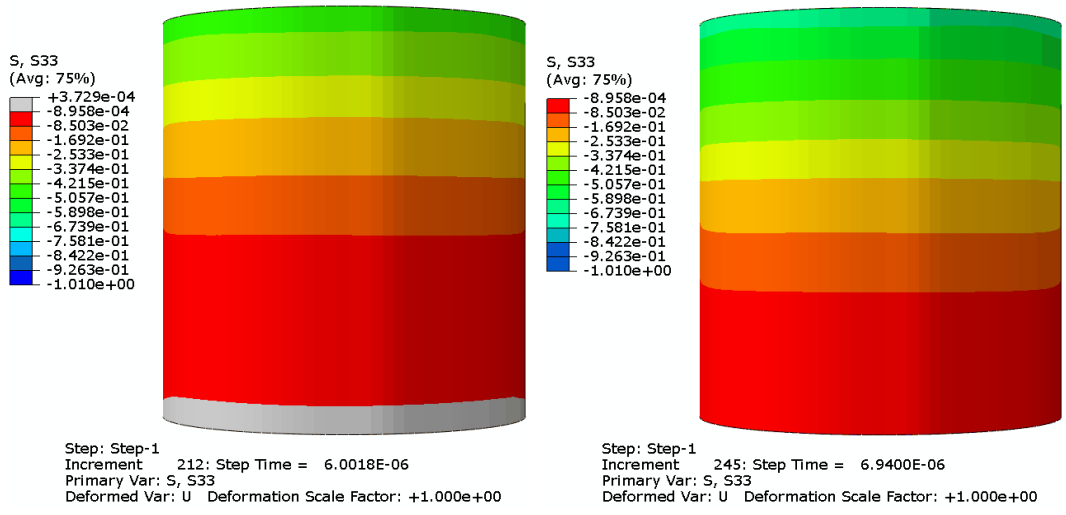


(c) **(d)**

Figure 3.15 The contour plot of shear stress on the shear zone at different moments



(a) **(b)**



(c) **(d)**

Figure 3.16 Contour plot of compression wave stress marching on the inner clamp

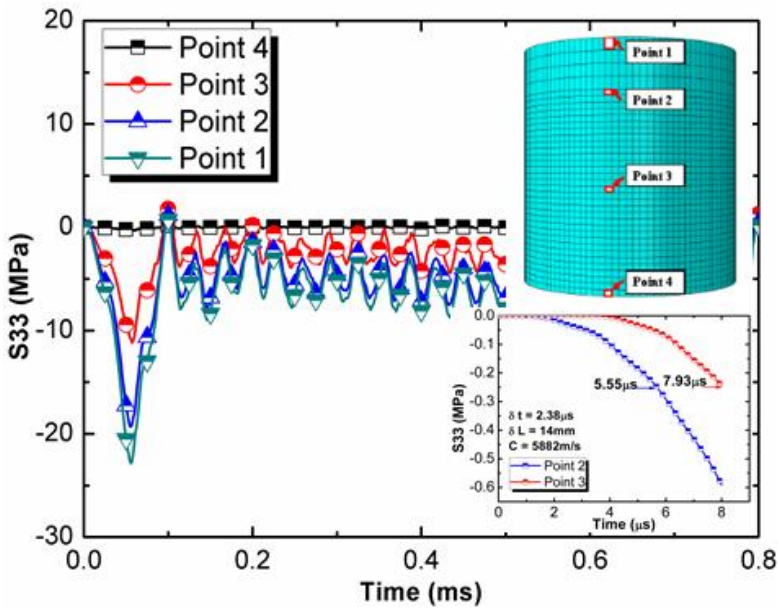


Figure 3.17 Compression wave stress on four nodes of outer surface of the inner clamp

Figure 3.17 depicts the stress time histories at different positions of the inner grips. Point 4 is the free surface so that the stress is zero. Point 1 is the place where the input force is calculated. As the other points, oscillations are found during all the testing time. There are roughly 7 periods in 200microseconds. A round trip is likely to be made in about 28 microseconds. The time delay between different points can give a more accurate evaluation of the compressive wave speed. A value of 5882m/s is found and it matches roughly the waves speed in a short cylinder (Figure 3.17). Therefore, a round trip of 28microseconds corresponds to a distance of 164mm, which is roughly the distance of a round trip inside inner and external grips (2x(40+40)mm).

In order to further prove that this oscillation is due to the wave traveling within the clamps, a simulation for the clamps with a Young's modulus 100 times high at 21000 GPa is performed. The wave speed is then 10 times quicker. Figure 3.18 shows the comparison of the two simulations as well as the prescribed force. One can see that the transient effect could dramatically affect the measured force. The input force cannot be used at all because of the wave superimposition. The output force is likely to be less affected because there is only a time shift if no impedance jumps between clamps and pressure bar. However, the early stage is more questionable. It is noted also that the important spurious oscillations is surely exaggerated in the numerical model where all the contact is hard. In the real test, such oscillation is not observed, likely to be mechanically absorbed.

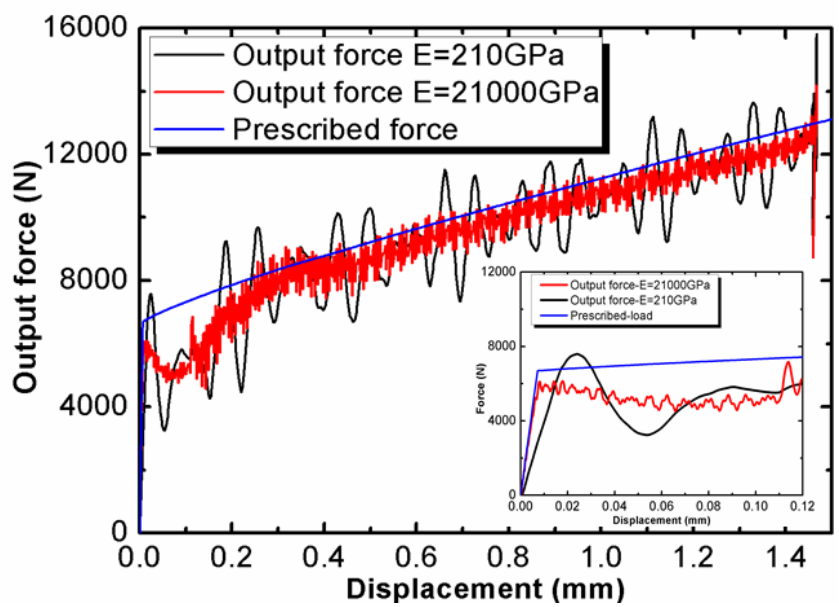


Figure 3.18 Comparison of output force with different Young's modulus defined

3.4 Large strain definition used in FEM codes and strain corrective coefficient

As mentioned in section 3.1, the corrective coefficients include not only the error of numerical model but also the error in the way that the nominal stress and strain are calculated. It is natural to ask whether the Equations (2.10 and 2.11) are the best way to calculate the nominal strain and stress, especially at high strain levels? Actually, the default strain definition in most FEM codes and in all the explicit codes (at least for 3D brick elements) is the cumulated Eulerian strain obtained by integrating the symmetric part of velocity gradient. If there is a rotation or precisely vorticity, which is the case of plane shear testing, this integration should be made in a corotational frame where the vorticity is zero to ensure the objectivity of the cumulated strain [116]. As the constitutive relation are naturally used in the FEM code, it is important to formulate and experimentally identify such a relation using the same stress and strain definition. The following theoretical analysis provides the formulas to calculate this Eulerian cumulated strain from displacement d (Figure 2.14) directly measured during testing. Besides, this analysis demonstrates also why the tension part becomes more and more important (shown in Figure 3.3).

Actually, if we take a fixed reference frame R($\vec{x}_1, \vec{x}_2, \vec{x}_3$) as shown in Figure 2.14, the velocity field in plane shear testing reads:

$$\vec{V}|_R = \begin{pmatrix} 0 \\ \dot{\gamma} x_1 \\ 0 \end{pmatrix} \tag{3.3}$$

where, $\gamma = d/l$ is engineering shear strain.

The velocity gradient can be expressed as a sum of its symmetric part, the rate of deformation$D$, and its anti-symmetric part, the vorticity Ω

$$grad\vec{V}|_R = \begin{pmatrix} 0 & 0 & 0 \\ \dot{\gamma} & 0 & 0 \\ 0 & 0 & 0 \end{pmatrix}$$

$$= \begin{pmatrix} 0 & \dot{\gamma}/2 & 0 \\ \dot{\gamma}/2 & 0 & 0 \\ 0 & 0 & 0 \end{pmatrix} + \begin{pmatrix} 0 & -\dot{\gamma}/2 & 0 \\ \dot{\gamma}/2 & 0 & 0 \\ 0 & 0 & 0 \end{pmatrix} = D_R + \Omega_R \tag{3.4}$$

The vorticity in this frame is then not zero. The cumulated Eulerian strain cannot be calculated in this frame. In order to find the needed frame without vorticity, we rotate frame R($\vec{x}_1, \vec{x}_2, \vec{x}_3$) around $\vec{x}_3$ with an angle θ(t)to define a new reference frame R′($\vec{x}_i, \vec{x}_j, \vec{x}_3$). Thus, the velocity field in this new frame can be expressed in the coordinate system ($\vec{x}_i, \vec{x}_j, \vec{x}_3$) as :

$$\vec{V}|_{R'} = \begin{pmatrix} \dot{\gamma}\frac{\sin 2\theta}{2} x_i + \left[\dot{\theta} - \frac{\dot{\gamma}}{2}(1 - \cos 2\theta)\right] x_j \\ \left[-\dot{\theta} + \frac{\dot{\gamma}}{2}(1 + \cos 2\theta)\right] x_i - \dot{\gamma}\frac{\sin 2\theta}{2} x_j \\ 0 \end{pmatrix} \tag{3.5}$$

The rate of deformation D and vorticity Ω in this rotating frame is calculated by

$$D|_{R'} = \begin{bmatrix} \dot{\gamma}\frac{\sin 2\theta}{2} & -\dot{\gamma}\frac{\cos 2\theta}{2} \\ -\dot{\gamma}\frac{\cos 2\theta}{2} & -\dot{\gamma}\frac{\sin 2\theta}{2} \end{bmatrix} \quad \Omega|_{R'} = \begin{bmatrix} 0 & \dot{\theta} - \frac{\dot{\gamma}}{2} \\ \frac{\dot{\gamma}}{2} - \dot{\theta} & 0 \end{bmatrix} \tag{3.6}$$

As we aim at finding a reference frame where the vorticity should be zero, this angle θ(t) should satisfy

$$\theta = \theta_0 + \frac{\gamma}{2}$$

Thus, the rate of deformation and vorticity are calculated in this specific reference frame R^S.

$$D|_{R^s} = \begin{bmatrix} \dot{\gamma}\frac{\sin(2\theta_0+\gamma)}{2} & \dot{\gamma}\frac{\cos(2\theta_0+\gamma)}{2} \\ \dot{\gamma}\frac{\cos(2\theta_0+\gamma)}{2} & -\dot{\gamma}\frac{\sin(2\theta_0+\gamma)}{2} \end{bmatrix} \quad \Omega|_{R^s} = 0 \tag{3.7}$$

By integrating $D|_{R^s}$ with time t, the strain tensors in R^S can be found:

$$E^s|_{R^s} = \begin{bmatrix} \sin\frac{\gamma}{2}\sin\left(2\theta_0+\frac{\gamma}{2}\right) & \sin\frac{\gamma}{2}\cos\left(2\theta_0+\frac{\gamma}{2}\right) \\ \sin\frac{\gamma}{2}\cos\left(2\theta_0+\frac{\gamma}{2}\right) & -\sin\frac{\gamma}{2}\sin\left(2\theta_0+\frac{\gamma}{2}\right) \end{bmatrix} \tag{3.8}$$

The projection of strain tensor to the coordinate system $(\vec{x}_1, \vec{x}_2, \vec{x}_3)$ it leads to

$$E^s|_R = \begin{bmatrix} -\frac{1}{2}(1-\cos\gamma) & \frac{1}{2}\sin\gamma \\ \frac{1}{2}\sin\gamma & \frac{1}{2}(1-\cos\gamma) \end{bmatrix} \tag{3.9}$$

Thus, for the simple plane shear test, the von-Mises equivalent strain for this Eulerian cumulated strain tensor will be the following:

$$\varepsilon_{eq} = \sqrt{\frac{2}{3}(1-\cos\gamma)} \tag{3.10}$$

Figure 3.19 shows the comparison of the nominal equivalent strain calculated by (Equation 3.10) with the numerical average equivalent strain. There is nearly no gap and this implies that the main gap is actually due to a misunderstanding of the strain definition in the FEM codes in the large strain configuration. It implies that the non-homogeneous state of strain is not the main factor of the gaps found in previous works.

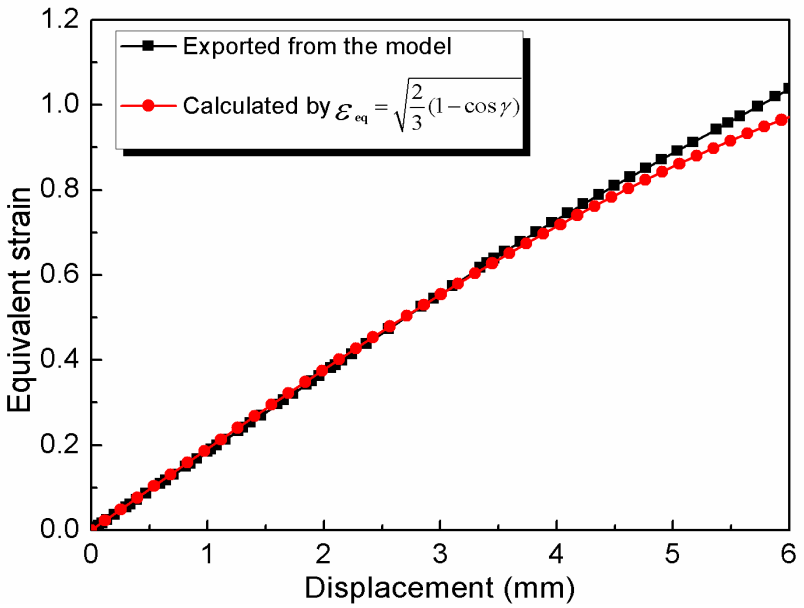


Figure 3.19 Numerical results compared with nominal strain

Finally, if the Euleiran cumulated strain is used to calculate nominal strain from experimental displacement data and the average equivalent stress in all the shear area is used, the corrective coefficients are no longer needed. Figure 3.20 depicts the comparison between the prescribed force/displacement relation (which is used to

calculate stress-strain relation for numerical models) and the calculated force/displacement curve from the numerical model and they agree very well.

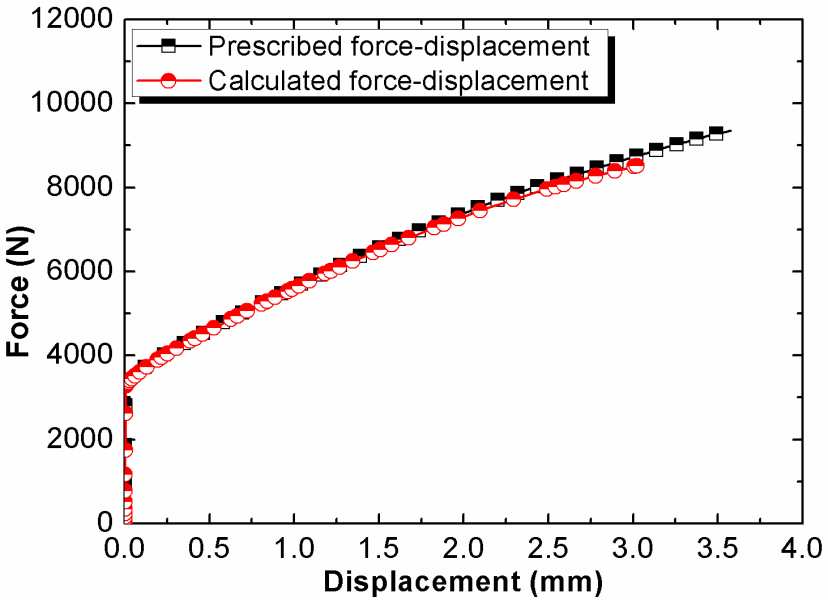


Figure 3.20 Comparison of modified numerical result and experiment result

3.5 Application to SMAT treated AISI304 austenitic stainless steel sheet

Above complete analysis of shear testing conditions shows that even there is no a homogeneous shear zone, the average equivalent shear stress-shear strain relation reflect well the test material behavior and the clamping device have very limited influence on this result. However, the Eulerian cumulated strain should be used for large strain.

The rate sensitivity obtained in Chapter 2 for the SMAT treated AISI304 austenitic stainless steel sheet does not take into account of the analyses developed in section 3.4. Therefore, these results should be recalculated using Eulerian cumulated equivalent strain.

Figure 3.21 shows all the equivalent nominal stress and Eulerian cumulated equivalent strain which calculated by Equation (3.10) relations from quasi-static and SHPB tests.

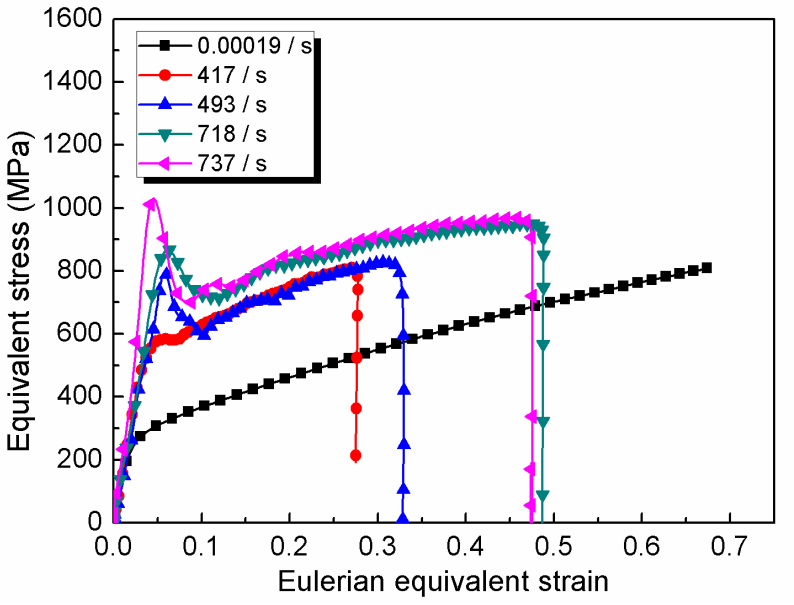


Figure 3.21 Comparison of the equivalent stress and equivalent strain under quasi-static and dynamic loading

3.6 Summary

The double shear tests for sheet metals are investigated numerically and analytically in this paper in order to understand and improve actual data extracting method. The main points are the following:

i) The clamping device has been added in the numerical model devoted to find commonly used corrective coefficients to extract stress-strain relation in such test. Under quasi-static loading, Taking account of the clamps leads to a less rigid boundary condition on the shear area. It leads to an additional error on the early stage of the test (elastic part).

ii) Under impact loading, the shear loading in the shear area is mainly guided by the compressive wave within the massive clamping pieces. The equilibrium within the shear area is quickly attained. However, the transient effect due to wave propagating between the clamping pieces leads to important oscillations.

iii) The cumulated Eulerian strain should be used to calculate the nominal strain in such test. With this cumulated Eulerian strain and Cauchy stress derived from experimental displacement/force recording, it is possible to repeat numerically the test. It implies that all the corrective coefficients commonly used for this test are no longer needed.

Chapter 4 Parameter Identification of a multi-layers elastic-plastic damageable model for SMAT treated AISI304 austenitic stainless steel sheet

4.1 Multi-layers geometry and the elastic plastic parameters of each layer.

As mentioned at the beginning, the final aims of this Ph.D research is to better understand the quasi-static and impact behavior of SMAT treated AISI304 austenitic stainless steel sheet and to build a reliable constitutive model. With this constitutive model, the response of structures made of SMAT treated AISI304 austenitic stainless steel sheet can be predicted. Furthermore, prospective studies on the influence of the properties gradient can be performed and gradient adaptive designs become possible.

For this purpose, we aimed at building a multi-layers elastic-plastic damageable model for SMAT treated AISI304 austenitic stainless steel sheet behavior in this chapter. Thus, the starting point is the tensile testing results on SMAT treated AISI304 austenitic stainless steel sheet after removing different depth of treated surface, already described in the introduction.

Actually, it is not easy to obtain the constitutive law of each layer of SMAT treated sheet metals because of the difficulties of separating each layer from the whole structures. Such a process via removing different layers step by step and tensile experiments of the specimen after outer surface removal is the only available procedure to get quantitative information of the layers geometry and its mechanical properties[117-118].

Figure 4.1 recalls the typical true stress strain curves of various tensile tests, where the four following types of specimen are used:

(1) 1mm thick AISI304 austenitic stainless steel as received;

(2) 1mm thick AISI304 austenitic stainless steel with SMAT at both sides;

(3) 0.7mm thick AISI304 austenitic stainless steel with SMAT at both sides and removed the upper and lower surface of 0.15mm each.

(4) 0.5mm thick AISI304 austenitic stainless steel with SMAT at both sides and removed the upper and lower surface of 0.25mm each.

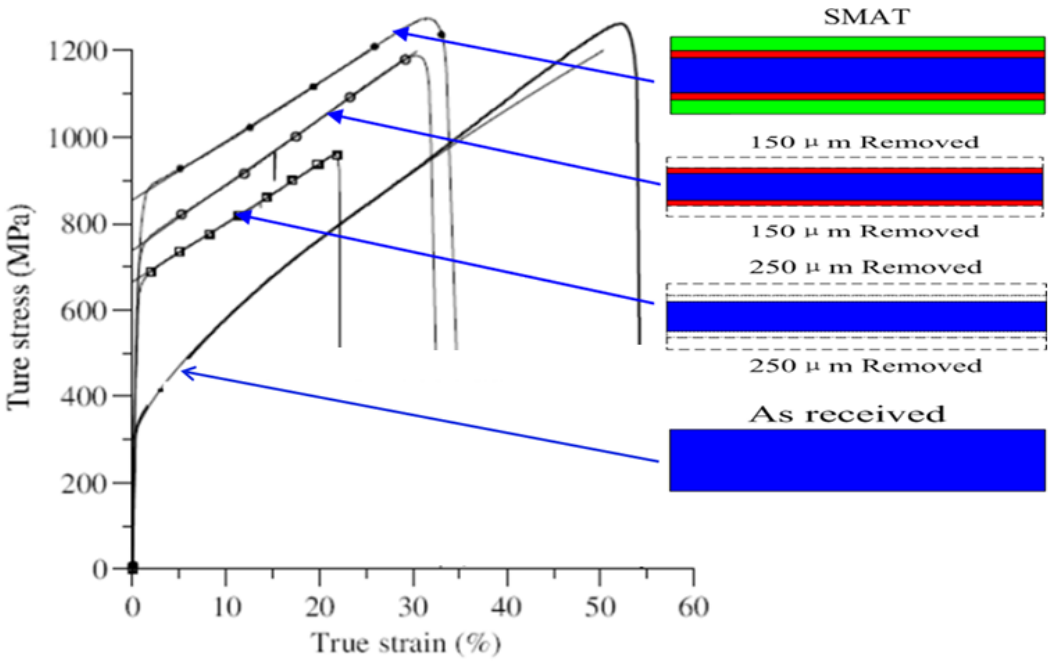


Figure 4.1 True stress-strain curves of the treated and as-received AISI304 stainless steel of 1mm thickness and different testing states of specimens

It is obvious that the geometry of layers in the prospective model should correspond to the removal thickness. Therefore, we propose a model with five layers: a core layer of 0.5mm in the center, two adjacent transition layers of 0.1mm and two external top hard layers of 0.15mm.

From figure 4.1, it is easy to make a curve fitting to the simple elastic-plastic Ludwig model as given in equation (4.1)

$$\sigma = A + B\varepsilon_p^n \tag{4.1}$$

The curve fitting provides parameters expressed as follows,

$$\sigma_{as} = 300(1 + 4.9\varepsilon_p^{0.72}) \tag{4.2}$$

$$\sigma_{treated} = 854(1 + 1.6\varepsilon_p) \tag{4.3}$$

$$\sigma_{0.7} = 739(1 + 2.05\varepsilon_p) \tag{4.4}$$

$$\sigma_{0.5} = 665(1 + 2.05\varepsilon_p) \tag{4.5}$$

From these parameters, if we suppose the behavior of each layers has the same type of expression, the elastic-plastic relations of each layer can be derived

individually. Actually, the core layer behavior is already known from Equation 4.5, the transition layer behavior can be easily determined from Equation 4.4 and finally that of the top hard layer from Equation 4.3. The parameters of each layer are given in Table 4.1

Table 4.1 Elastic-plastic parameters of different graded layers

Components	Top layer	Transition layer	Core layer
A	1122.3	924	665
B	1021.3	1894.2	1363.3

Figure 4.2(a) depicts an illustration of the yield point of each layer whereas the hardening behavior is plotted in Figure 4.2 (b).

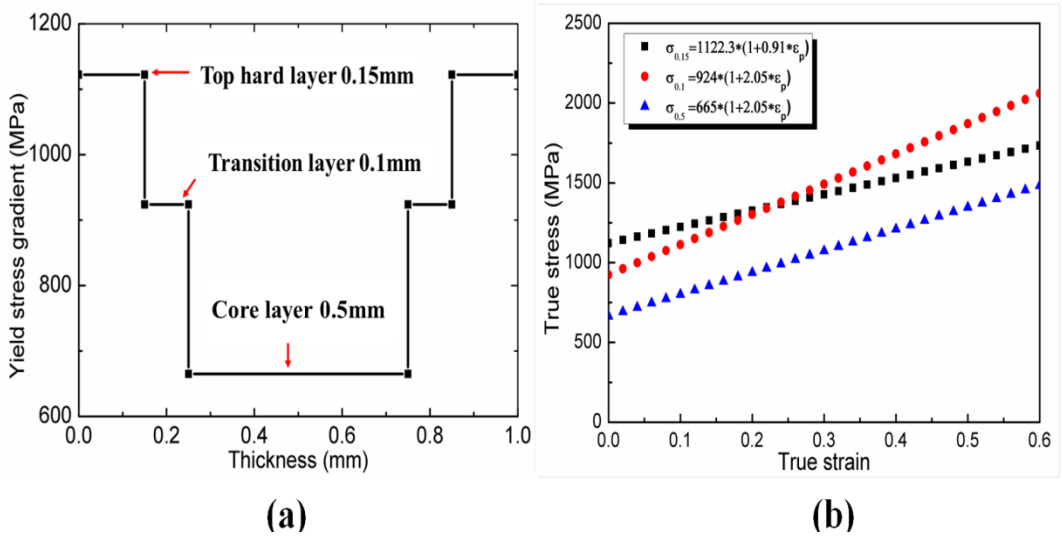


Figure 4.2 Yield stresses (a) and hardening (b) of layers

4.2 Determining the damage evolution and fracture strain of each layer

4.2.1 Inverse identification by numerical simulation

Elastic plastic parameters of each layers is easily found because each layer is considered as homogeneous at this stage of strain. However, the fracture feature is a localized parameter, the apparent fracture strain in Figure 4.1 do not offer an evident assessment of fracture parameters in each layer. An inverse identification using

numerical simulation is unavoidable.

ABAQUS/Explicit was used for establishing models to simulate the tensile tests. Actually, material failure and element degradation often leads to severe convergence difficulties in ABAQUS/implicit, while such problems do not exist in explicit analysis.

The tensile dog-bone specimen model is shown in Figure 4.3. The constitutive parameters are listed in Table 4.1.

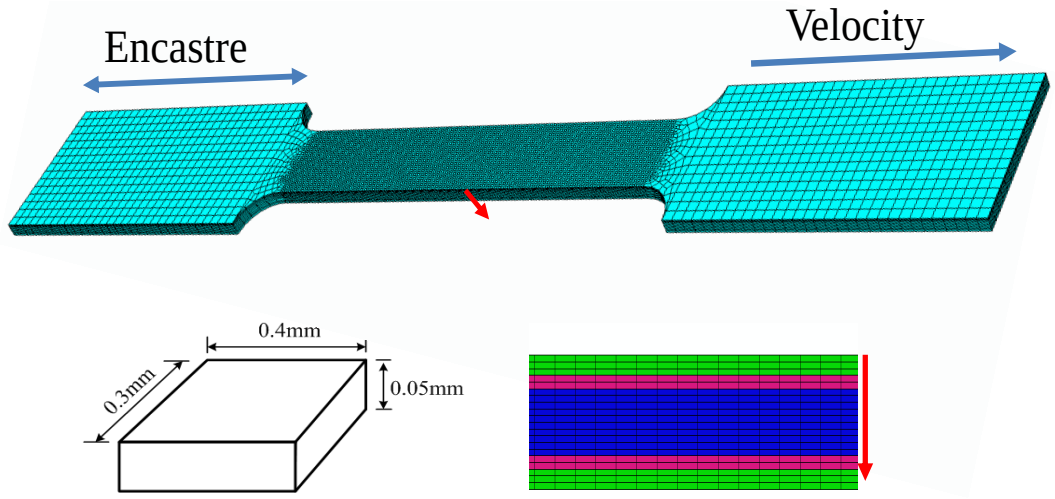


Figure 4.3 The model for tensile simulation and meshes

Eight-node reduced integration 3D brick elements were used to generate the model. In order to achieve the boundary condition consistent with the real tensile tests (see Figure 4.5), the left part of the model is fixed as the clamping boundary condition and a velocity of 0.5mm/s corresponding with equivalent strain rate of 10^{-2} s^{-1} loaded in axial direction on the right part. It was divided in five graded layers in the thickness direction. The thickness of the upper surface layer, the adjacent transition layers and the core layer are 0.15mm, 0.1mm and 0.5mm respectively. It is easy to construct then the numerical models for 0.7mm specimen as well as the 0.5mm core only model.

We chose to use ABAQUS/Explicit because of its computationally efficiency for the problem involving the damage evolution till fracture. However, ABAQUS/Explicit is conditionally stable, and the stability limit is estimated by follow:

$$\Delta t = \frac{L^e}{c_d} \tag{4.6}$$

$$c_d = \sqrt{\frac{E}{\rho}} \tag{4.7}$$

where, L^e is the smallest element dimension in the mesh, c_d is the wave speed. Δt is usually a small value which makes ABAQUS/Explicit only suitable for high speed impact problems, ρ is the density.

For our quasi-static simulation, ABAQUS/Explicit provides an automatic mass scaling technique, which can be used to increase the time increment to an acceptable value by enlarging material density. From the two equations above, if artificially increasing the material density ρ as f^2 times, then the velocity will be reduced f times, which could enhance the stable increment step as f times. The quasi-static loading conditions are guaranteed by ensuring a small ratio the kinetic energy/the strain energy with the chosen time increment.

The time increment in this work is enlarged to be 100μs. The ratio the kinetic energy/strain energy is around 10^{-4} with this chosen time increment (see Figure 4.4).

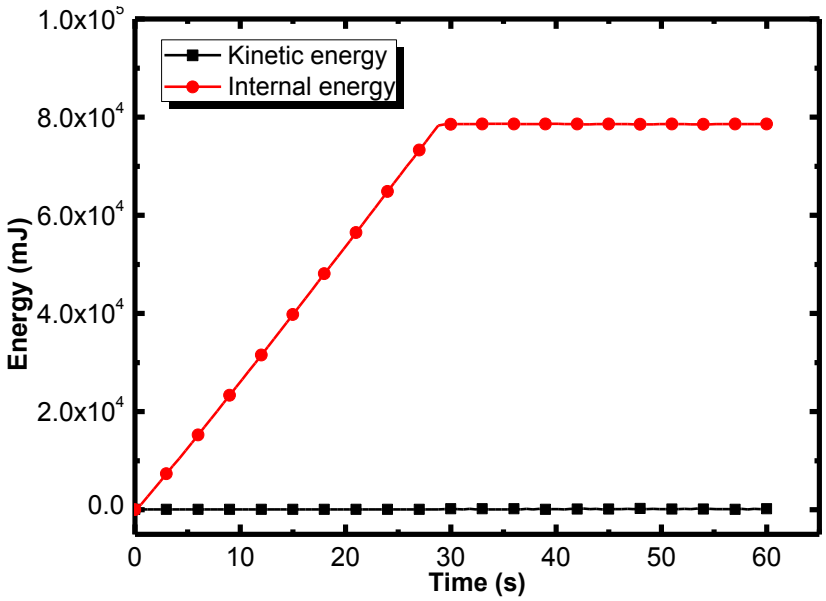


Figure 4.4 Comparison of kinetic energy and internal energy using mass scaling

4.2.2 Selected damage model

The isotropic ductile damage model available in ABAQUS/explicit is chosen. It is assumed that the degradation of the stiffness associated with each active failure mechanism can be modeled using a scalar damage variable D, capturing the combined effect of all active mechanisms. At any given time during the analysis the stress tensor in the material is given by the scalar damage equation,

$$\sigma_{ij} = (1 - D)\sigma_{ij}^0 \quad (i = 1,2,3;\ j = 3) \tag{4.8}$$

where, D is the overall damage variable and σ_{ij}^{0} is the effective (or undamaged) stress tensor computed in the current increment. D can monotonously change from 0 to 1.

An important thing is to define the criterion for damage initiation. It is the point when the damage mechanism will start. Equation (4.9) expresses this condition.

$$\omega_D = \int \frac{d\bar{\varepsilon}^{pl}}{\bar{\varepsilon}_D^{pl}(\eta,\dot{\bar{\varepsilon}}^{pl})} = 1 \tag{4.9}$$

where, $\eta = -p/q$ is stress triaxiality, p is hydrostatic pressure, q is Von Mises equivalent stress, $\dot{\bar{\varepsilon}}^{pl}$ is equivalent plastic strain rate, ω_D is a state value, monotonically increasing with plastic deformation. In practice, this criterion can be simply characterized by a coefficient called the strain at fraction $\varepsilon_{fracture}$ in ABAQUS/Explicit.

After this starting point, the damage will vary following a damage evolution law to be defined. ABAQUS propose an exponential damage evolution law (Equation 4.10).

$$D = \frac{1-e^{-\alpha(\bar{u}^{pl}/\bar{u}_f^{pl})}}{1-e^{-\alpha}} \tag{4.10}$$

In practice, this evolution is determined by two parameters: the relative plastic displacement at failure $\bar{u}_f^{pl}$ and the exponent α.

Therefore, the entire numerical processing can be shown by Figure 4.5, which illustrates the characteristic stress-strain behavior of a material undergoing damage.

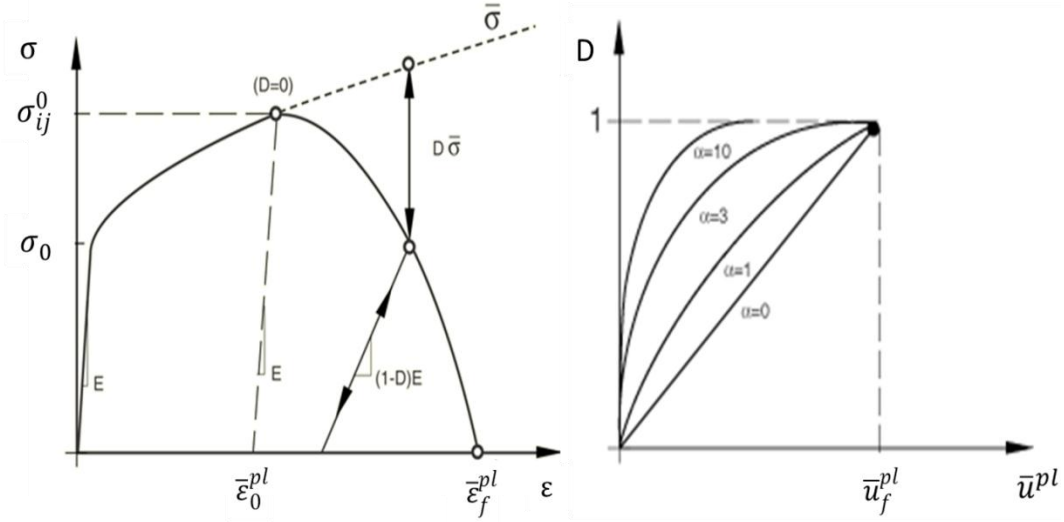


Figure 4.5 Stress-strain curve with progressive damage degradation(a) and Exponential form for damage evolution(b)

In the context of an elastic-plastic material with isotropic hardening, the damage manifests itself in two forms: softening of the yield stress and degradation of the elasticity. The solid curve in the figure represents the damaged stress-strain response, while the dashed curve is the response in the absence of damage. When the criterion (Equation 4.10) is satisfied, D = 0 and the damage starts, then with the increase of loading, the damage evolution go along the path defined (figure 4.5(b)). When D = 1, the overall damage happened. By default, the element is removed from the mesh if all of the section points at any one integration location have lost their load-carrying capacity.

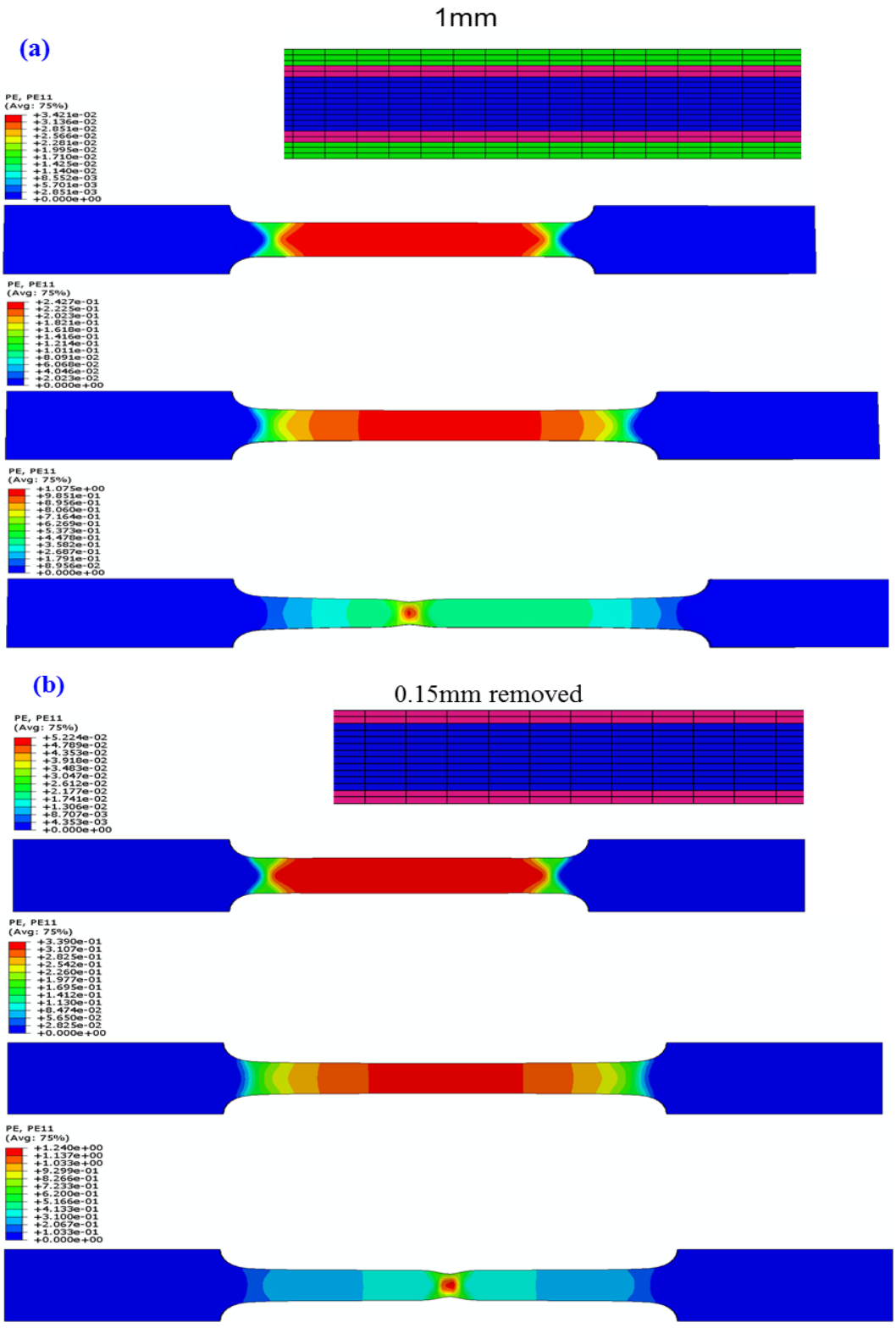
4.2.3 Simulated results and identified parameters

The numerical simulations of three cases (case A, 1mm specimen; case B, 0.7mm specimen, case C, 0.5mm core only specimen) have been realized respectively. Material parameters to be given to ABAQUS/Explicit are listed in the following table 4.2.

Table 4.2 Parameter needed to elastic plastic damage model

Components	Each gradient layer
$\rho(\mathrm{Kg}/m^3)$	Density
$E(\mathrm{GPa})$	Young's modules
ν	Poisson's ratio
A(MPa)	Yield stress
B(MPa)	Hardening coefficient
n	Hardening exponent
$\varepsilon_{fracture}$	Damage starting strain level
η	Triaxiality coefficient
$\bar{u}_{\mathrm{f}}^{\mathrm{pl}}$	Displacement at failure
α	Softening exponent

Figure 4.6(a), (b) and (c) depicts the evolution of equivalent plastic strain for the three cases (case A, 1mm specimen; case B, 0.7mm specimen, case C, 0.5mm core only specimen).


1mm
(a)
PE, PE11
(Avg: 75%)
+3.421e-02
+3.136e-02
+2.851e-02
+2.566e-02
+2.281e-02
+1.995e-02
+1.710e-02
+1.425e-02
+1.140e-02
+8.552e-03
+5.701e-03
+2.851e-03
+0.000e+00
PE, PE11
(Avg: 75%)
+2.427e-01
+2.225e-01
+2.023e-01
+1.821e-01
+1.618e-01
+1.416e-01
+1.214e-01
+1.011e-01
+8.091e-02
+6.068e-02
+4.046e-02
+2.023e-02
+0.000e+00
PE, PE11
(Avg: 75%)
+1.075e+00
+9.851e-01
+8.956e-01
+8.060e-01
+7.164e-01
+6.269e-01
+5.373e-01
+4.478e-01
+3.582e-01
+2.687e-01
+1.791e-01
+8.956e-02
+0.000e+00
(b)
0.15mm removed
PE, PE11
(Avg: 75%)
+5.224e-02
+4.789e-02
+4.353e-02
+3.918e-02
+3.483e-02
+3.047e-02
+2.612e-02
+2.177e-02
+1.741e-02
+1.306e-02
+8.707e-03
+4.353e-03
+0.000e+00
PE, PE11
(Avg: 75%)
+3.390e-01
+3.107e-01
+2.825e-01
+2.542e-01
+2.260e-01
+1.977e-01
+1.695e-01
+1.412e-01
+1.130e-01
+8.474e-02
+5.650e-02
+2.825e-02
+0.000e+00
PE, PE11
(Avg: 75%)
+1.240e+00
+1.137e+00
+1.033e+00
+9.299e-01
+8.266e-01
+7.233e-01
+6.200e-01
+5.166e-01
+4.133e-01
+3.100e-01
+2.067e-01
+1.033e-01
+0.000e+00

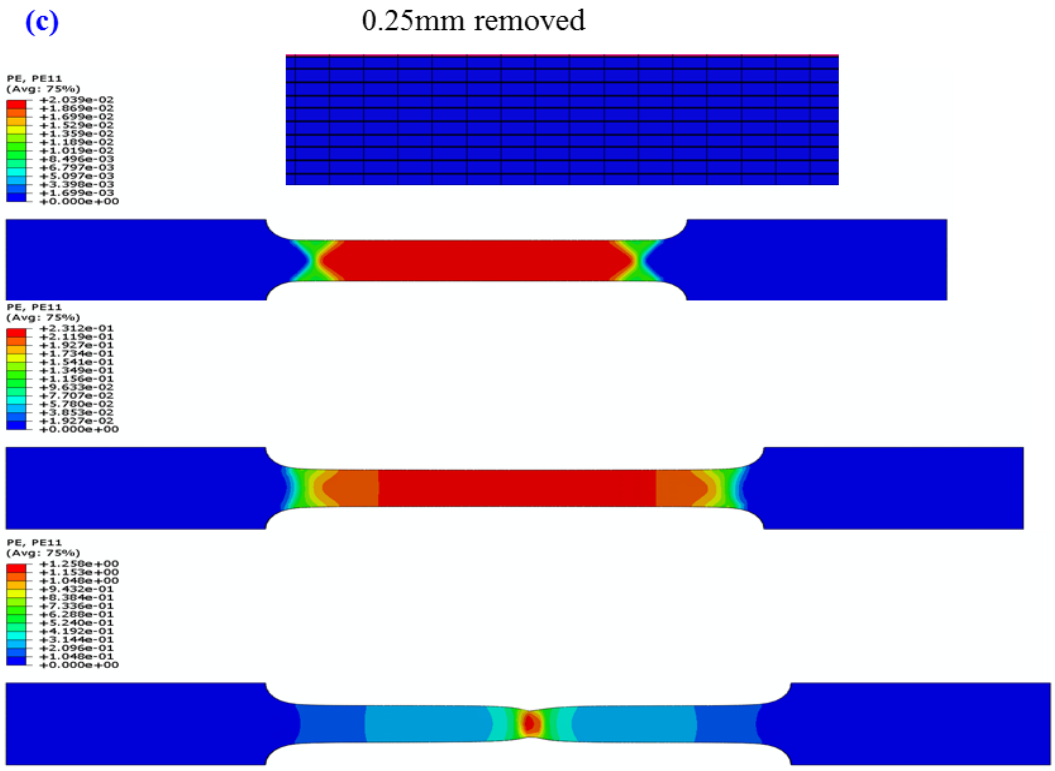


Figure 4.6 Contour of equivalent strain for different cases

As the elastic plastic parameters of each layer are already known, the inverse identification concerns only the damage model parameters ($\varepsilon_{fracture}$, $\bar{u}_f^{pl}$ α).

By adjusting these parameters in the three models, one can finally fit experimental ductile damage evolution and the final fracture point. Figure 4.7 illustrates the best fit found and the identified parameters are given in Table 4.3.

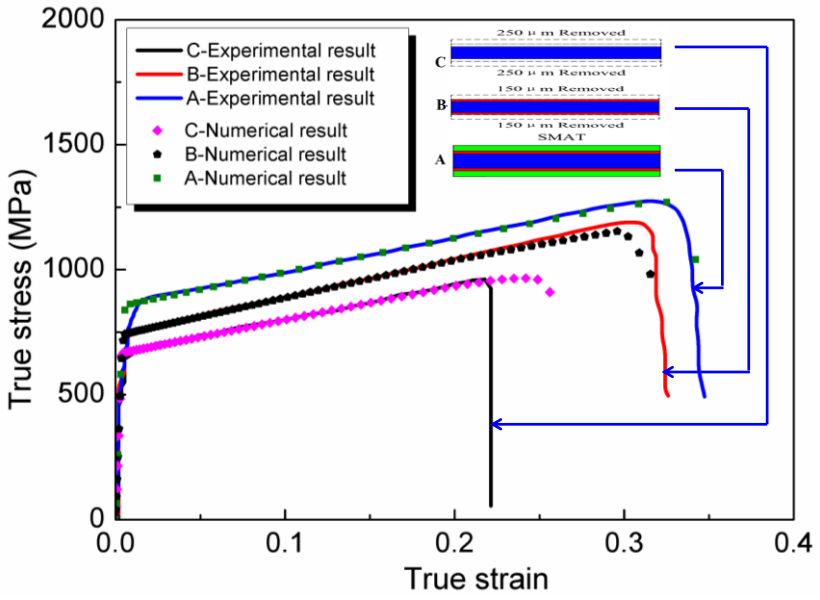


Figure 4.7 Comparison of experimental results and numerical results

Table 4.3 Input parameters of the layers in Abaqus

Components	Top layer	Transition layer	Core layer
$\rho(\mathrm{Kg}/m^3)$	8000	8000	8000
$E(\mathrm{GPa})$	200	200	200
Poisson's ratio(ν)	0.3	0.3	0.3
A	1122.3	924	665
B	1021.3	1894.2	1363.3
$\varepsilon_{fracture}$	0.35	0.35	0.2
$\sigma_{triaxiality}$	0.33	0.33	0.33
Displacement at failure	20	10	3
Softening exponent	1	1	5

4.3 Validation of the identified elastic-plastic damageable model

4.3.1 Quasi-static piercing test

In order to evaluate the performance of the elastic-plastic damageable model as well as the identified parameters given above, a reference structural test is needed. We have selected a piercing test of clamped SMAT treated AISI304 austenitic stainless steel sheet as a reference test.

The testing configuration is basically composed of a hollow clamping support with 40mm inner diameter and a 60 mm circular sheet specimen. This hollow tube-like projectile is made from an aluminum tube with a welded bottom plate at one end. The circular specimens are mounted between the open end of the aluminum tube and an aluminum-clamping ring. The fixture is realized by six uniformly distributed bolts slightly tightened.

Figure 4.8a depicts the scheme of specimen together with the clamping support whereas Figure 4.8b shows the photo of this clamping support and the circular AISI304 austenitic stainless steel sheet of 60 mm diameter. It can be seen that the central part (40mm diameter) are SMAT treated.

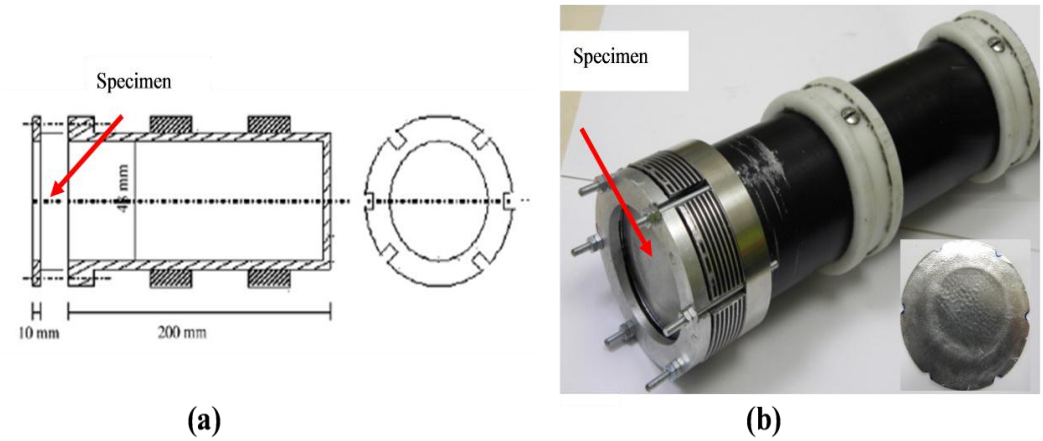


Figure 4.8 Schematic drawing of projectile (a) photo of projectile and specimen (b)

The piercing of the plate specimen mounted on the clamping support is performed at a velocity of 0.1mm/s by MTS810 testing machine using the indenter with diameter of 16mm (Figure 4.9).

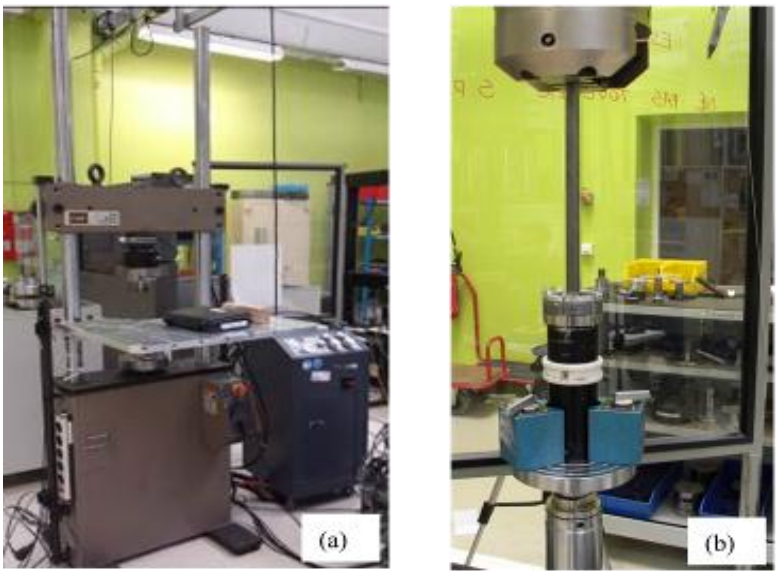


Figure 4.9 MTS 810 setup (a) and fixture of the specimen (b)

In order to evaluate the clamping condition, the interrupted tests were performed through loading-unloading cycles with a displacement of 1mm every cycle. After each unloading, photos are taken and the clamping condition was checked just like what we have done in the double shear testing. No evident slip was observed. The piercing displacement and piercing force curves of all these interrupted tests is in good agreement with that of the continuous test (Figure 4.10), which indicates a good test condition.

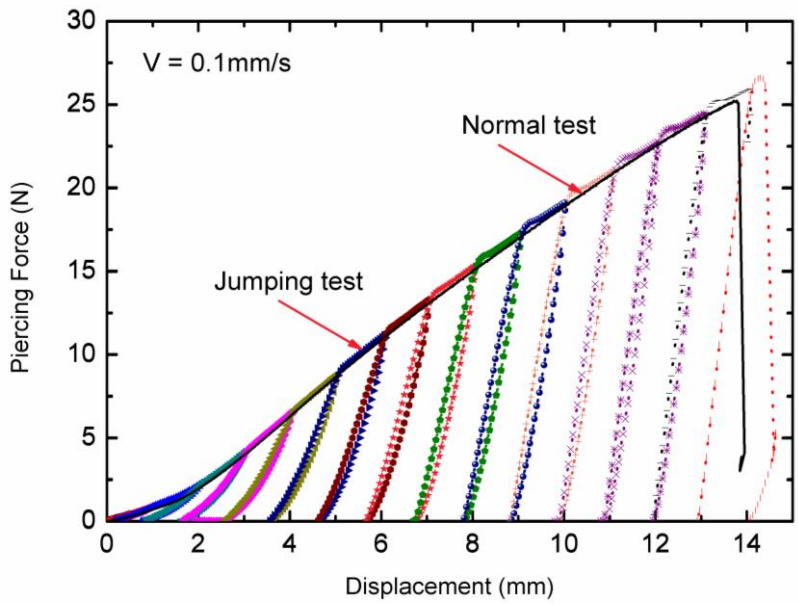


Figure 4.10 Results comparison of the jumping test and the continuing test

4.3.2 Numerical models of the piercing test

Numerical model of this piercing test is built. The specimen/plate was discretized by 8-node linear brick elements with reduced integration and hourglass control (C3D8R). The 1mm thick plate is modeled with five layers as in the tensile tests above: two top hard layers of 0.15mm thick, two transition layers of 0.1mm thick and the inner core layer of 0.5mm thick (Figure 4.11).

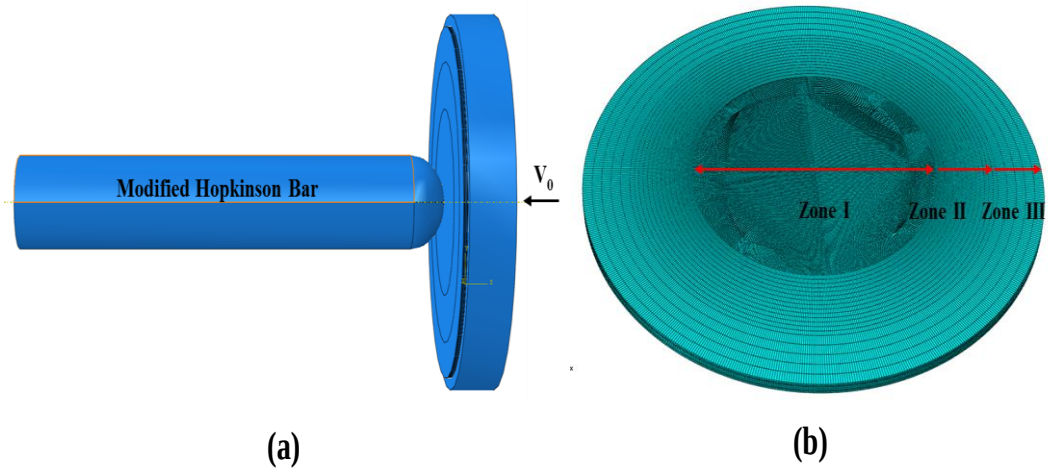


Figure 4.11 Simulation model under quasi-static loading (a) and

Mesh configuration of the specimen (b)

The model is divided into three zones in order to reduce computational time/cost. The central zone I is taken as two times larger than that of the penetrator (16mm) to

ensure accuracy of the model where a refined mesh is used to have an element size of 0.15 mm×0.15 mm×0.05 mm each. Outside this central zone I, larger elements are used in ZoneII and ZoneIII. A convergence study on element size shows that the used elements are small enough for obtaining reliable results within reasonable calculation expense. It is emphasized that the identified constitutive models for each layer listed in Table 4.3 are prescribed. Only the stress triaxiality coefficient is set to 0.66 because an equal bi-axial tension loading is dominant.

The indenter is modeled as rigid cylindrical rod with hemispherical head. A predefined velocity of 0.1mm/s was applied on the specimen. Surface-to-surface contact with penalty contact method is employed. The friction coefficient between specimen and the indenter is set to 0, which is corresponding with the real tests where the lubricant is applied between the specimen and the hemispherical head.

4.3.3 Numerical results and comparisons

Figure 4.12 depicts the piercing force-displacement curve compared to the experimental measurement.

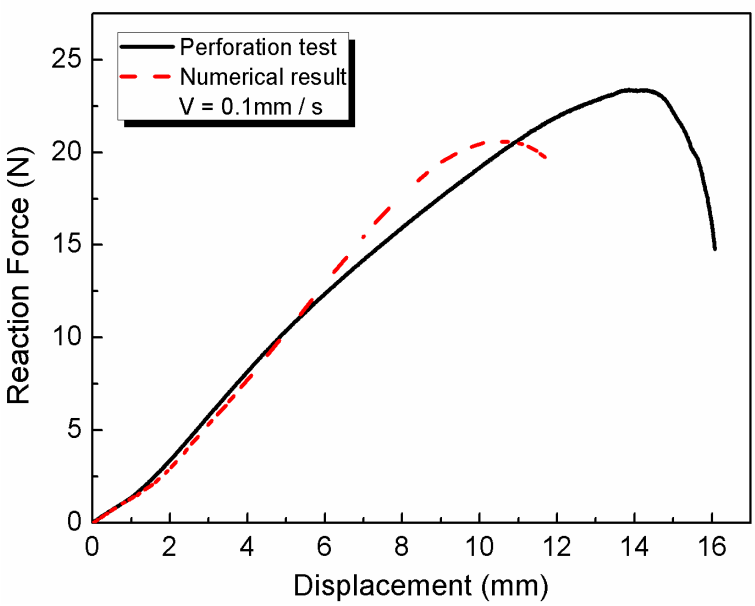


Figure 4.12 Comparisons of numerical results and experimental results under quasi-static loading

It can be seen that at the early stage under 6mm displacement, a perfect agreement is obtained. It means that the testing condition at this stage is well modeled

and elastic plastic part of constitutive model is rather good. However, the numerical model underestimates the peak force and the final failure displacement.

Figure 4.13 depicts the equivalent stress map at the point of final failure compared with experimental post-mortem observation. It seems that the damaged range corresponds to the observed fracture locations.

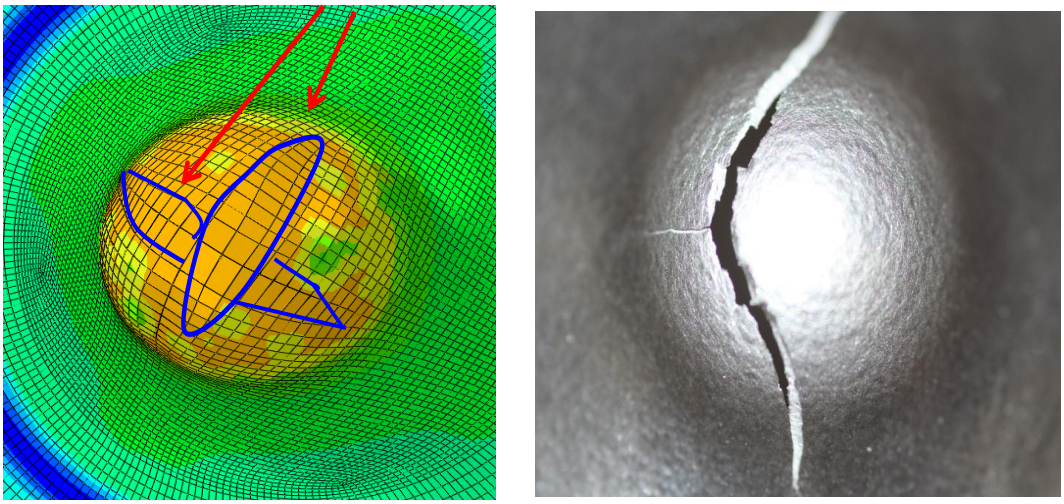


Figure 4.13 Comparison of numerical and experimental fracture morphology at quasi-static loading

It is could be concluded that the proposed elastic-plastic damageable constitutive model can catch qualitatively the main damage/fracture feature in a piercing/indentation test. With the parameters identified using dog-bone tensile testing results, this model can quantitatively reproduce piercing force-displacement with a reasonable error.

4.4 Summary

This chapter presented the parameter identification of a constitutive model for SMAT treated AISI304 austenitic stainless steel sheet. The starting point is the tensile testing results on SMAT treated AISI304 austenitic stainless steel sheet after removing different depth of treated surface.

An elastic-plastic damageable constitutive model is adopted to describe the behavior of each layer. The parameters for each layer are identified using an inverse calculation technique. The three-dimensional ABAQUS/Explicit models with mass scaling are built for the SMAT treated AISI304 austenitic stainless steel tensile

specimen. The best fit of parameters for each layer is obtained by minimizing the error between measured stress and calculated stress for the prescribed strain history.

In order to validate the identified model, a piercing-indentation test is performed. Numerical simulation of such a piercing-indentation test using identified multi-layers constitutive model shows a good agreement with experimental results, which illustrates the efficiency of the proposed elastic-plastic damageable constitutive model.

Chapter 5 Anti-perforation performance of SMAT treated AISI austenitic stainless steel sheet under impact loading and FGM design

5.1 Impact Piercing tests of SMAT treated AISI austenitic stainless steel sheet

Anti-perforation performance is generally evaluated by shooting a projectile on fixed target plate/armor. The projectile can have different shapes warheads (blunt head projectile, conical head projectile and spherical head projectile)[119-123]. The measurement of such a piercing test is rather poor because only the post-mortem observation of the target and the residual velocity of the projectile are the main available[124-140].

The main deficiency of classical free flying projectile-target perforation tests reported in the open literature is the lack of the force recording during the perforation process. An evident solution is to use an instrumented long rod as the projectile, and the piercing force is then measurable from recorded wave profiles as in the case of a Hopkinson pressure bar. However, it was very difficult to launch a long rod at a uniform speed without frictions during the test. In general, a length of several meters is necessary because the measuring duration is determined by the length of the rod over the wave speed. An alternative is to launch the target to strike the perforating long rod[141].

Therefore, zhao and co-workers proposed an inversed perforation testing set-up using a gas gun with a 70mm inner diameter barrel and a 16mm diameter and 6m-long rod with a semi-spherical nose at its perforating end. The rod is instrumented by strain gauges aimed at accurate force measurements during the whole perforation process. Figure 5.1 shows an outline and photos of the experimental set-up. Zeng and Pattofatto[29,142] successfully realized the study on the energy absorption of sandwich structure by using this inverse Hopkinson set-up.

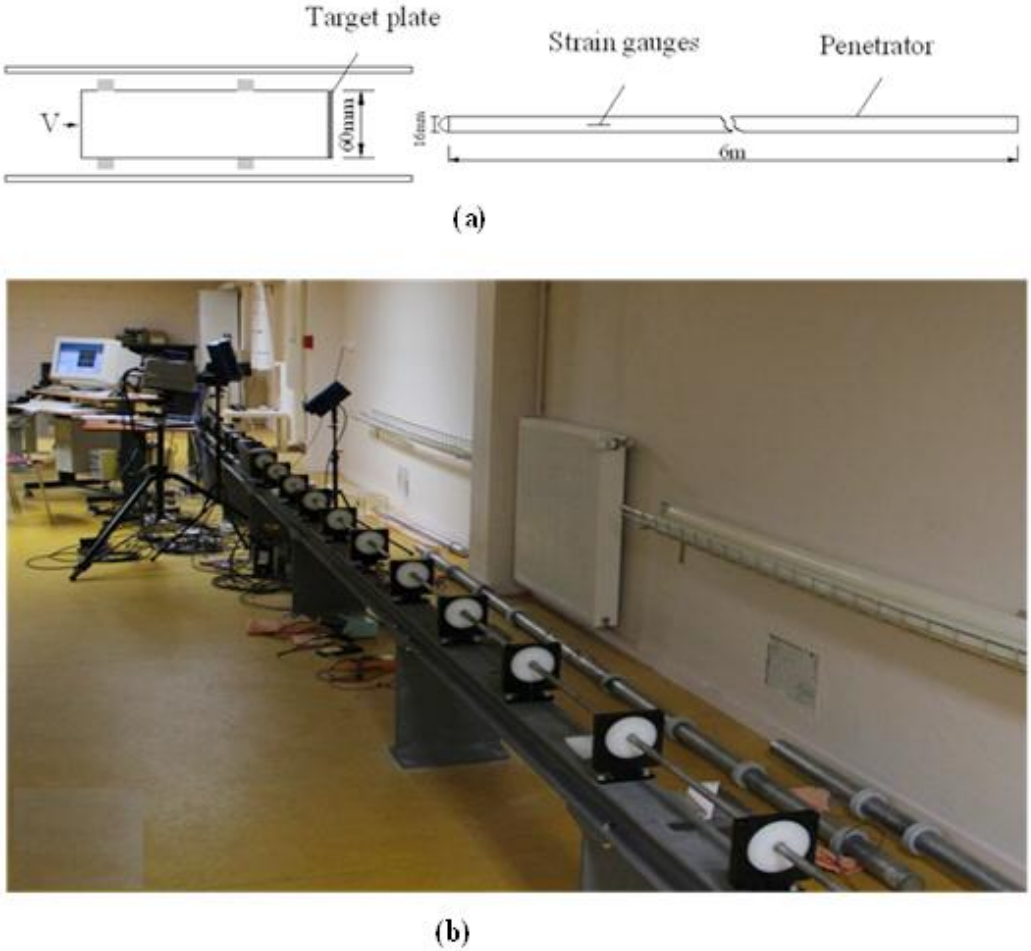


Figure 5.1 Scheme of experimental set-up for perforation

For the penetration tests under dynamic loading, the target plate specimen with the hollow tube-like projectile as that used in our quasi-static piecing test (Figure 4.8) is launched in the barrel. Two Teflon rings are screwed on the tube which allow for a small friction between projectile and the barrel of the gas gun. The tube-like projectile strike on the hemispherical head (the same diameter of 16mm with that under quasi-static loading) Hopkinson bar. The velocity would be obtained from the signals by collecting system. Another technical point concerns how to stop the launched sandwich sample mounted on the hollow projectile after complete perforation. The adopted solution is to use an aluminum honeycomb bumper to absorb the residual energy of the sandwich sample and the projectile. Figure 5.2 shows the aluminum honeycomb bumper and the semi-spherical nose end of the pressure bar.



Figure 5.2 Projectile and Hopkinson pressure bar and experimental setup

With aforementioned inversed penetration testing set-up, the piercing strain impulse $\varepsilon(t)$ can be recorded by the strain gauges cemented on the pressure bars. Indeed, Hopkinson pressure bar analysis is based on the following basic assumption: the waves propagating in the bars can be described by the one-dimensional wave propagation theory. According to this wave propagation theory, the stress and the particle velocity associated with a single wave can be calculated from the associated strain measured by the strain gauges. Therefore, the piercing force and velocity time history $F(t)$, $V(t)$are calculated by

$$F(\mathrm{t}) = S_b E_b \varepsilon(t) \tag{5.1}$$

$$V(\mathrm{t}) = C_b \varepsilon(t) \tag{5.2}$$

where, S_b is the cross section area of pressure bar, E_b is the Young's modulus of Hopkinson bar, C_b is the wave speed of Hopkinson bar, $V(\mathrm{t})$ is the particle velocity of Hopkinson.

$$V_{projectile}(t) = V_0 - \int_0^t \frac{F(\tau)}{M} d\tau \tag{5.3}$$

where, M is a total mass of specimen and impact tube.

According to formulas above, we can induce the relative displacement with time history seen as equation(5.4):

$$U(\mathrm{t}) = \int_0^t (V_{projectile}(t) - V(t)) d\tau \tag{5.4}$$

Typical tension recording from the pressure bar (test at 34m/s) is plotted in Figure 5.3. The piercing force as well as piercing displacement can be calculated from Eqation (5.1) and (5.4).

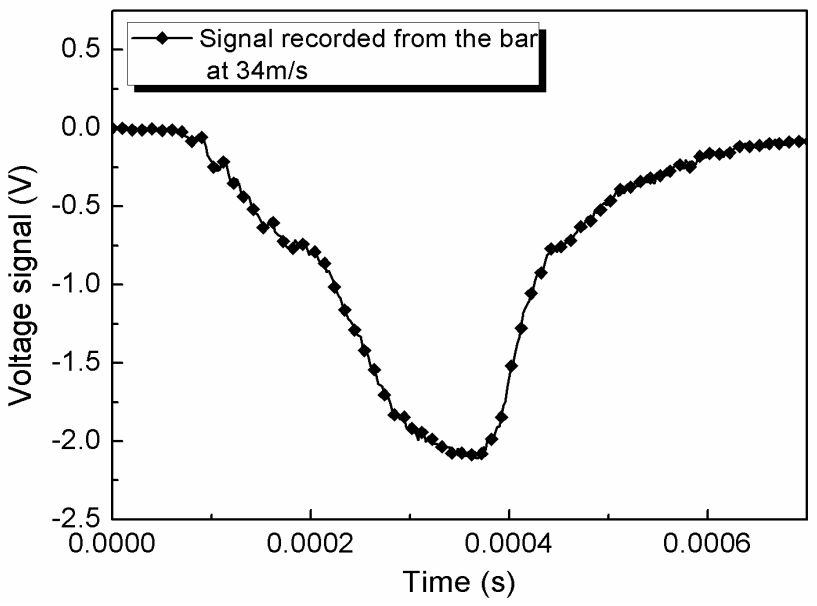


Figure 5.3 Typical time-tension recording from the pressure bar

Figure 5.4 depicts the piercing force-piercing displacement curve obtained in a test of 34mm/s.

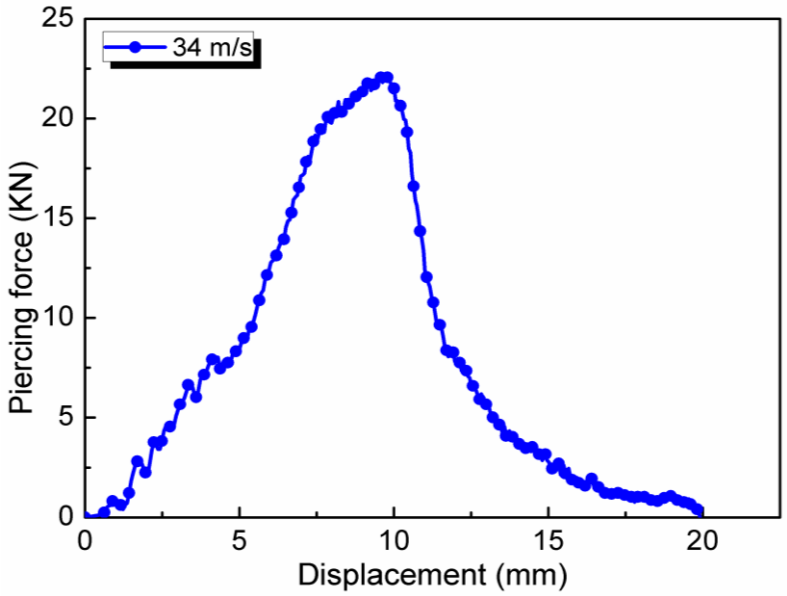


Figure 5.4 Displacement-piercing force curves under impact loading

5.2 Numerical simulation of piercing tests using the a multi-layered elastic plastic rate sensitive constitutive model

5.2.1 Numerical model for piercing test

Numerical model of the impact piercing test is very similar as the quasi-static case presented in the chapter 4. The specimen/plate meshing details are the same. 8-node linear brick elements with reduced integration and hourglass control (C3D8R) are used to form five layers of 1mm thick target plate (Figure 5.5).

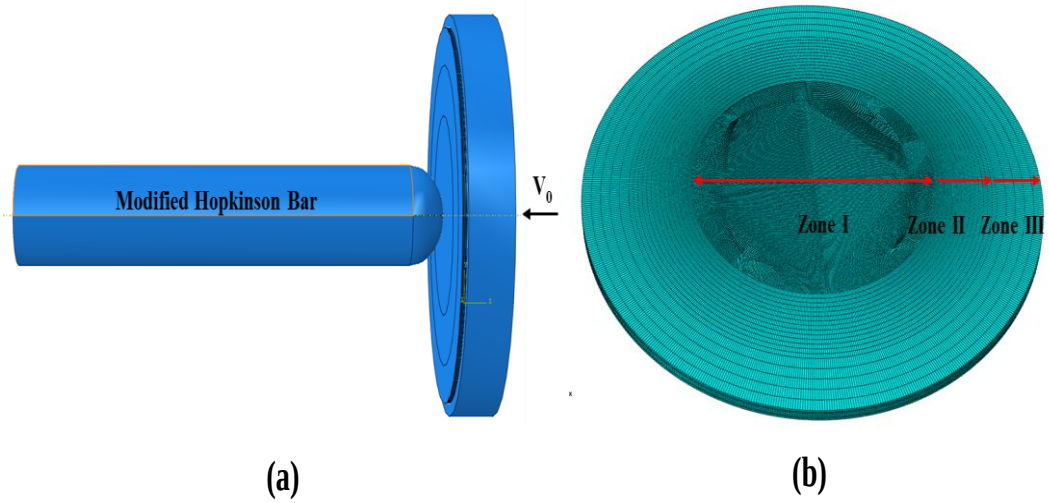


Figure 5.5 Simulation model under impact loading (a) and Mesh configuration of the specimen (b)

The indenter is modeled by a rigid cylindrical rod with hemispherical head. A predefined velocity of 34 m/s was applied on the specimen. Surface-to-surface contact with penalty contact method is employed. The friction coefficient between specimen and the indenter is set to 0, which is corresponding to the real tests where the lubricant is applied between the specimen and the hemispherical head.

5.2.2 Rate sensitivity of the multi-layered elastic plastic constitutive model

The rate sensitivity of the SMAT treated AISI304 austenitic stainless steel sheet has been experimentally investigated in the chapter 2 using in-plane double shear tests.

Quasi static and impact stress-strain curves are available for SMAT treated AISI304 austenitic stainless steel sheet without any removal process as the quasi-static tensile tests. Thus, there is only an overall rate sensitivity. Besides, these shear tests do not contain any information on the fracture feature.

Because of this lack of experimental data, following hypothesis are assumed:

(1) The elastic plastic behavior of each layer has the same rate sensitivity.

(2) The damage starting point and its evolution under impact loading can be described with the same model. However, it might have different parameters.

Under these assumptions, rate sensitivity of the elastic-plastic damageable model can be built. First of all, the damage starting point as well as its evolution parameters remains the same as quasi-static ones for each layer.

The hardening behavior is also supposed to be the same as quasi-static ones; only the yield stress varies with strain rate. It corresponds to the experimental results recalled in figure 5.6.

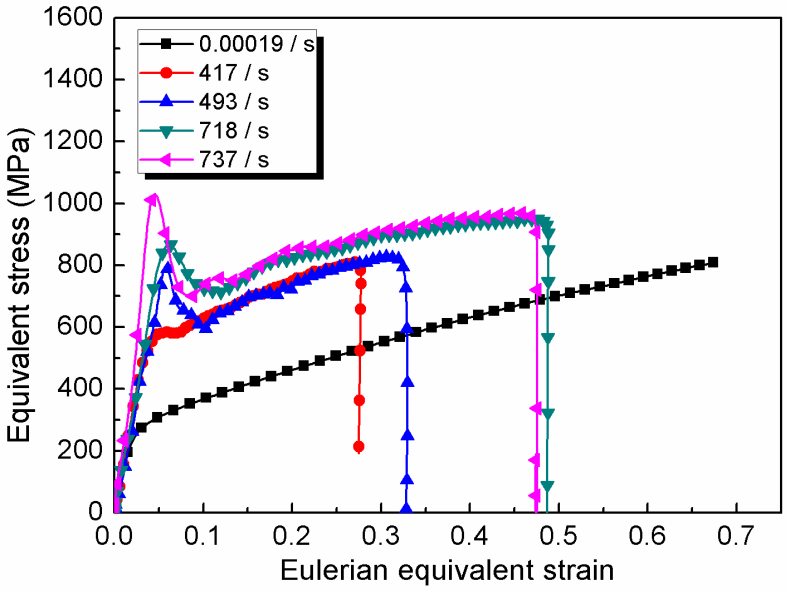


Figure 5.6 Comparison of the equivalent stress and equivalent strain under quasi-static and dynamic loading

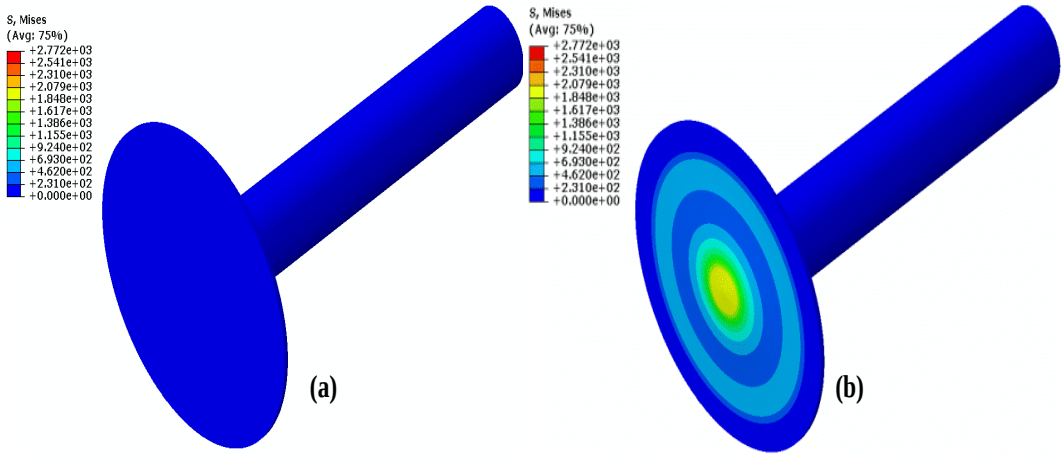
The constitutive model used under impact situation is listed in table 5.1.

Table 5.1 Input parameters of the layers in Abaqus under impact loading

Components	Top layer	Transition layer	Core layer
$\rho(\mathrm{Kg}/m^3)$	8000	8000	8000
$E(\mathrm{GPa})$	200	200	200
Poisson's ratio(ν)	0.3	0.3	0.3
A	1907.9	1570.8	1130.5
B	1736.2	3220.1	2317.5
$\varepsilon_{fracture}$	0.26	0.29	0.18
$\sigma_{triaxiality}$	0.66	0.66	0.66
Displacement at failure	0.2	0.6	0.6
Softening exponent	8	1	8

5.2.3 Numerical results

Figure 5.7 depicts the equivalent stress map at different loading times: a) the indenter just contact the specimen and the stress is zero; b) the indenter head contacts the plate and the stress is starting and expanding in radial direction; c) the contact part of the indenter and the plate starts to damage; d), the overall failure happens on the specimen and the plate finally loses carrying capacity.



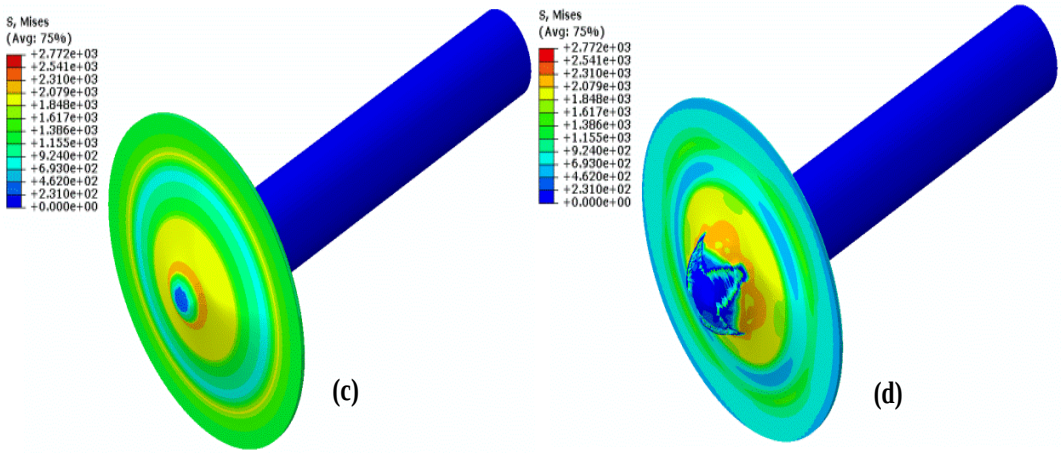


Figure 5.7 Stress contours of different times

5.2.4 Comparisons experiment-simulation

Figure 5.8 depicts the piercing force-displacement curve compared to the experimental measurement. It can be seen that at the early stage, a good agreement is obtained. It means that the testing condition at this stage is well modeled and elastic plastic part of constitutive model is rather good. However, the numerical model overestimates the peak force and underestimates the final failure displacement.

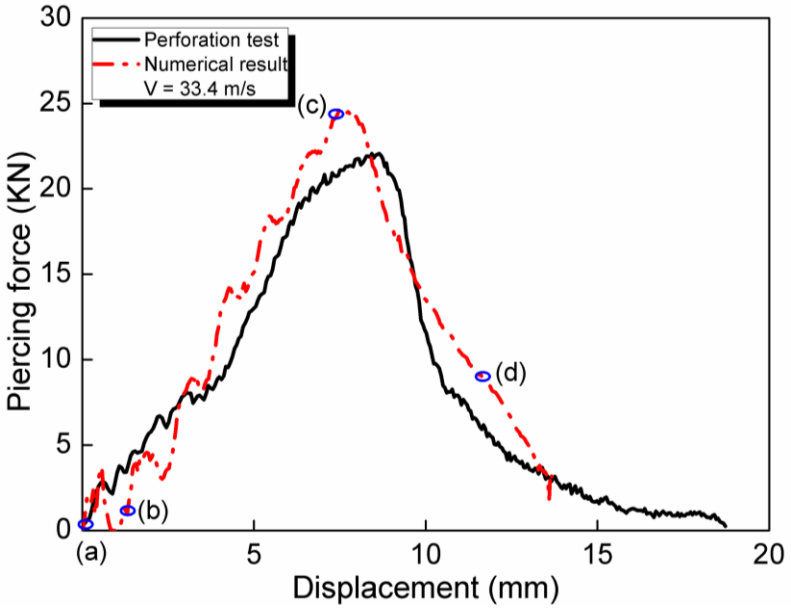


Figure 5.8 Comparisons of numerical results and experimental results under quasi-static loading

Figure 5.9 depicts the equivalent stress map at the point of final failure compared with experimental post-mortem observation. It seems that the damaged range corresponds to the observed fracture locations.

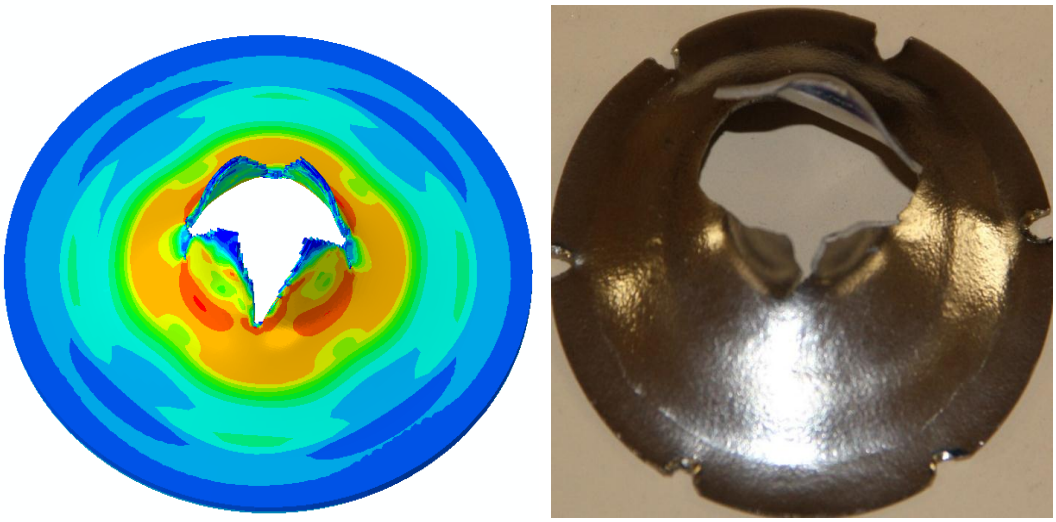


Figure 5.9 Comparison of numerical and experimental fracture morphology at dynamic loading

5.3 Prospective numerical study on FGM design

As already mentioned in the introduction, SMAT treatment can be easily modulated by the treating intensity and duration. A higher treating intensity might lead to a harder top layer while a longer treatment will induce a thicker SMAT layer. Therefore, the property gradient can be easily modified. Besides, one side SMAT treatment can be made instead of two side treatments. It will lead to a monotonically decreasing gradient profile instead of U-form profile. Finally, one can even fabricate a gradient profile with a repeated pattern by cold rolling of a stack of SMAT treated sheets.

It is therefore possible to fabricate a FGM sheet with optimized the gradient profile for a given application. Taking the anti-piercing performance as an example, we can easily simulate the piercing test using various gradient profiles. The simulated results will provide a guide of the more efficient gradient type.

A prospective study on different gradient profile is performed under the condition of the constant average strength of a 1mm thick plate.

The simplest variation from the actually studied SMAT treated AISI304 austenitic stainless steel sheet is to keep the layers thickness but the yield stress of each layer.

Two fictive models are made. One has a sharper yield stress variation than the real case and another has a less sharp gradient profile. Of course, the weighted average strength of these two fictive models is kept the same as the real case. The designed constitutive relations for each graded layer are shown in Figure 5.15 (a), (b) and (c).

$\sigma_{0.15} = 1122.3*(1+0.91\varepsilon_p)$
$\sigma_{0.1} = 924*(1+2.05\varepsilon_p)$
$\sigma_{0.25} = 665*(1+2.05\varepsilon_p)$

(a)

$\sigma_{0.15} = 1730.6*(1+0.6\varepsilon_p)$
$\sigma_{0.1} = 924*(1+2.05\varepsilon_p)$
$\sigma_{0.25} = 300*(1+4.5\varepsilon_p)$

(b)

$\sigma_{0.15} = 913.3*(1+1.1\varepsilon_p)$
$\sigma_{0.1} = 900*(1+2.08\varepsilon_p)$
$\sigma_{0.25} = 800*(1+1.8\varepsilon_p)$

(c)

Figure 5.15 Real gradient(a), Increased gradient(b) and Decreased gradient(c)

Piercing simulations are made for these two gradient profiles using the same numerical model built above with only a gradient profile change. The strain energy time history is plotted in figure 5.16. It can be seen that greater strain energy is found for a sharper gradient profile.

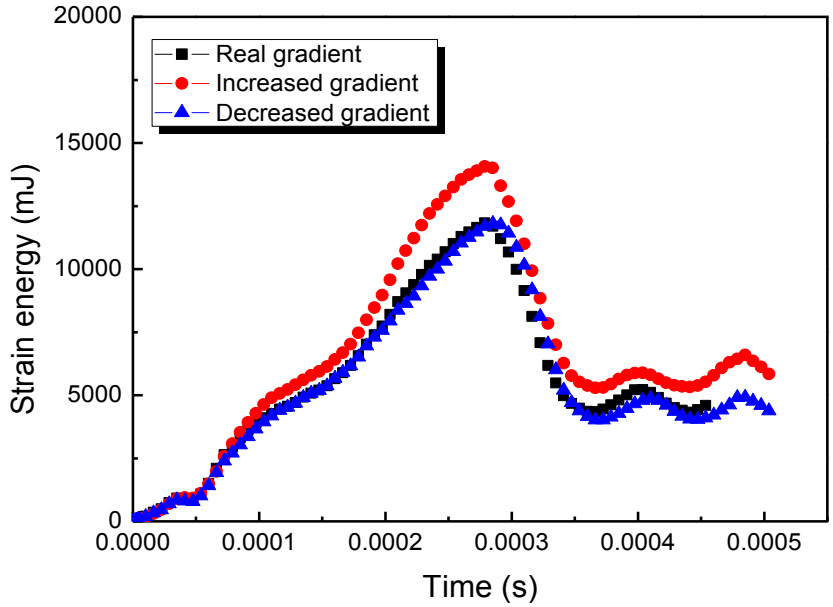


Figure 5.16 Comparisons of the numerical results of three cases

5.4 Summary

In order to evaluate the anti-piercing performance of SMAT treated AISI304 austenitic stainless steel sheet, impact piercing tests on target plates were performed using a 16mm diameter Hopkinson pressure bar.

Quasi static and impact double shear testing results presented in Chapter 2 is used to build the rate sensitive multi-layers elastic plastic damageable constitutive model for the SMAT treated AISI304 austenitic stainless steel sheet. Numerical simulation of the impact piercing tests is realized using ABAQUS/Explicit. A good agreement between simulated result and experiments is found. It implies that not only the proposed constitutive model but also the numerical model of piercing test are efficient.

Finally, a prospective study of the effect of gradient profiles is carried out on the basis of the numerical model.

Chapter 6 Conclusions and perspectives

The presented works in this Ph.D dissertation aimed at the comprehensive understanding and the constitutive modeling of the mechanical behaviours of the SMAT treated AISI304 stainless steel sheet under a large range of loading rates. SMAT treated AISI304 stainless steel sheets are multi-layered functionally graded materials (FGM). The main research results and conclusions are summarized as followed:

(1) The overall rate sensitivity SMAT treated AISI304 stainless steel sheet is characterized by the double shearing tests under quasi-static and dynamic loading where a large strain can be achieved without geometry instability. Impact double shear test are performed with a large diameter Hopkinson bar system and an adapted equal-impedance clamping device. Significant rate sensitivity (about 70% strength enhancement) is found. It is also observed that such a rate enhancement does not induce an important reduction of the ductility.

(2) In order to extract accurate material information from the double shear tests, their testing conditions are thoroughly analyzed using numerical simulation. Numerical models including clamping devices have been built to investigate the influence of this clamping device at the early stage of loading. A limited effect was found for various imperfect testing conditions such as the clamping device stiffness, non-homogeneous stress and strain fields, non-equilibrium state, etc. On the contrary, numerical and analytical study shows that the simple small strain assumption usually used in double shear tests is not accurate enough. Eulerian cumulated strain definition should be used to get consistent numerical results. From this finding, the experimental rate sensitivity obtained for the SMAT treated AISI304 stainless steel sheet are recalculated.

(3) A multi-layers elastic plastic damageable constitutive model is proposed to model SMAT treated AISI304 stainless steel sheet. The parameters are identified using tensile testing results. The elastic plastic behavior is curved fitted with a simple Ludwig hardening model. However, the damage parameters should be identified using an inverse method on the basis of numerical simulation of these tensile tests. In order to validate this multi-layer elastic plastic damageable constitutive model, indentation/piercing tests on SMAT treated AISI304 stainless steel sheet are

performed. Numerical simulation of this indentation/piercing tests is also realized. It is found that the identified multi-layer elastic plastic damageable constitutive model allows a quite accurate prediction of the experimental piercing tests.

(4) In order to evaluate the impact anti-piercing capacity of the SMAT treated AISI304 stainless steel sheet, the impact perforation tests using Hopkinson bar are carried out. Numerical simulation of these impact perforation tests are realized with a similar FEM model as the quasi-static case. As the rate sensitivity of SMAT treated AISI304 stainless steel sheet is experimentally characterized with double shear test, a rate sensitive multi-layer elastic plastic damageable constitutive model is introduced. The numerical results agree well with the experimental ones, which indicate the effectiveness of the numerical model as well as the rate sensitive multi-layer elastic plastic damageable constitutive model.

The presented Ph.D work illustrates the possibility to characterize and to model SMAT treated AISI304 stainless steel sheet, which is a easily adaptable functionally graded material. The identified rate sensitive multi-layer elastic plastic damageable constitutive model can be used to predict various structural responses under quasi static and dynamic loading. Even though the testing configurations as well as constitutive models are not perfect and can surely be improved in the future, but the actual proposed models provide already reasonable predictive simulations.

The methodology proposed in this work can be easily applied for other FGM materials. It does give a new perspective to make numerical graded materials and to possibly fabricate a FGM sheet with an optimized gradient profile for a given application. Taking the anti-piercing performance as an example, various gradient profiles are tested virtually for the piercing tests. Offering a guide of the more efficient gradient type is already possible.

References

[1] T.Arciszewski, J.Cornell. Bio-inspiration: Learning Creative Design Principia. Intelligent computing in Engineering and Architecture, 4200:32-53(2006).

[2] C.Ortiz, M.C.Boyce. Bioinspired Structural Materials. Science, 319(5866):1053-1054(2008).

[3] S.Weiner, L.Addadi. Design strategies in mineralized biological materials. Journal of Materials Chemistry, 7(5):689-702(1997).

[4] K.S.TAI, H.J.QI, C.ORTIZ. Effect of mineral content on the nanoindentation properties and nanoscale deformation mechanisms of bovine tibial cortical bone. Journal of Materials Science: Materials in Medicine,16(10):947-959(2005).

[5] F.Nogata, H.Takahashi. Intelligent functionally graded material: Bamboo. Composite Engineering, 5(7):743-751(1995).

[6] C.Mattheck. Teacher tree: The evolution of notch shape optimization from complex to simple. Engineering Fracture Mechanics, 73:1732-1742(2006).

[7] M.Koizumi. FGM activities in Japan. Composites Part B, 28B: 1-4(1997).

[8] B.Chen, X.H.Peng, H.Jing. Microstructure of natural biocomposites and research of biomimetic composites. Acta Materialae Compositae Sinica, 17(3): 59-62(2000).

[9] D.K.Jha, T.Kant, R.K.Singh. A critical review of recent research on functionally graded plates. Composite Structures, 96:833-849(2013).

[10] J.F.B.Benjamin, S.Juha, C.B.Mary, O.Christine. Materials design principles of ancient fish armour. Nature materials, 1-9(2008).

[11] D.J.Klaus. Fishing for compliance. Nature materials, 7:692-693(2008).

[12] C.Daniel, T.J.Balk, T.Wübben, F.Mücklich. Bio-mimetic scaling of mechanical behavior of thin films, coatings, and surface by laser interference metallurgy. Advanced engineering materials, 7(9): 823-826(2005).

[13] Q.L.Feng. Review of current biomineralization and bio mimetic materials .Journal of Tsinghua University(Science & Technology), 45(3): 378-383(2005).

[14] A.Gilchrist, N.J.Mills. Modelling of the impact response of motorcycle helmets. International Journal of Impact Engineering, 15:201-218(1994).

[15] G.Liu, L.Zhou. Surface Nanocrystallization Technique of the Engineering Metalli

Materials. Nanotechnology, 3(1):51-56(2006).

[16] G.Liu, S.C.Wang, X.F.Lou, J.Lu, K.Lu. Low carbon steel with nanostructured surface layer induced by high energy shot peening. Scripte Materialia, 44(8):1791-1795(2001).

[17] G.Liu, X.P.Luan, K.Lu. The current situation of researches of surface-nanocrystallization on metallic materials. China Surface Engineering, 52(3):1-5(2001).

[18] J.J.Wu, Y.Li, D.M.Sun. Research progress of the metal surface self-nanocrystallization. Heat Treatment Technology and Equipment,34(1):41-45(2013).

[19] K.Yasuna, M.Terauchi, A.Otsuki, K.N.Ishihara, P.H.Shingu. Formation of nanoscale Fe:Ag multi-layer by repeated press-rolling and its layer thickness dependence of magneto resistance. Materials Science and Engineering A, 85:412-417(2000).

[20] J.G.Luo, V.L.Acoff. Using cold roll bonding and annealing to process Ti/Al multilayered composites from elemental foils. Materials Science and Engineering A, 379:164-172(2004).

[21] T.J.Nobuhiro, S.Yoshihiro, S.H.Lee, M.Yoritoshi. ARB and other new techniques to produce bulk ultrafine grained materials. Advanced Engineering Materials, 5(5):338-344(2003).

[22] P.C.Gajanan, A.Viola. Cold roll bonding of multi-layered bi-metal laminate composites. Composites Science and Technology, 69:1667-1675(2009).

[23] F.Carreno, J.Chao, M.Pozuelo, O.A.Ruano. Microstructure and fracture properties of an ultrahigh carbon steel–mild steel laminated composite. Scripta Materialia, 48:1135-1140(2003).

[24] H.Y.Wu, S.Lee, J.Y.Wang Solid-state bonding of iron-based alloys, steel-brass, and aluminum alloys. Journal of Materials Processing Technology,75(1-3): 173-179(1998).

[25] J.J.Moore, D.V.Wilson, W.T.Roberts. Fabrication of formable metal-metal composites. Materials Science and Engineering, 48:113-121(1981).

[26] T.U.Tamots, T.Makoto, K.Yoshihisa, K.Shiomi， Preparation and hydrogen storage properties of Mg-Ni-Mg2Ni laminate composites. Journal of Alloys and Compounds, 386:253-257(2005).

[27] M.Eizadjou, A.K.Talachi, H.D.Manesh, H.S.Shahabi, K.Janghorban.

Investigation of structure and mechanical properties of multi-layered Al/Cu composite produced by accumulative roll bonding (ARB) process. Composites Science and Technology, 68: 2003-2009(2008).

[28] S.Kundu, M.Ghosh, A.Laik, K.Bhanumurthy, G.B.Kale, S.Chatterjee. Diffusion bonding of commercially pure titanium to 304 stainless steel using copper interlayer. Materials Science and Engineering A, 407:154-160(2005).

[29] H.B.Zeng, S.Pattofatto, H.Zhao, Y.Girard, V.Fascio. Impact behavior of hollow sphere agglomerates with density gradient. International Journal of Mechanical Sciences, 52:680-688(2010).

[30] H.B.Zeng, S.Pattofatto, H.Zhao, Y.Girard, V.Fascio. Perforation of sandwich plates with graded hollow sphere cores under impact loading. International Journal of Impact Engineering, 37(11):1083-1091(2010).

[31] H.N.G.Wadley, M.R.O'Masta, K.P.Dharmasena, B.G.Compton, E.A.Gamble, F.W.Zok. Effect of core topology on projectile penetration in hybrid aluminum/alumina sandwich structures. International Journal of Impact Engineering, 62:99-113(2013).

[32] Q.J.Yu, Y.L.Li. Q.Deng, Z.B.Tang, F.Xu. Penetration of SiCp/Al functionally graded plates-Experiment and numerical simulation. Acta Material Composite Sinica, 24(5): 6-12(2007).

[33] A.Tasdemirci, I.W.Hall. The effects of plastic deformation on stress wave propagation in multi-layer materials. International Journal of Impact Engineering, 34(11):1797-1813(2007).

[34] A.Tasdemirci, I.W.Hall. Experimental and Modeling Studies of Stress Wave Propagation in Multilayer Composite Materials: Low Modulus Interlayer Effects. Journal of Composite Materials, 39(11): 981-1005(2005).

[35] A.Tasdemirci, I.W.Hall, A.Gama. Stress Wave Propagation Effects in Two-and Three-layered Composite Materials. Journal of Composite Materials, 38(12): 995-1009(2004).

[36] Chakraborty, S.Gopalakrishnan. A spectrally formulated finite element for wave propagation analysis in functionally graded beams. International Journal of Solids and Structures, 40(10): 2421-2448(2003).

[37] A.Berezovski, J.Engelbrecht, G.A.Maugin. Numerical simulation of two-dimensional wave propagation in functionally graded materials. European Journal of Mechanics - A/Solids, 22(2):257-265(2003).

[38] G.R.Liu, X.Han, K.Y.Lam. Stress waves in functionally gradient materials and its use for material characterization. Composites Part B: Engineering, 30(4): 383-394(1999).

[39] G.R.Liu, X. Han, Y. G. Xu, K. Y. Lam. Material characterization of functionally graded material by means of elastic waves and a progressive-learning neural network. Composites Science and Technology, 61(10):1401-1411(2001).

[40] H.A.Bruck. A one-dimensional model for designing functionally graded materials to manage stress waves. International Journal of Solids and Structures, 37(44): 6383-6395(2000).

[41] Y.L.Li, K.T.Ramesh, E.S.C.Chin. Dynamic characterization of layered and graded structures under impulsive loading. International Journal of Solids and Structures, 38(34-35): 6045-6061(2001).

[42] T.Z.Li, F.C.Jiang, E.A.Olevsky, K.S.Vecchio, M.A.Meyers. Damage evolution in Ti6Al4V-Al3Ti metal-intermetallic laminate composites. Materials Science and Engineering A, 443(1-2): 1-15(2007).

[43] N.Masahashi, S.Watanabe, N.Nomura, S.Semboshi, S.Hanada. Laminates based on an iron aluminide intermetallic alloy and a CrMo steel. Intermetallics, 13:717-726(2005).

[44] A.E.Markaki, T.W.Clyne. Energy absorption during failure of layered metal foam/ceramiclaminates. Materials Science and Engineering A,323:260-269(2002).

[45] B.Q.Jiang. Study on penetration resistance of functionally graded plate and numerical analysis of bird on balance beam Outrigger. Xi'an, Northwestern Polytechnical Univercity, 2004.

[46] J.G.Hetherington, B.P.Rajagopalan. An investigation into the energy absorbed during ballistic perforation of composite armours. International Journal of Impact Engineering, 11:33-40(1991).

[47] S.K.Hui, T.X.Yu. Modelling of the effectiveness of bicycle helmets under impact. International Journal of Mechanical Sciences, 44(6):1081-1100(2002).

[48] K.X.He, W.G.Guo, X.Q.Zhang, Y.Z.Ge, C.N.Yan, W.J.Zhang. Study on Absorbing Energy Character of Functionally Graded Plate of GFRP/CFRT. Advances in Aeronautical Science and Engineering, 2(3):276-281(2011).

[49] J.Lopez-Puente, A.Arias, R.Zaera, C.Navarro. The effect of the thickness of the adhesive layer on the ballistic limit of ceramic/metal armours. An experimental andnumerical study. International Journal of Impact Engineering, 32:321-

336(2005).

[50] S.Yadav, G.Ravichandran. Penetration resistance of laminated ceramic/polymer structures. International Journal of Impact Engineering, 28:557-574(2003).

[51] J.Radin, W.Goldsmith. Normal projectile penetration and perforation of layered targets. International Journal of Impact Engineering, 7:229-259(1988).

[52] L.Marom, S.R.Bodner. Projectile perforation of multi-layered beams. International Journal of Mechanical Science, 21:489-504(1979).

[53] R.S.J.Corran, P.J.Shadbolt, C.Ruiz. Impact loading of plates an experimental investigation. International Journal of Impact Engineering, 1:3-22(1983).

[54] N.K.Cupta, V.Madhu. An experimental study of normal and oblique impact of hard-core projectile on single and layered plates. International Journal of Impact Engineering, 5-6:395-414(1997).

[55] M.Huang. Ballistic resistance of multi-layered steel shields. Beijing, 131-135(2007).

[56] X.Teng, T.Wierzbicki, M.Huang. Ballistic resistance of double-layered armor plates. International Journal of Impact Engineering, 35:870-884(2008).

[57] E.A.Flores-Johnson, M.Saleh, L.Edwards. Ballistic performance of multi-layered metallic plates impacted by a 7.62-mm APM2 projectile. Materials Science and Engineering A, 323:260-269(2002).

[58] J.G.Liu, S.Pattofatto, D.N.Fang, F.Y.Lu, H.Zhao. Impact strength enhancement of aluminum tetrahedral lattice truss core structures. International Journal of Impact Engineering, 79:3-13(2015).

[59] Z.Wei, K.P.Dharmasena, H.N.G.Wadley, A.G.Evans. Analysis andinterpretation of a test for characterizing the response of sandwich panels to water blast. International Journal of Impact Engineering, 34:1602-1618(2007).

[60] W.Z.Wang. Experimental and Numerical Study on Impact Damage of Typical Aircraft Structures .Xian: Northwestern Polytechnical University, 60-63(2012).

[61] H.W.Zhang, G.Liu, Z.K.Hei, J.Lu, K.Lu. Surface nanocrystallization of AISI304 stainless steel induced by surface mechanical attrition treatment I. Structure and property. Acta Metallurgica Sinica, 39(4): 342-346(2003).

[62] K.Lu, J.Lu. Surface nanocrystallization (SNC) of metallic materials: presentation of the concept behind a new approac . Materials Science Technology， 15(3):193-197(1999).

[63] N.R.Tao, Z.B.Wang, W.P.Tong, M.L.Sui, J.Lu, K.Lu. An investigation of surface

nanocrystallization mechanism in Fe induced by surface mechanical attrition treatment. Acta Materialia, 50:4603-4616(2002).

[64] K.Y.Zhu, A.Vassel, F.Brisset, K.Lu, J.Lu. Nanostructure formation mechanism of alpha-titanium using SMAT. Acta Materialia, 52:4101-4110(2004).

[65] A.Y.Chen, D.F.Li, J.B.Zhang, H.W.Song, J.Lu. Make nanostructured metal exceptionally tough by introducing non-localized fracture behaviors. Scripta Materialia, 59:579-582(2008).

[66] Y.M.Lin, J.Lu, L.P.Wang, T.Xu, Q.J.Xue. Surface nanocrystallization by surface mechanical attrition treatment and its effect on structure and properties of plasma nitrided AISI 321 stainless steel. Acta Materialia, 54:5599-5605(2006).

[67] M.F.Doener, W.D.Nix. A method for interpreting the data from depth-sensing indentation instruments. Journal of Materials Research, 1:601(1986).

[68] W.C.Oliver, G.M.Pharr. An improved technique for determining hardness and elastic modulus using load and displacement sensing indentation experiments. Journal of Materials Research, 7:1564(1992).

[69] S.Suresh, A.E.Giannakopoulos. A new method for estimating residual stresses by instrumented sharp indentation. Acta Materialia, 46:5755-5767(1998).

[70] S.Carlsson, P.L.Larsson. On the determination of residual stress and strain fields by sharp indentation testing: Part1: theoretical and numerical analysis. Acta Materialia, 49:2179-2191(2001).

[71] S.Carlsson, P.L.Larsson. On the determination of residual stress and strain fields by sharp indentation testing: Part II. Experimental investigation. Acta Materialia, 49:2193-2203(2001).

[72] J.G.Swadener, B.Taljat, G.M.Pharr. Measurement of residual stress by load and depth sensing indentation with spherical indenters. Journal of Materials Research, 16:2091-2102(2001).

[73] J.G.Swadener, E.P.George, G.M.Pharr. The correlation of the indentation size effect measured with indenters various shapes. Journal of Mechanics Physics Solids, 150:681-694(2002).

[74] M.Dao, N.Chollacoop, K.J.Van-Vliet, T.A.Venkatesh, S. Suresh. Computational modeling of forward and reverse problems in instrumented sharp indentation. Acta Materiallia, 49:3899-3918(2001).

[75] J.L.Bucaille, S.Stauss, E.Felder, J.Michler. Determination of plastic properties of metals by instrumented indentation using different sharp indenters. Acta

Materialia, 51: 1663-1678(2003).

[76] N.Chollacoop, M.Dao, S.Suresh. Depth-sensing instrumented indentation with dual sharp indenters[J]. Acta Materialia, 51:3713-3729(2003).

[77] A.E.Giannakopoulos, S.Suresh. Determination of elastoplastic properties by instrumented sharp indentation. Scripta Materialia, 40:1191-1198(1999).

[78] M.Futakawa, T.Wakui, Y.J.Tanabe, I.Ioka. Identification of the constitutive by the indentation technique using plural indenters with different apex angles. Journal of Materials Research, 16:2283-2292(2001).

[79] A.E.Giannakopoulos. Indentation of plastic graded substrates by sharp indenters. International Journal of Solids and Structures, 39:2495-2515(2002).

[80] W.Capehart, Y.T.Cheng. Determining constitutive models from conical indentation: a sensitivity analysis. Journal of Materials Research, 18: 827-832(2003).

[81] M.Mata, J.Alcal á. Mechanical property evaluation through sharp indentations in elastoplastic and fully plastic contact regimes. Journal of Materials Research, 18:1705-1709(2003).

[82] A.DiCarlo, H.T.Y.Yang, S.Chandrasekar. Semi-inverse method for predicting stress-strain relationship from cone indentations. Journal of Materials Research, 18: 2068-2078(2003).

[83] J.L.Bucaille, S.Stauss, P.Schwaller, J.Micher. Thin Solid Films, 447-448:239(2004).

[84] M.Mata, J.Alcala. The role of friction on sharp indentation. Journal of the Mechanics and Physics of Solids, 52: 145-165(2004).

[85] Y.P.Cao, J.Lu. Depth-sensing instrumented indentation with dual sharp indenters: stability analysis and corresponding regularization schemes. Acta Materialia, 52:1143–1153(2004).

[86] Y.P.Cao, J.Lu. A new scheme for computational modeling of conical indentation in plastically graded materials. Journal of Materials Research, 19:1703-1716(2004).

[87] H.W.Zhang, Z.K.Hei, G.Liu, J.Lu, K.Lu. Formation of nanostructured surface layer on AISI 304 stainless steel by means of surface mechanical attrition treatment. Acta Materialia, 51:1871-1881(2003).

[88] B.Hopkinson. A method of measuring the pressure in the deformation of high explosives by the impact of bullets. Philosophical Transactions of the Royal

Society of London, A213: 437-452(1914).

[89] H.Kolsky. An investigation of mechanical properties of materials at very high rates of loading. Proceedings of the Physics Society of London, Series B 62: 676-700(1949).

[90] G.Gary, P.Bailly. Behaviour of quasi-brittle material at high strain rate. Experiment and modeling. European Journal of Mechanics A-Solids, 17(3):403-420(1998).

[91] R.Fandrich, J. Clout, F. Bourgeois. The CSIRO Hopkinson Bar Facility For Large Diameter Particle Breakage. Minerals Engineering, 11(9):861-869(1998).

[92] H.Zhao, S.Abdennadher. On the strength enhancement under impact loading of square tubes made from rate insensitive metals. International Journal of Solids and Structures, 41 (24-25):6677 -6697(2004).

[93] H.Zhao, G.Gary. A three dimensional analytical solution of the longitudinal wave propagation in an infinite linear viscoelastic cylindrical bar. Application to experimental techniques. Journal of the Mechanics and Physics of Solids, 43 (8):1335 -1348(1995).

[94] L.Pochhammer. Uber Fortplanzungsgeschwindigkeiten kleiner Schwingungen in einem unbergrenzten isotropen Kreiszylinder, Journal fur die Reine und Angewandte Mathematik, 81: 324(1876).

[95] C.Chree. The equations of an isotropic elastic solid in polar and cylindrical coordinates, their solution and applications, Transactions Cambridge Philosophical Society, 14:251-369(1899).

[96] E.D.H.Davies, S.C.Hunter. The dynamic compression test of solids by the method of the split Hopkinson pressure bar (SHPB). Journal of Mechanics Physics of Solids, 11:155-179(1963).

[97] J.Z.Malinowski, J.R. Klepaczko. A unified analytic and numerical approach to specimen behavior in the split-hopkinson pressure bar. International Journal of Mechanical Sciences, 28:381-391(1986).

[98] N.Iosipescu. New accurate procedure for single shear testing of metals. Journal of Materials, 2:537-566(1967).

[99] C.G'sell, S.Boni, S.Shrivastava. Application of the plane simple shear test for determination of the plastic behaviour of solid polymers at large strains. Journal of Materials Science, 18(3):903-918(1983).

[100] F.Pierron, A.Vautrin, B.Harris. The losipescu in-plane shear test: validation on

an isotropic material. Experimental Mechanics, 35(2):130-136(1995).

[101]M.Arcan, Z.Hashin, A.Voloshin. Method to produce uniform plane stress states with applications to fiber-reinforced materials. Experimental Mechanics, 18(4):141-146(1978).

[102]K.Yoshida, K.Myauchi. Experimental studies of mechanical behavior as related to sheet metal forming, mechanics of sheet metal forming. New York: Plenum Press, 19-49(1978).

[103]J.D.Campbell, W.G.Ferguson. The temperature and strain-rate dependence of the shear strength of mild steel. Philosophical Magazine, 21(169):63-82(1970).

[104]Y.Z.Guo, Y.L.Li. A novel approach to testing the dynamic shear response of Ti-6Al-4V. Acta Mechanica Solida sinica, 25(3):299-311(2012).

[105]J.Harding, J.Huddart. The use of the double-notch shear test in determining the mechanical properties of uranium at very high rates of strain. In: Proc. 2nd international conf. mechanical properties at high rates. London: The Institute of Physics, 49-61(1979).

[106]J.R.Klepaczko. Plastic shearing at high and very high strain rates. Journal of Physics IV, 4(C8):C8-C35-C8-C40(1994).

[107]Gary G, Nowacki WK. Essai de cisaillement plan applique a des toles minces. Journal of Physics IV, 4(C8): C8-C65-C8-C70(1994).

[108]R.Merle, H.Zhao. On the errors associated with the use of large diameter SHPB, correction for radially non-uniform distribution of stress and particle velocity in SHPB testing. International Journal of Impact Engineering, 32(12):1964-1980(2006).

[109]Merle R. Mise en oeuvre et analyse d'un essai de double cisaillement en grandes deformations sous sollicitations dynamiques [Ph.D. thesis of ENS Cachan], 2006.

[110]J.R.Klepaczko, H.V.Nguyen, W.K.Nowacki. Quasi-static and dynamic shearing of sheet metals. European Journal of Mechanics A-Solids, 18(2):271-289(1999).

[111]Rodr ǵuez-Mart ńez J A, Rusinek A, Pesci R. Experimental survey on the behaviour of AISI 304 steel sheets subjected to perforation. Thin-Walled Structures, 48:966-978(2010).

[112]A.Rusinek, J.R.Klepaczko. Shear testing of a sheet steel at wide range of strain rates and a constitutive relation with strain-rate and temperature dependence of the flow stress. International Journal of Plasticity, 17(1):87-115(2001).

[113]R.Merle, H.Zhao. Experimental study of sheet metals under dynamic double shear at large strains. Key Engineering Materials, 274:787-792(2004).

[114]H.Zhao. Experimental characterisation of materials behaviour under dynamic loading. Computer & Structures, 81:1301-1310(2003).

[115]F.F.Shi, H.Bing, Y.L.Li, J.Lu, H.Zhao. Experimental study on a graded stainless steel sheet under quasi-static and dynamic loading. Key Engineering Materials, 535:56-59(2013).

[116]Gilormini P, Roudier P, Rougée P, Les déformations cumulées tensorielles, Comptes Rendus de L'Académie des Sciences Série, 316(11):1499-1504(1993).

[117]H.H. Ruan, A.Chen, J.Lu, Characterization of plastically graded nanostructured material: PartI. The theories and the inverse algorithm of nanoindentation. Mechanics of Materials, 42(5):559-569(2010).

[118]H.H. Ruan, A. Chen, J. Lu, Characterization of plastically graded nanostructured material:Part II. The experimental validation in surface nanostructured material. Mechanics of Materials, 42(7):698-708(2010).

[119]W.Goldsmith, S.Finnegan. Penetration and perforation processes in metal targets at and above ballistic limits. International Journal of Mechanical Sciences, 13:843-866(1971).

[120]C.Calder, W.Goldsmith. Plastic deformation and perforation of thin plates resulting from projectile impact. International Journal of Solids and Structures, 7:863-881(1971).

[121]M.Backman, W.Goldsmith. The mechanics of penetration of projectiles into targets. International Journal of Engineering Sciences, 16:1-99(1978).

[122]R.Corran, P.Shadbolt, C. Ruiz. Impact loading of plates： an experimental investigation. International Journal of Impact Engineering, 1:3-22(1983).

[123]S.Leppin, R.Woodward. Perforation mechanisms in thin titanium alloy targets. International Journal of Impact Engineering, 4:107-115(1986).

[124]G.Corbett, S.Reid, W.Johnson. Impact loading of plates and shells by free flying projectiles: a review. International Journal of Impact Engineering, 18:141-230 1986(1996).

[125]T.Wierzbicki. Petalling of plates under explosive and impact loading. International Journal of Impact Engineering, 22:935-954(1999).

[126]Y.W.Lee, T.Wierzbicki. Fracture prediction of thin plates under localized impulsive loading. Part II: Discing and petalling. International Journal of Impact

Engineering, 31:1277-1308(2005).

[127]X.Teng, T.Wierzbicki. Evaluation of six fracture models in high velocity perforation. Engineering Fracture Mechanics, 73:1653-1678(2006).

[128]T.Borvik, M. Langseth, O.S. Hopperstad, K.A. Malo. Ballistic penetration of steel plates. International Journal of Impact Engineering, 22:855-886(1999).

[129]T.Borvik, M.Langseth, O.S Hopperstad, K.A.Malo. Perforation of 12 mm thick steel plates by 20 mm diameter projectiles with flat, hemispherical and conical noses. Part I: Experimental study. International Journal of Impact Engineering, 7:19-35(2002a).

[130]T.Borvik, M.Langseth, O.S.Hopperstad, K.A.Malo. Perforation of 12 mm thick steel plates by 20 mm diameter projectiles with flat, hemispherical and conical noses. Part II: Numerical study. International Journal of Impact Engineering, 27:37-64(2002b).

[131]S.Dey, T.Brovik, O.S.Hopperstad, J.R.Leinum, M.Langseth. The effect of target strength on the perforation of steel plates using three different projectile nose shapes. International Journal of Impact Engineering, 8-9:1005-1038(2004).

[132]A.G.Atkins, M.A.Khan, J.H.Liu. Necking and radial cracking around perforations in thin sheets and normal incidence. International Journal of Impact Engineering, 7:521-539(1998).

[133]J.Dean, C.Dunleavy, P.Brown, T.Clyne. Energy absorption during projectile perforation of thin steel plates and the kinetic energy of ejected fragments. International Journal of Impact Engineering, 36:1250-1258(2009).

[134]N.K.Gupta, M.A.Iqbal, G.S.Sekhon. Experimental and numerical studies on the behaviour of thin aluminium plates subjected to impact by blunt- and hemispherical-nosed projectiles. International Journal of Impact Engineering, 32:1921-1944(2006).

[135]N.K.Gupta, M.A.Iqbal, G.S.Sekhon. Effect of projectile nose shape, impact velocity and target thickness on deformation behaviour of aluminium plates. International Journal of Solids and Structures, 44: 3411-3439(2007).

[136]J.A.Rodr ́guez-Mart ́nez, R.Pesci, A.Rusinek, A.Arias, R.Zaera, D.A.Pedroche. Thermo-mechanical behaviour of TRIP 1000 steel sheets subjected to low velocity perforation by conical projectiles at different temperatures. International Journal of Solids and Structures, 47:1268-1284(2010a).

[137]J.A.Rodr ́guez-Mart ́nez, A.Rusinek, A.Arias. Thermo-viscoplastic behaviour of

2024-t3 aluminium sheets subjected to low velocity perforation at different temperatures. Thin-Walled Structures, 49: 819-832(2011b).

[138]J.A.Rodr ǵuez-Mart ńez, A.Rusinek, P.Chevrier, R.Bernier, A.Arias. Temperature measurements on ES steel sheets subjected to perforation by hemispherical projectiles. International Journal of Impact Engineering, 37:828-841(2010b).

[139]J.A.Rodr ǵuez-Mart ńez, A.Rusinek, R.Pesci. Experimental survey on the behaviour of AISI 304 steel sheets subjected to perforation. Thin-Walled Structures, 48:966-978(2010c).

[140]N.Jones, J.Paik. Impact perforation of aluminium alloy plates. International Journal of impact Engineering, 48:46-53(2012).

[141]H.Zhao, I.Elnasri, Y.Girard. Perforation of aluminium foam core sandwich panels under impact loading-An experiment study. International Journal of Impact Engineering, 34:1246-1257(2007).

[142]I.Elnasri, S.Pattofatto, H.Zhao, H.Tsitsiris, F.Hild, Y.Girard. Shock enhancement of cellular structures under impact loading: Part I Experiments. Journal of the Mechanics and Physics of Solids, 55:2652-2671(2007).

Appendix

Publications and International Communications

[1] **FF. Shi,** R. Merle, B. Hou, YL. Li, H. Zhao. A critical analysis of plane shear tests under quasi-static and impact loading, International Journal of Impact Engineering, 74:107-119, 2014.

[2] **FF. Shi,** B. Hou, YL. Li, H. Zhao. Behavior identification of a multilayered graded stainless steel using an inverse method, Key Engineering Materials, 626:85-90, 2014.

[3] **FF. Shi,** B. Hou, YL. Li, J. Lu, H. Zhao. Experimental study on a graded stainless sheet under quasi-static and dynamic loading, Key Engineering Materials(KEM), 535:56-59, 2013.

[4] **FF. Shi,** B. Hou, YL. Li, H. Zhao. On the impact shear tests using Hopkinson Bar[C], 16th International Conference on Experimental Mechanics, Cambridge, UK, 2014.

[5] **FF. Shi,** T. Suo, B. Hou, YL. Li. Study on strain rate and temperature sensitivity and constitutive model of YB-2 of aeronautical acrylic polymer. Explosion and Shock Waves, 2014(accepted). In Chinese.

[6] WG. Guo, **FF. Shi,** FL. Liu. Investigation on dynamic mechanical performances of DH-36 high strength ship-hull steel, Acta Armament a RII, 30: 203-207, 2009. In Chinese.

[7] WG. Guo, **FF. Shi.** Deformation and failure behavior of MDYB-3 oriented PMMA glass under different loading conditions, Acta Aeronautica et Astronautica Sinica, 29:1517-1525, 2008. In Chinese.

[8] YJ. Mao, YL. Li, **FF. Shi.** A Matlab/Simulink-based method for modelling and simulation of split Hopkinson bar test. World Journal of Modelling and Simulation , 6(3):205-213, 2010.

[9] YJ. Mao, YL. Li, **FF. Shi.** A discussion on determining Young's moduli by conventional split Hopkinson bar, Chinese Journal of Solid Mechanics, 30:170-176, 2009. In Chinese.

[10] X. Chen, YL. Li, **FF. Shi,** HY. Zhao, X. Ma. Influences of adherent thickness,

temperature and velocity on strength of adhesively-bonded single-lap joints. Explosion and Shock Waves, 29(5):449-456, 2009. In Chinese.

[11] H. Huang, D. Saletti, S. Pattofatto, **FF. Shi,** H. Zhao. Experimental observation of phase transformation front of SMA under impact loading. 13th International Conference on Fracture, Beijing, China, 2013.